

AFTAC Project No. VELA T/7704
ARPA Order No. 624
ARPA Program Code No. 7F10

AD694099

FINAL ANALYSIS REPORT
ALEUTIAN ISLANDS EXPERIMENT
OCEAN-BOTTOM SEISMOGRAPHIC EXPERIMENTS

Prepared by

A. Frank Linville Gary D. McNeely Ronald D. Bauer
R. Fred Howard A. Ronald Mendina

Terence W. Harley, Program Manager
Telephone: 1-214-238-3473

TEXAS INSTRUMENTS INCORPORATED
Science Services Division
P. O. Box 5621
Dallas, Texas 75222

Effective Date of Contract: 5 April 1967
Contract Expiration Date: 31 October 1968
Amount of Contract: \$1,054,991

ACKNOWLEDGMENT

This research was supported by the
ADVANCED RESEARCH PROJECTS AGENCY
Nuclear Test Detection Office
under Project VELA UNIFORM
and accomplished under the technical direction of the
AIR FORCE TECHNICAL APPLICATIONS CENTER
Contract No. F33657-67-C-1341

D D C

OCT 7 1969

B

31 July 1968

Reproduced by the
CLEARINGHOUSE
for Federal Scientific & Technical
Information Springfield Va. 22151

This document has been approved
for public release and sale; its
classification is unlimited

**BEST
AVAILABLE COPY**



Distribution of this document is unlimited

AFTAC Project No. VELA T/7704
ARPA Order No. 624
ARPA Program Code No. 7F10

FINAL ANALYSIS REPORT
ALEUTIAN ISLANDS EXPERIMENT
OCEAN-BOTTOM SEISMOGRAPHIC EXPERIMENTS

Prepared by

A. Frank Linville Gary D. McNeely Ronald D. Bauer
R. Fred Howard A. Ronald Mendina

Terence W. Harley, Program Manager
Telephone: 1-214-238-3473

TEXAS INSTRUMENTS INCORPORATED
Science Services Division
P.O. Box 5621
Dallas, Texas 75222

Effective Date of Contract: 5 April 1967
Contract Expiration Date: 31 October 1968
Amount of Contract: \$1,054,991

ACKNOWLEDGMENT

This research was supported by the
ADVANCED RESEARCH PROJECTS AGENCY
Nuclear Test Detection Office
under Project VELA UNIFORM
and accomplished under the technical direction of the
AIR FORCE TECHNICAL APPLICATIONS CENTER
Contract No. F33657-67-C-1341

31 July 1968



ABSTRACT

The crustal structure across Amchitka was determined from two in-line reversed-refraction profiles located northeast and southwest of Amchitka. Both profiles employed 10 Ocean-Bottom Seismographs (OBS) spaced at 20-km intervals and 5-ton shots detonated at 20-km intervals off each end of the OBS line. traveltimes were corrected to a reference plane 4.5 km below sea level to minimize lateral velocity variations associated with the large changes in water depth in the area. Depth to the Moho along the profile was determined from first arrivals using standard refraction analysis, wave-front methods, the time-term method and model perturbation techniques. Calculations show the Moho refractor to be dipping towards Amchitka with the root of the structure located 60 km north of Amchitka under Semisopochnoi Island. The Moho velocity is 8.1 km/sec in the area.

Nearly all of the first arrivals were Moho refractions; therefore, digital techniques were employed to enhance the capability of picking secondary arrivals in order to obtain upper crustal velocity information. In general, secondary arrivals were difficult to identify, and although some apparent velocity measurements were obtained, the information could not be directly incorporated into the crustal model.



TABLE OF CONTENTS

Section	Title	Page
I	SUMMARY	I-1
II	CRUSTAL STUDY	II-1
	A. DATA REDUCTION	II-1
	1. Correction to Reference Plane	II-1
	2. First Arrivals and Secondaries	II-2
	3. Deconvolution	II-39
	B. REFRACTION ANALYSIS	II-46
	1. Iterations	II-46
	2. Refraction Model	II-46
	C. WAVEFRONT ANALYSIS	II-55
	1. Wavefront Methods	II-55
	2. Wavefront Model	II-57
	D. TIME-TERM ANALYSIS	II-63
	1. Time-Term Theory	II-63
	2. Time-Term Model	II-70
	3. Theoretical Example	II-73
	E. TRAVELTIME ANALYSIS	II-76
	1. Traveltime Program	II-76
	2. Perturbation Model	II-80
III	EFFECT OF CRUSTAL STRUCTURE ON REGIONAL TRAVELTIMES	III-1
IV	REFERENCES	IV-1

APPENDIX CONFIDENCE LEVELS



LIST OF ILLUSTRATIONS

Figure	Description	Page
I-1	Phase I Station and Explosion Locations	I-5
I-2	Phase III Station and Explosion Locations	I-6
I-3	Phase II Station and Explosion Locations	I-7
I-4	Water Bottom Profile for Phases I and III with Shor's Published Sections	I-9
I-5	Comparison of Models Determined by Refraction, Wavefront, Time-Term, and Perturbation Methods	I-11
II-1	Method of Reference-Plane Correction	II-10
II-2	Example of Digitized Field Data from OBS	II-11
II-3	Gathered Traces of All Shots Recorded at One Station, Aligned at 8 km/sec with Trace Amplitudes Equalized	II-12
II-4	Gathered Traces of One Shot Recorded at All Stations, Aligned at 8 km/sec with Trace Amplitudes Equalized	II-13
II-5	Gathered Traces of All Shots Recorded at One Station, Aligned Vertically with Trace Amplitudes Equalized	II-14
II-6	Gathered Traces of One Shot Recorded at All Stations, Aligned Vertically with Trace Amplitudes Equalized	II-15
II-7	Gathered Traces of All Shots Recorded at S10 and S9	II-16
II-8	Gathered Traces of All Shots Recorded at S8 and S7	II-17
II-9	Gathered Traces of All Shots Recorded at S6 and S5	II-18
II-10	Gathered Traces of All Shots Recorded at S2 and S1	II-19
II-11	Gathered Traces of All Shots Recorded at S10 and S9, Horizontal Instruments	II-20
II-12	Gathered Traces of All Shots Recorded at S2 and S1, Horizontal Instruments	II-21
II-13	Gathered Traces of E3 and E4 Recorded at All Stations	II-22
II-14	Gathered Traces of E5 and E6 Recorded at All Stations	II-23
II-15	Gathered Traces of E30 and E31 Recorded at All Stations	II-24



LIST OF ILLUSTRATIONS (CONTD)

Figure	Description	Page
II-16	Gathered Traces of All Shots Recorded at S31 and S23	II-25
II-17	Gathered Traces of All Shots Recorded at S31 and S23, Horizontal Instruments	II-26
II-18	Raw traveltimes of Phase I Secondary Arrivals for All Shots Recorded at Each Station	II-27
II-19	Raw traveltimes of Phase I Secondary Arrivals for Each Shot Recorded at All Stations	II-28
II-20	Raw traveltimes of Phase I Secondary Arrivals, Horizontal Instruments	II-29
II-21	Raw traveltimes of Phase III Secondary Arrivals	II-30
II-22	Corrected traveltimes of Phase I Secondary Arrivals for All Shots Recorded at Each Station	II-31
II-23	Corrected traveltimes of Phase I Secondary Arrivals for Each Shot Recorded at All Stations	II-32
II-24	Corrected traveltimes of Phase I Secondary Arrivals, Horizontal Instruments	II-33
II-25	Corrected traveltimes of Phase III Secondary Arrivals	II-34
II-26	Reduced traveltimes of Phase I Secondary Arrivals for All Shots Recorded at Each Station	II-35
II-27	Reduced traveltimes of Phase I Secondary Arrivals for Each Shot Recorded at All Stations	II-36
II-28	Reduced traveltimes of Phase I Secondary Arrivals, Horizontal Instruments	II-37
II-29	Reduced traveltimes of Phase III Secondary Arrivals	II-38
II-30	Deconvolution, Station S31	II-41
II-31	Deconvolution, Station S23	II-42



LIST OF ILLUSTRATIONS (CONTD)

Figure	Description	Page
II-32	Deconvolution, Station S1	II-43
II-33	Deconvolution, Station S7	II-44
II-34	Deconvolution, Station S10	II-45
II-35	Equations for Solving Reverse Profile	II-47
II-36	Fitted Reverse Profile Between E34 and E7, Phase I	II-48
II-37	Fitted Single Profile of Phase I Shots Recorded at S10	II-49
II-38	Fitted Reverse Profile Between E24 and E15, Phase III	II-50
II-39	Fitted Single Profile of Phase III Shots Recorded at S31	II-51
II-40	Refraction Model Based on First Arrivals	II-53
II-41	Reverse Profile Plot Between E34 and E7, Phase I	II-60
II-42	Wavefront Model Using General Wavefront Method	II-61
II-43	Wavefront Targeting Method	II-62
II-44	Ray Path Diagram for Critically Refracted Rays	II-64
II-45	Time-Term Model Using Data from Phase I, Phase III, and Land Stations at Adak, Atka, Shemya, and Amchitka	II-72
II-46	Time-Term Model Using Data from Phase I, Phase III, and Adak Land Station	II-74
II-47	Time-Term Results Using Theoretically Computed Traveltimes	II-75
II-48	Time-Term Results Using Theoretically Computed Traveltimes (model with dip angles less than 5.2°)	II-78



LIST OF ILLUSTRATIONS (CONTD)

Figure	Description	Page
II-49	Example of Output from Program which Computes Traveltimes for Crustal Models with Layers that Change Dip	II- 79
II-50	Model-Perturbation Results Showing Initial Model and Iterations 1 Through 4	II-83
II-51	Model-Perturbation Results Showing Iterations 5 Through 8	II-85
III-1	Crustal Refraction Ray Paths for Symmetrical Model, Standard Crust, and Dual Model, Amchitka Crust with Standard Crust	III - 3
III-2	Reduced Traveltimes for Symmetrical Model and Dual Model	III-4

LIST OF TABLES

Table	Title	Page
II-1	Least-Squares Line Fits	II-7
II-2	Average Velocities of Secondary Arrivals	II-9
II-3	Shot/Station Experimental Data	II-71
II-4	Shot/Station Theoretical Data	II-77
II-5	Traveltime Residual Values	II-82

BLANK PAGE



SECTION I

SUMMARY

The Ocean-Bottom Seismograph (OBS) Aleutian Islands Experiment was conducted between 5 April 1967 and 31 October 1968. The objective of the experiment was to determine the crustal structure across Amchitka Island and subsequently to determine the effect of that structure on seismic traveltimes anomalies observed from the LONGSHOT explosion, which was detonated on Amchitka on 29 October 1965.

Unit and equipment preparation, field operations, and data analysis were the tasks performed under the experiment. These tasks have been discussed in previous reports:

- Operations Report¹ — a detailed description of unit and equipment preparation and field operations
- System Response Report² — a description of the determination of vertical and horizontal amplitude responses of the Ocean-Bottom Seismograph system
- Preliminary Analysis Report³ — details of data quality, basic reduction of the first-arrival data, determination of charge depths using hydroacoustic traveltimes recordings and bubble-pulse-period measurements, compilation of preliminary bulletin, and a model of the crustal structure across Amchitka obtained using standard refraction methods

Final results of the data analysis program are presented in this report.

Data obtained from the Aleutian Islands Experiment were collected in three phases. Instrument arrays (OBS) and shot arrays (5-ton explosions) were deployed along a line N42°E across Amchitka for each phase.



OBS instrument and shot locations for Phases I and III are shown in Figures I-1 and I-2, respectively. These two arrays were designed to record refraction arrivals from the Moho in order to determine the crustal structure along the profile.

Phase II instruments (Figure I-3) were deployed at longer ranges with larger spacings than Phases I and III to record seismic waves penetrating the upper mantle from the CHASE-VI explosion. However, CHASE VI did not detonate, precluding direct upper mantle observations by the OBS.

The explosion recordings were edited onto digital tape and played back, and first arrivals were picked. Due to significant changes in water depth and structural environment across the profile (Figure I-4), the traveltimes data were corrected to a reference plane (4.5 km below sea level) for interpretive purposes. The crustal parameters used in correcting the data to a reference plane were estimated by a series of iterations.³ Errors resulting from incorrect velocity assumptions were minimized by choosing the reference plane to approximate the water bottom on either side of the Aleutian Ridge.

Nearly all of the first arrivals obtained were Moho-refracted events; therefore, any upper crustal velocity information must necessarily be derived from secondary arrivals. Digital techniques were employed to enhance the capability of picking secondary arrivals. Traces were gathered to produce records consisting of all explosions recorded at one station and all stations recording one explosion. Static corrections were applied to align the traces at a velocity of 8 km/sec; trace amplitudes were equalized to reduce signal variations across the records; and deconvolution filters were designed and applied to remove reverberation effects. Some secondary arrivals were picked, time-distance plots generated, and apparent velocities determined



from least-square line fits. In general, however, secondary arrivals were difficult to identify, even after processing. In addition, a positive identification of the same secondary arrival from opposite directions across the profile could not be made. Thus the velocity information derived, while indicating the existence of intermediate refractors, is qualitative and cannot be directly incorporated into the crustal model.

Section II describes the four methods of crustal structure determination used. Only first-arrival information was used for each method, and the average crustal velocity was taken as 6.4 km/sec. The methods are standard refraction, wavefront, time-term, and model perturbation. Figure I-5 shows a comparison of the resulting model obtained using each method. The structure obtained from each method is similar; however, differences arise from the basic assumptions necessary to implement each method.

The standard refraction method assumes plane-dipping constant-velocity layers across the profile. Phase I and Phase III OBS instrument arrays and shot arrays were designed to divide the structure across the Aleutian Ridge into four segments, each of which could be approximated by a plane-dipping layer. A reverse-time mistie showed that the structure under Phase III instruments could not be adequately represented by a plane-dipping layer.³

The wavefront method (applied to the structure under Phase I instruments only) indicated the adequacy of the method there and showed the need for denser recording along the profile.

The time-term method produced distortion in the model associated with the root of the structure. Theoretical calculations verified the distortion which was attributed to a deviation from the time-term assumption of interface planarity within the cone of critical refraction.



The traveltimes model was determined by perturbation techniques.

Iterations were performed by

- (1) Selecting a beginning model
- (2) Calculating theoretical traveltimes for the model
- (3) Modifying the model based on differences between calculated traveltimes and observed traveltimes
- (4) Repetitively applying steps 2 and 3 until a best fit is determined

The model-perturbation method produces a model (not necessarily unique) which fits the data by considering the actual ray paths involved and is not restricted by the various assumptions which are necessary to implement the other methods. In addition, the method utilizes every available shot/station observation along the profile. For these reasons, the perturbation model presented in Figure I-5 (bottom) is considered the most accurate representation of the crustal structure across Amchitka which can be obtained from the data collected in this experiment.

Section III compares traveltimes observed at distance ranges of 16° to 24° for a Jeffreys-Bullen (JB) crustal model and the Aleutian crustal model. Due primarily to the differences in average crustal velocity, variations up to 1.5 sec are observed. The effect of a dipping structure can be seen, but effect is less than 1 sec for the model used. This analysis is not exhaustive but does suggest that a significant portion of the traveltime anomalies observed from LONGSHOT is caused in the upper mantle.

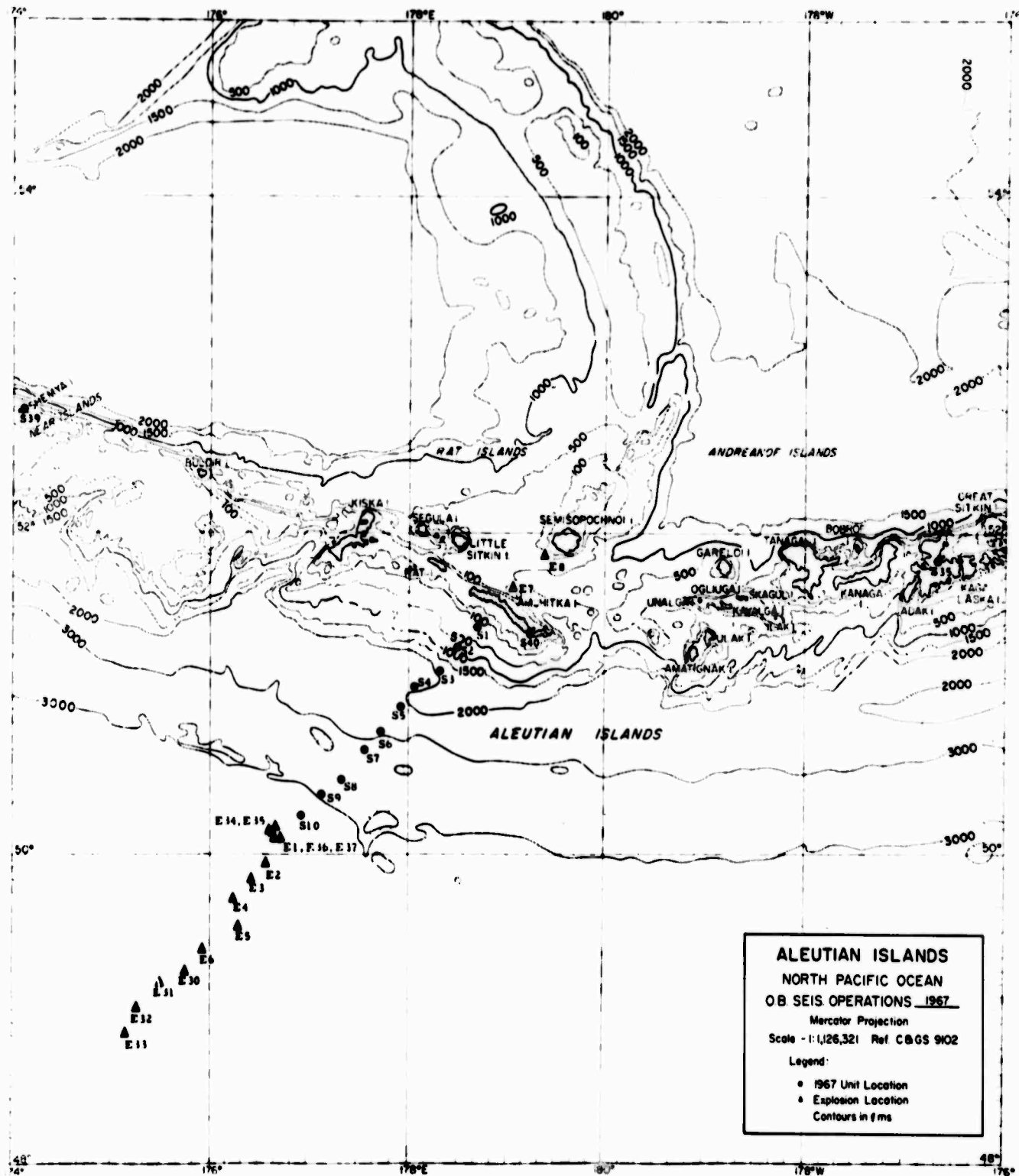


Figure I-1. Phase I Station and Explosion Locations

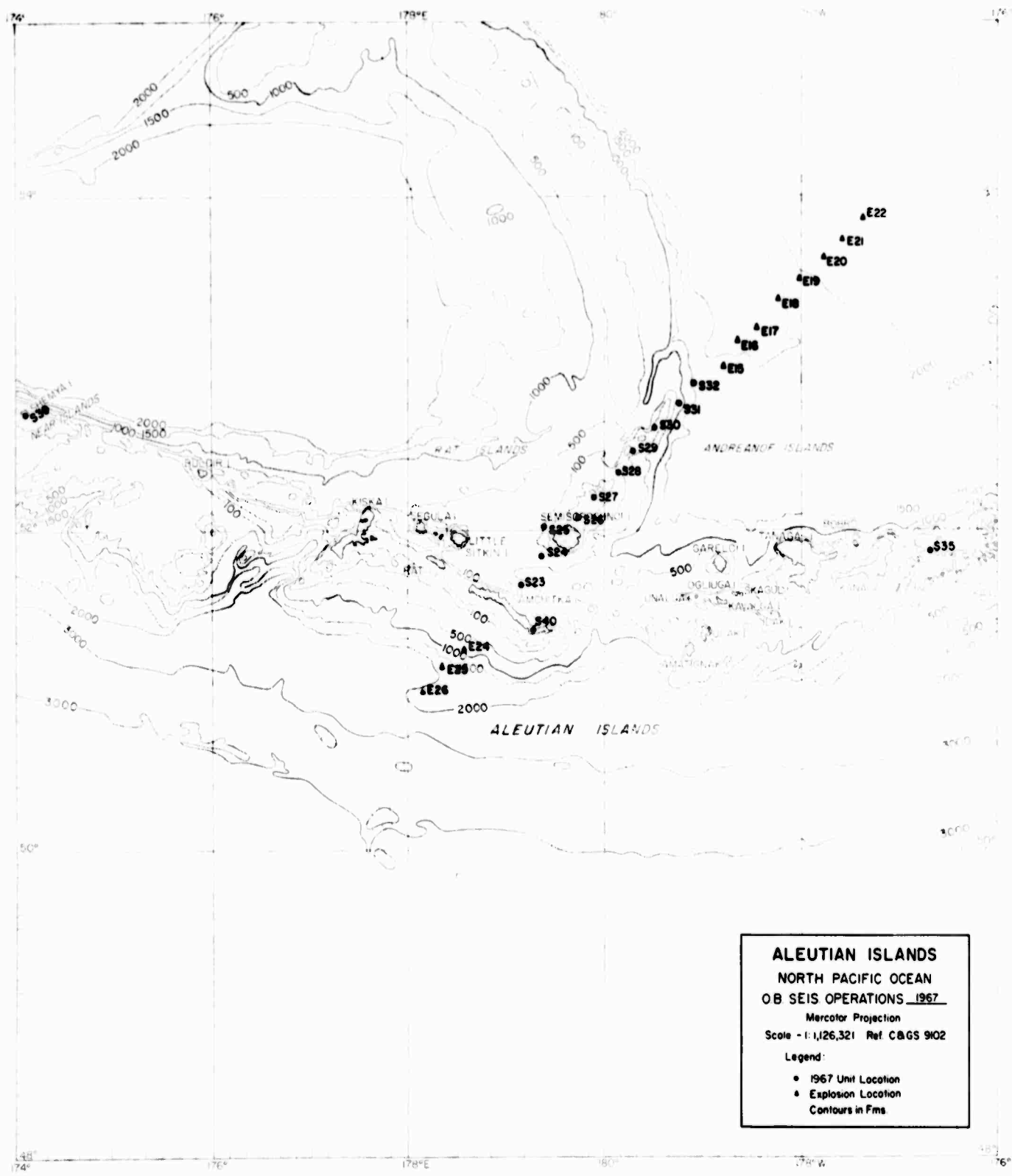


Figure I-2. Phase III Station and Explosion Locations

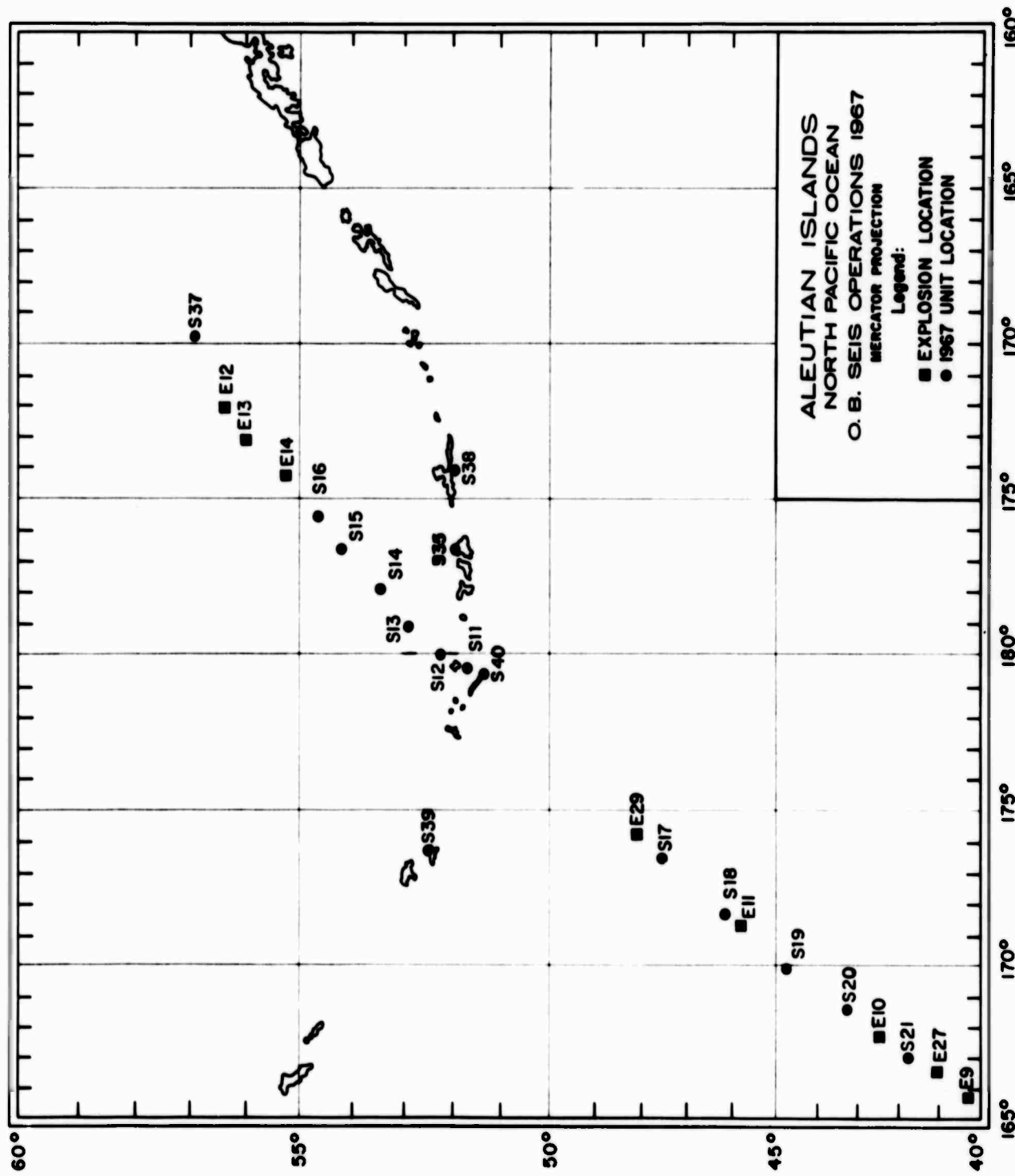
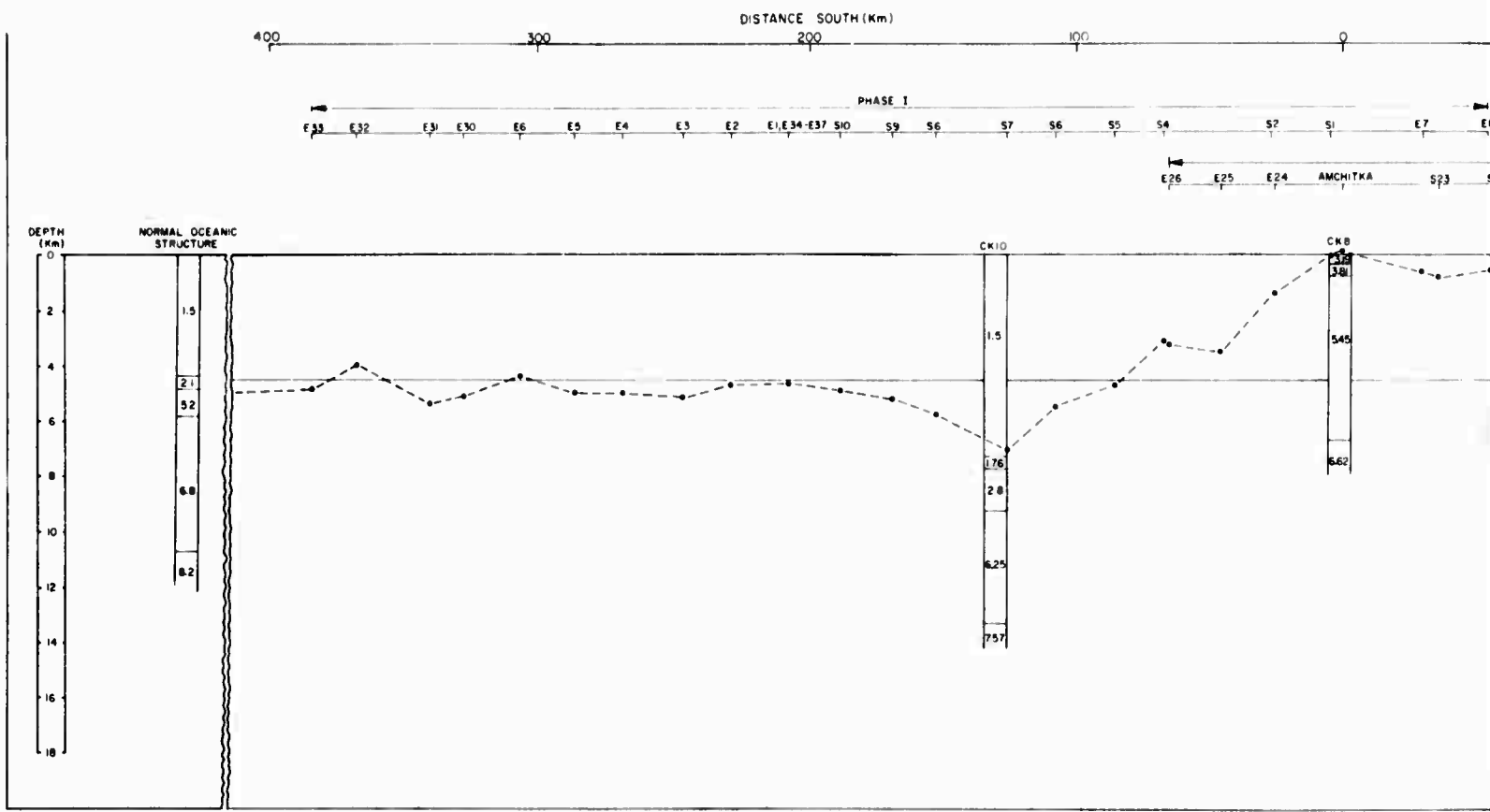


Figure I-3. Phase II Station and Explosion Locations



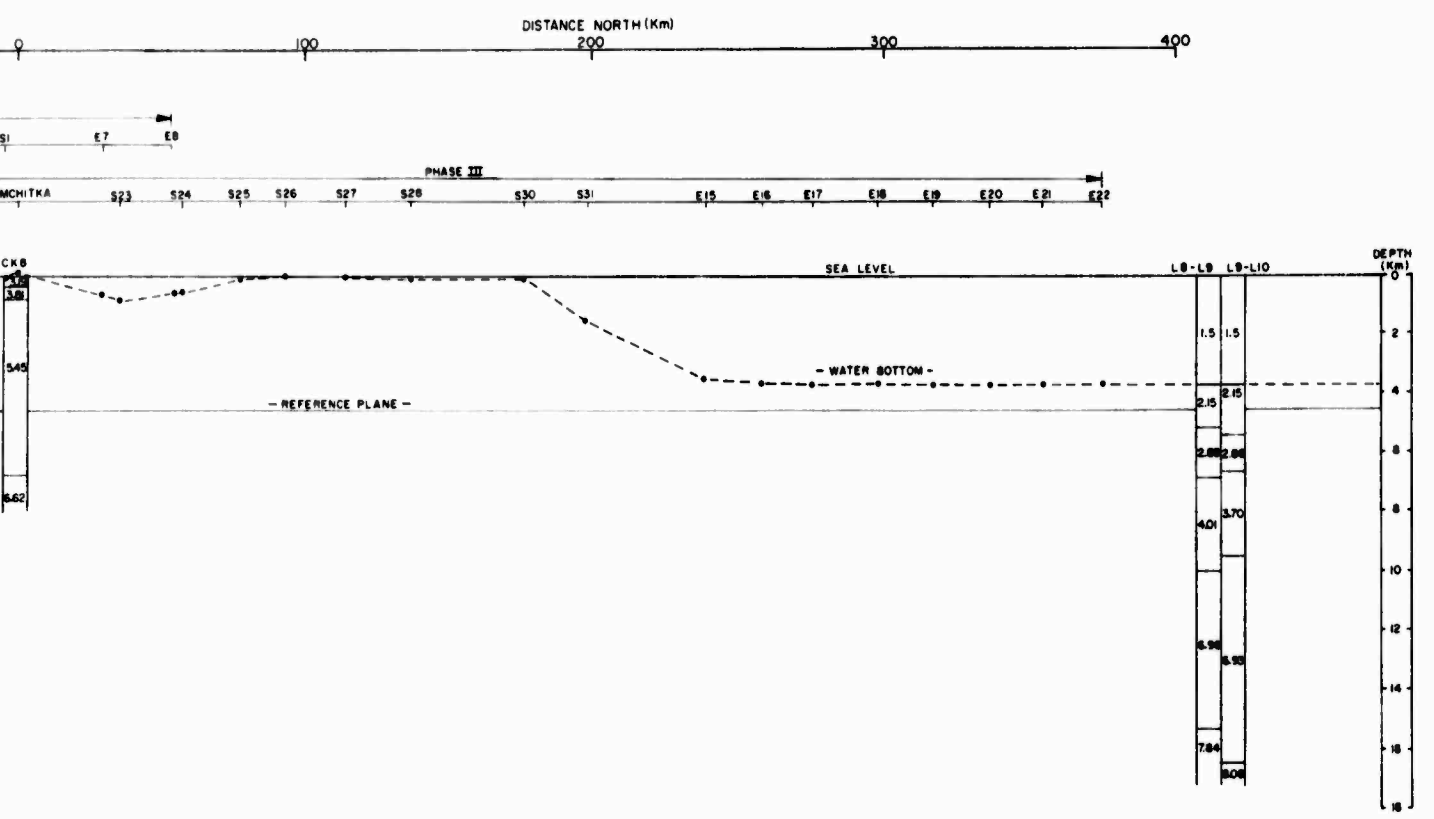


Figure I-4. Water Bottom Profile for Phases I and III with Shor's Published Sections (X10 vertical exaggeration)

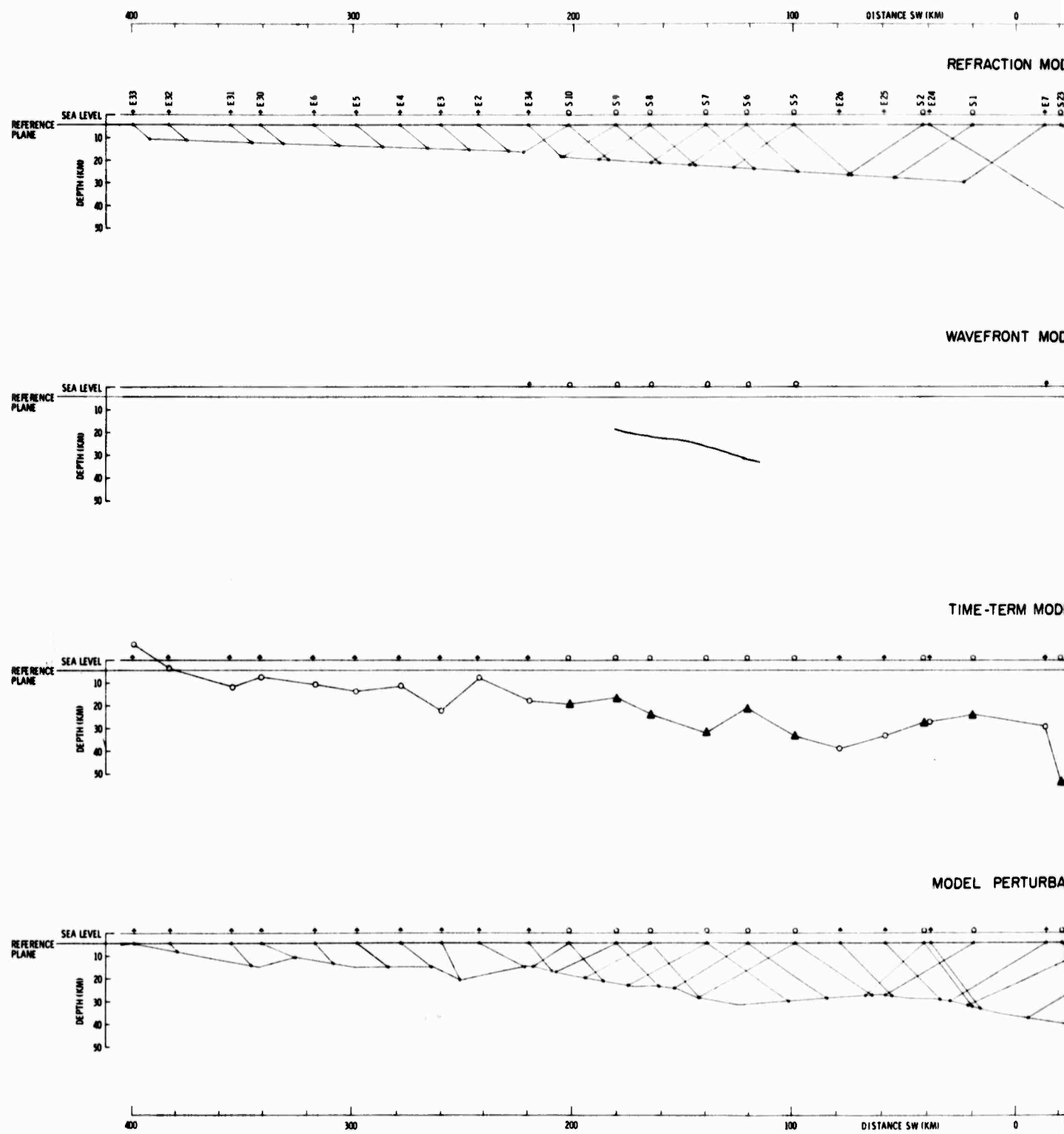


Figure I-5.

A

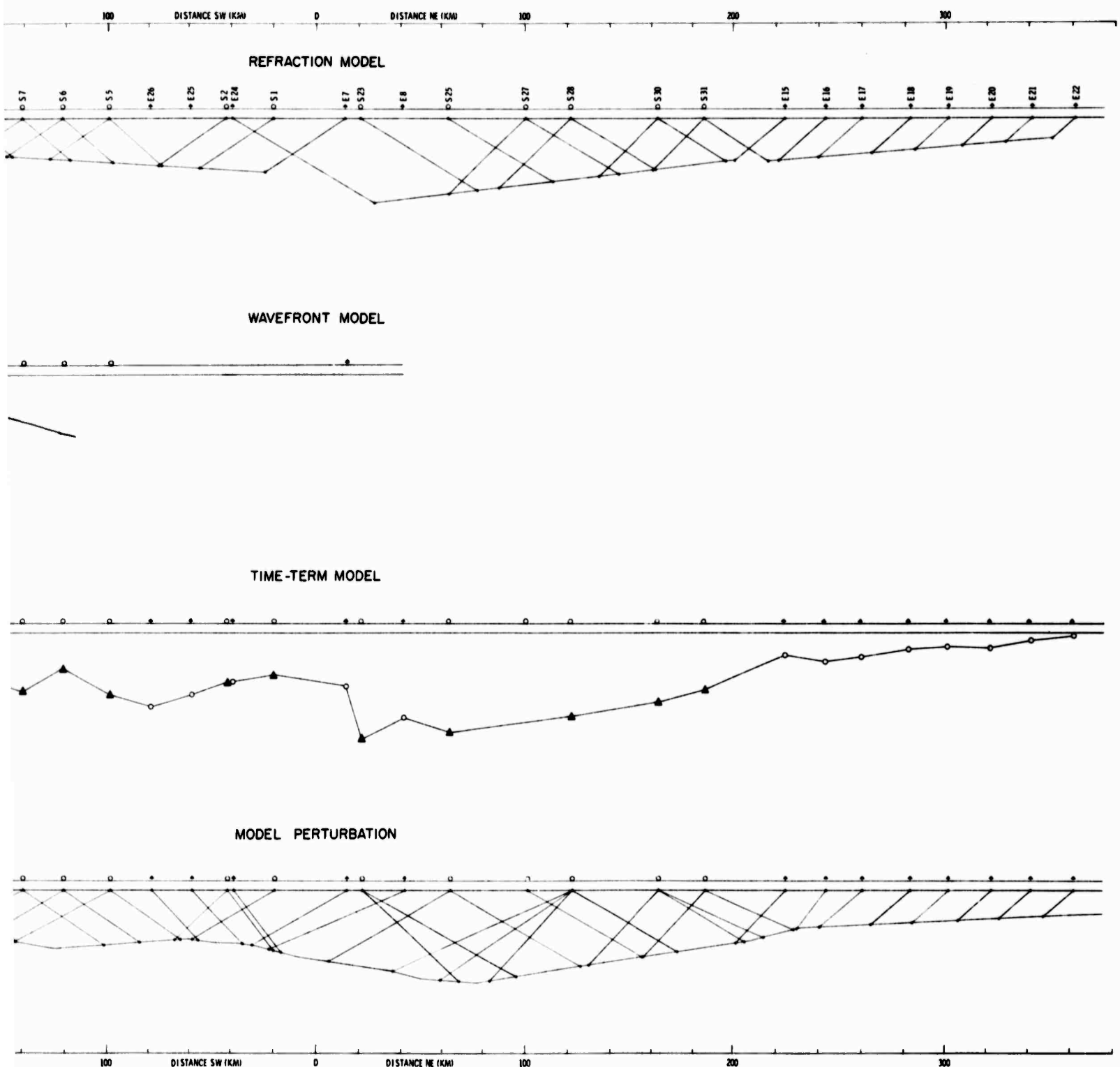


Figure I-5. Comparison of Models Determined by Refraction, Wavefront, Time-Term, and Perturbation Methods

BLANK PAGE



SECTION II

CRUSTAL STUDY

The objective of the study presented in this section was to determine the crustal structure across the Aleutian Ridge so that its effect on seismic traveltimes anomalies observed at teleseismic distances from the LONGSHOT explosion on Amchitka could be defined. Data used were collected in Phase I and Phase III operations. Phase I (Figure I-1) consisted of a line of 10 OBS instruments south of Amchitka spaced 20 km apart, with 10 explosions detonated in-line to the south and two explosions in-line to the north of Amchitka. The Phase III array (Figure I-2) consisted of 10 OBS instruments located north of Amchitka along the Petrel Bank, with eight explosions in-line to the north and three in-line to the south of Amchitka.

Results of four crustal analysis methods using data from Phase I and Phase III are presented in this section. The analysis methods are refraction, wavefront, time-term, and model perturbation. The refraction analysis was presented in the Preliminary Analysis Report³ along with details of data quality and data handling. Those results are briefly reviewed here for comparison with results from the other methods.

Because of the shot and seismometer geometry used in the experiment, nearly all first arrivals were Moho-refracted events. Consequently, a study of secondary arrivals was undertaken in order to obtain upper crustal velocity information. Trace gathering, amplitude equalization, and deconvolution techniques were applied to the digitized data to aid in the interpretation of secondary arrivals.

A. DATA REDUCTION

1. Correction to Reference Plane

Since all explosions and receivers were not located on the same plane, the data were reduced to a reference plane for interpretive purposes.



The method, described in the Preliminary Analysis Report,³ reduced the raw traveltimes to traveltimes below a reference plane by stripping off the time from explosion to reference plane and station to reference plane. Figure II-1 illustrates this method. Computer programs were written to process the arrival-time data.

The following parameters are input to the correction program:

V_1 — water velocity
 V_{2A} — subwater velocity (low)
 V_{2B} — subwater velocity (high)
 V_n — refractor velocity
 RP — reference-plane depth
 DP — decision-plane depth
 V_{Red} — velocity used to compute reduced traveltime
 t_R ; i.e.,

$$t_R = t - \frac{\Delta}{V_{Red}}$$

where

t = traveltime corrected to RP

Δ = distance

The output of this program is then used to generate CalComp plots of the raw, corrected, and reduced traveltimes vs distance. In addition, a third program computes least-squares line fits to both the raw times and corrected times.

2. First Arrivals and Secondaries

The refraction model developed during the preliminary analysis was based on first arrivals. Those arrivals were grouped into three categories:



Pn, Pg, and shallow Pg arrivals. Based on first arrivals, portions of only two refractors above the Moho could be mapped. Therefore, additional upper crustal velocity information must come from secondary arrivals.

Attempts to pick secondary arrivals from the field records did not produce meaningful results; consequently, additional processing was performed to enhance the capability of picking secondary arrivals. Digitized explosion recordings (Figure II-2) from Phases I and III and the northern part of Phase II were used as input data for TIAC processing, which comprised

- Trace gathering
- Trace amplitude equalization
- Static correction
- Paper playbacks (filtered and unfiltered)

The initial trace-gathering sequence consisted of gathering the pressure and vertical traces for all explosions recorded by one station to form one output record. The two horizontal traces were gathered in the same manner to form a second record. Trace amplitudes were equalized and static corrections applied to align the traces at a velocity of 8 km/sec (Figure II-3). Equalization was performed by scaling the traces so that their mean absolute values over the equalization gate (9.6 sec) were equal. This procedure gives record-to-record equalization, as well as trace-to-trace equalization. Using the records of the first gathering sequence, the traces were gathered to form records consisting of all stations recording a single explosion (Figure II-4).

A second set of records was made by applying static corrections to individual traces in order to vertically align the first motion of all traces (Figures II-5 and II-6). After each gathering sequence, paper playbacks of all records were made and frequency filters applied to further enhance the signal quality. Examples of the secondary arrivals are shown in Figures II-7 through II-17.



Figures II-7 through II-10 are records showing all explosions recorded by a station (pressure and vertical traces). The predominant arrival after the initial P-phase is the arrival corresponding to one air/water interface surface reflection in the water layer at the receiver. Only in the case of all explosions recorded by S10 (Figure II-7, top) could an arrival be followed across all traces. Most of the later arrivals appear to be emergent.

Figures II-11 and II-12 show examples of the horizontal traces for all explosions recorded at a single station. Stations S10 and S9 show the best arrivals, but only two or three picks could be made. Records of S2 and S1 show the cyclic nature of many of the arrivals. Also, it can be seen that the moveout pattern is not consistent.

Shown in Figures II-13 through II-15 are examples of all stations recording a single explosion (pressure and vertical traces). As in the other examples, the secondary arrivals are emergent, with the number of picks scattered from record to record. Figures II-13 (bottom) and II-14 (top) show the air/water interface surface reflection at the station.

Phase III recordings are illustrated in Figures II-16 and II-17. Figure II-16 shows the pressure and vertical traces for S31 and S23, and Figure II-17 shows the horizontal traces for the same stations. All secondary arrivals for Phase III were picked from recordings showing all explosions recorded at one station. Records showing all stations recording one explosion were of little value because of high noise levels or instrument problems at many stations. Secondary arrivals from Phase II were insufficient to produce meaningful data.

After all secondary arrivals had been picked, the times were converted to GCT, punched on cards, and processed through the correction program using the following parameters:



$$\begin{aligned}V_1 &= 1.5 \text{ km/sec} \\V_2 &= 2.1 \text{ km/sec} \\V_{2B} &= 5.0 \text{ km/sec} \\V_n &= 7.0 \text{ km/sec} \\RP &= -4.5 \text{ km} \\DP &= 3.5241 \text{ km} \\V_{Red} &= 8.0 \text{ km/sec}\end{aligned}$$

Output data from the reference-plane program were divided into four groups for plotting:

- Pressure and vertical arrivals — all explosions recorded at each station (Phase I)
- Pressure and vertical arrivals — all stations recording each explosion (Phase I)
- Horizontal component arrivals (Phase I)
- All secondary arrivals (Phase III)

Plots of the raw times and corrected times (Figures II-18 through II-25) were made. Comparison of the two sets of plots shows that the largest effect of the reference-plane correction was to lower the points by 2 to 4 sec (which is essentially the traveltime through the water layer from shot to the water bottom).

Reduced traveltime plots of the four sets of data are shown in Figures II-26 through II-29. Lines connecting the points which represent secondary picks across the records are shown. It is apparent that some picks represent multiple reflections in the water layer. Water depth at station S2 is 1.44 km, which gives a 2-way traveltime through the water layer of about 2 sec. The three sets of secondary arrivals picked from the horizontal instruments at S2 (Figure II-28) show a time separation of about 2 sec, indicating that the two latest sets were multiple reflections in the water layer. Similarly,



the two latest sets of secondary arrivals (Figure II-29) picked from station S31 (water depth of 1.58 km) show a time separation corresponding to multiple reflections in the water layer. Water depths for stations S5 through S10 (and the southern shots of Phase I) indicate a 2-way traveltimes of 6 to 9 sec; therefore, the secondary arrivals occurring in the 6- to 9-sec interval following the initial arrival cannot be attributed to multiple reflections in the water layer.

Least-square-error line fits (Table II-1) were made for each set of arrivals having at least four picks. Line fits for Phase I explosions recorded by individual stations (pressure and vertical traces) gave apparent velocities ranging from 6.89 km/sec to 7.96 km/sec. Velocities from pressure and vertical-trace picks of gathered records (stations recording explosions) ranged from 5.70 km/sec to 6.65 km/sec. Individual line fits for secondary arrivals picked from the horizontal traces gave velocities ranging from 5.13 km/sec to 7.53 km/sec. Due to the data quality of Phase III, only eight line fits for explosions recorded at stations could be determined. The velocities ranged from 6.61 km/sec to 7.43 km/sec.

In addition to the individual line fits, the secondary arrivals were grouped to determine average velocities (Table II-2). Phase I arrivals from all explosions recorded at one station gave an average velocity of 7.42 km/sec. Phase I secondary arrivals for all stations recording one explosion gave an average velocity of 6.23 km/sec. The average velocity for Phase I horizontal arrivals was 6.67 km/sec. Phase III arrivals gave an average velocity of 7.04 km/sec. The secondary arrivals indicate the existence of intermediate refractors. A single intermediate refractor with a true velocity of about 6.8 km/sec and dipping toward Amchitka could explain most of the measured apparent velocities under Phase I shots and stations. It was impossible to positively identify the same secondary arrival from two directions across the profile; this is necessary to determine true velocity, dip, and depth of the refractor.



Results of this study show the difficulty of identifying secondary refraction arrivals, picking their onsets, and identifying the same arrival recorded from opposite directions. The techniques employed here — trace gathering, static correction, and trace amplitude equalization — optimize the recorded data for interpretation; however, the results indicate the importance of utilizing shooting and recording techniques which allow recording first arrivals from each interface.⁴

Table II-1
LEAST-SQUARES LINE FITS

Phase I, Shots Recorded at Stations

<u>Station</u>	<u>Explosion</u>	<u>Velocity</u> (km/sec)	<u>Intercept</u> (sec)	<u>Slope</u>
S1	E34, E3, E5, E6, E30, E31, E32	7.32	2.54	0.1365
S2	E5, E6, E30, E31, E32	7.68	3.07	0.1302
S5	E2, E3, E4, E6, E30, E31	7.27	3.63	0.1373
S6	E2, E3, E4, E5, E32	7.57	3.57	0.1321
S6	E6, E30, E31, E32	7.96	3.31	0.1256
S7	E34, E2, E3, E4, E5, E6	7.24	4.40	0.1382
S9	E34, E3, E4, E5	6.89	1.70	0.1452
S9	E3, E4, E5, E6, E30	7.42	2.75	0.1348
S10	E34, E2, E3, E4, E5, E6, E30, E31, E32, E33	7.46	3.41	0.1341
S10	E3, E4, E5, E32, E33	7.41	6.68	0.1349



Table II-1 (contd)

Phase I, Stations Recording Shots

<u>Station</u>	<u>Explosion</u>	<u>Velocity (km/sec)</u>	<u>Intercept (sec)</u>	<u>Slope</u>
S2, S5, S7, S8	E2	6.64	2.39	0.1505
S2, S5, S6, S7, S8	E4	6.44	0.94	0.1552
S2, S5, S6, S7, S9, S10	E4	6.24	8.89	0.1603
S6, S7, S8, S9, S10	E4	6.47	2.58	0.1646
S2, S5, S6, S7, S9, S10	E5	5.69	2.42	0.1758
S1, S2, S5, S6, S7, S8, S10	E5	6.15	11.84	0.1627
S1, S2, S5, S6, S9	E5	5.70	12.87	0.1754
S1, S2, S5, S6, S7, S8	E31	6.65	1.58	0.1504
S7, S8, S9, S10	E31	6.09	-2.51	0.1642

Phase I, Shots Recorded at Stations (Horizontal)

S1	E3, E4, E5, E6	6.38	1.21	0.1568
S2	E2, E3, E4, E5, E6, E30, E31	7.44	4.50	0.1344
S2	E2, E3, E4, E5, E6, E30, E31	7.53	7.48	0.1328
S2	E2, E3, E4, E5, E6	7.21	8.69	0.1388
S9	E5, E6, E31, E32	6.61	3.40	0.1513
S9	E3, E4, E5, E6	6.36	10.86	0.1572
S10	E3, E4, E5, E6	5.13	6.68	0.1948



Table II-1 (contd)

Phase III, Shots Recorded at Stations

<u>Station</u>	<u>Explosion</u>	<u>Velocity (km/sec)</u>	<u>Intercept (sec)</u>	<u>Slope</u>
S31	E16, E17, E18, E19, E22	6.95	12.14	0.1438
S31	E16, E17, E18, E20, E21, E22	7.18	14.58	0.1392
S30	E16, E17, E19, E20	7.43	13.95	0.1345
S28	E15, E16, E17, E18	6.61	21.84	0.1513
S23	E17, E18, E19, E20, E21	6.79	3.61	0.1473
S31	E15, E17, E19, E21	6.96	16.10	0.1436
S28	E15, E16, E17, E19, E20	7.33	7.76	0.1364

Table II-2

AVERAGE VELOCITIES OF SECONDARY ARRIVALS

	<u>Velocity (km/sec)</u>
Phase I, Shots Recorded at Stations	7.42
Phase I, Stations Recording Shots	6.23
Phase I, Shots Recorded at Stations (Horizontal)	6.67
Phase III, Shots Recorded at Stations	7.04

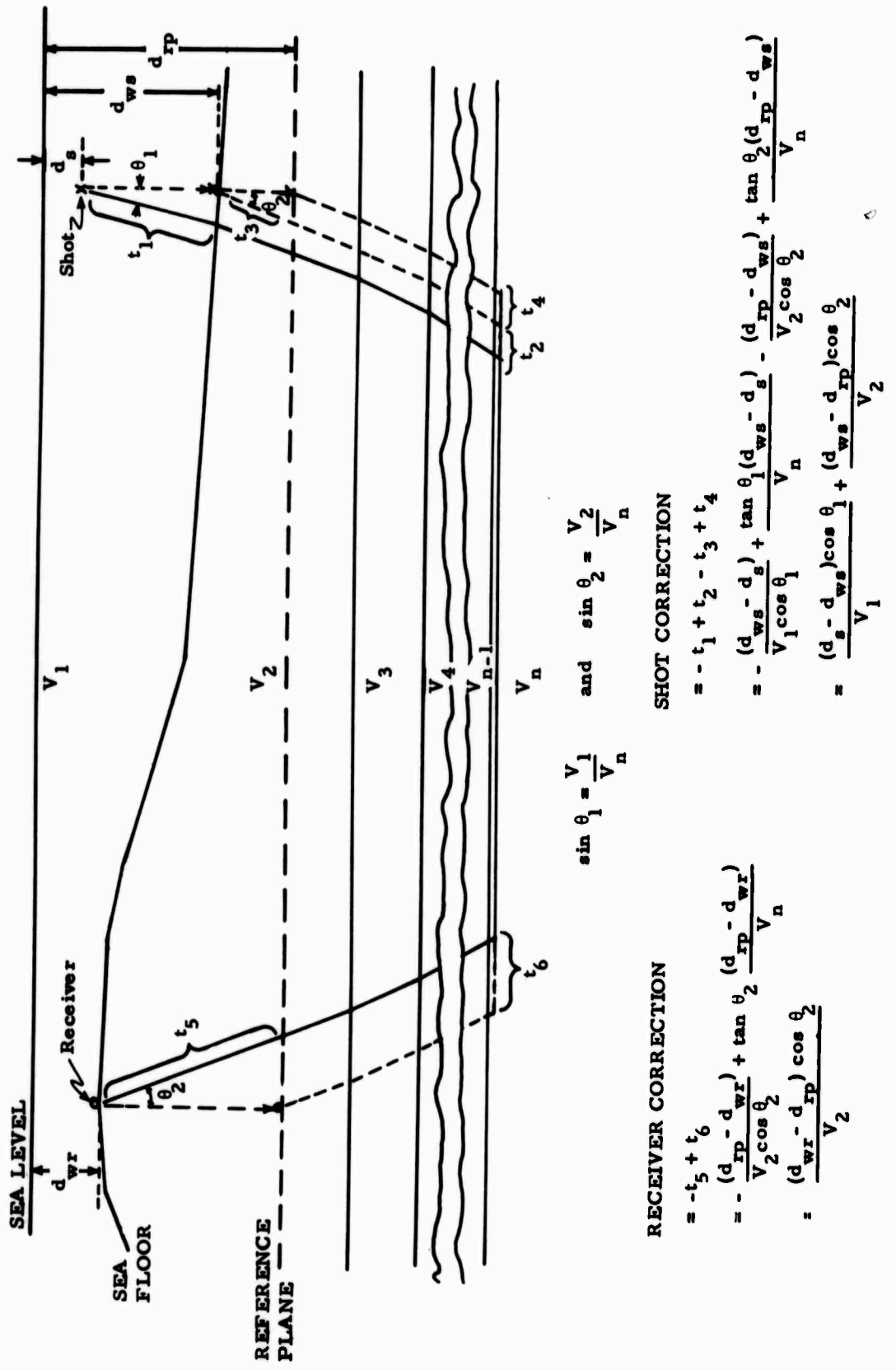


Figure II-1. Method of Reference-Plane Correction



S5-E33



S31 - E22

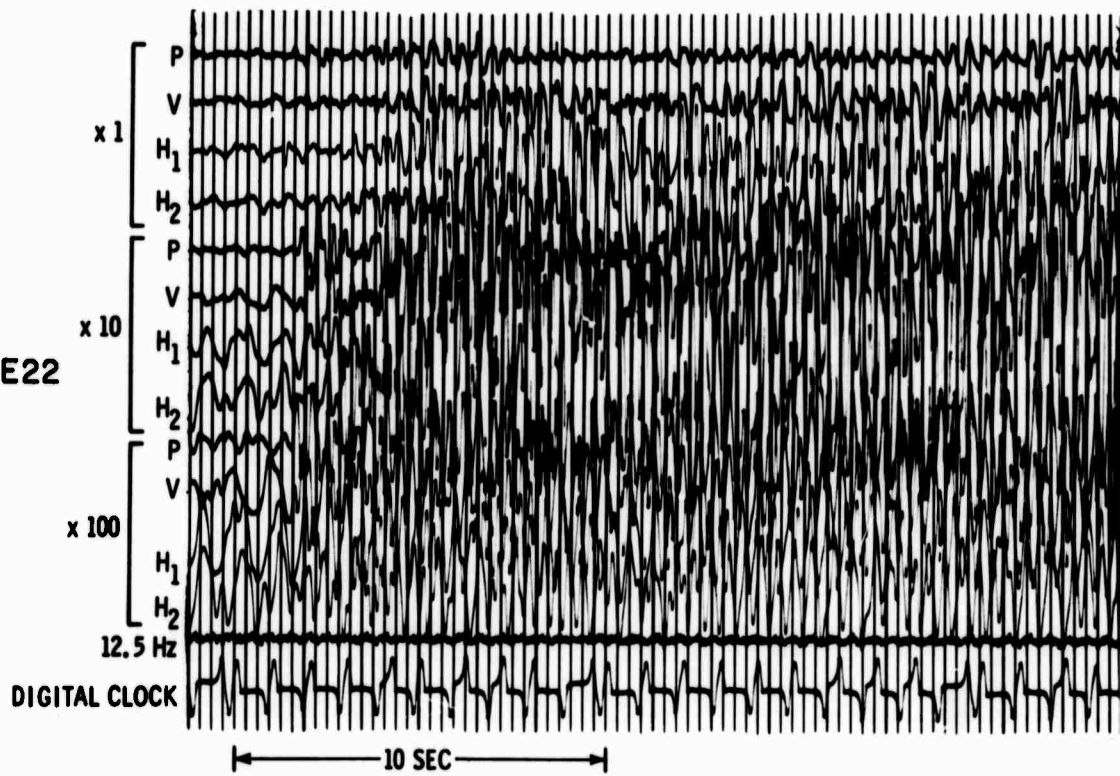


Figure II-2. Example of Digitized Field Data from OBS

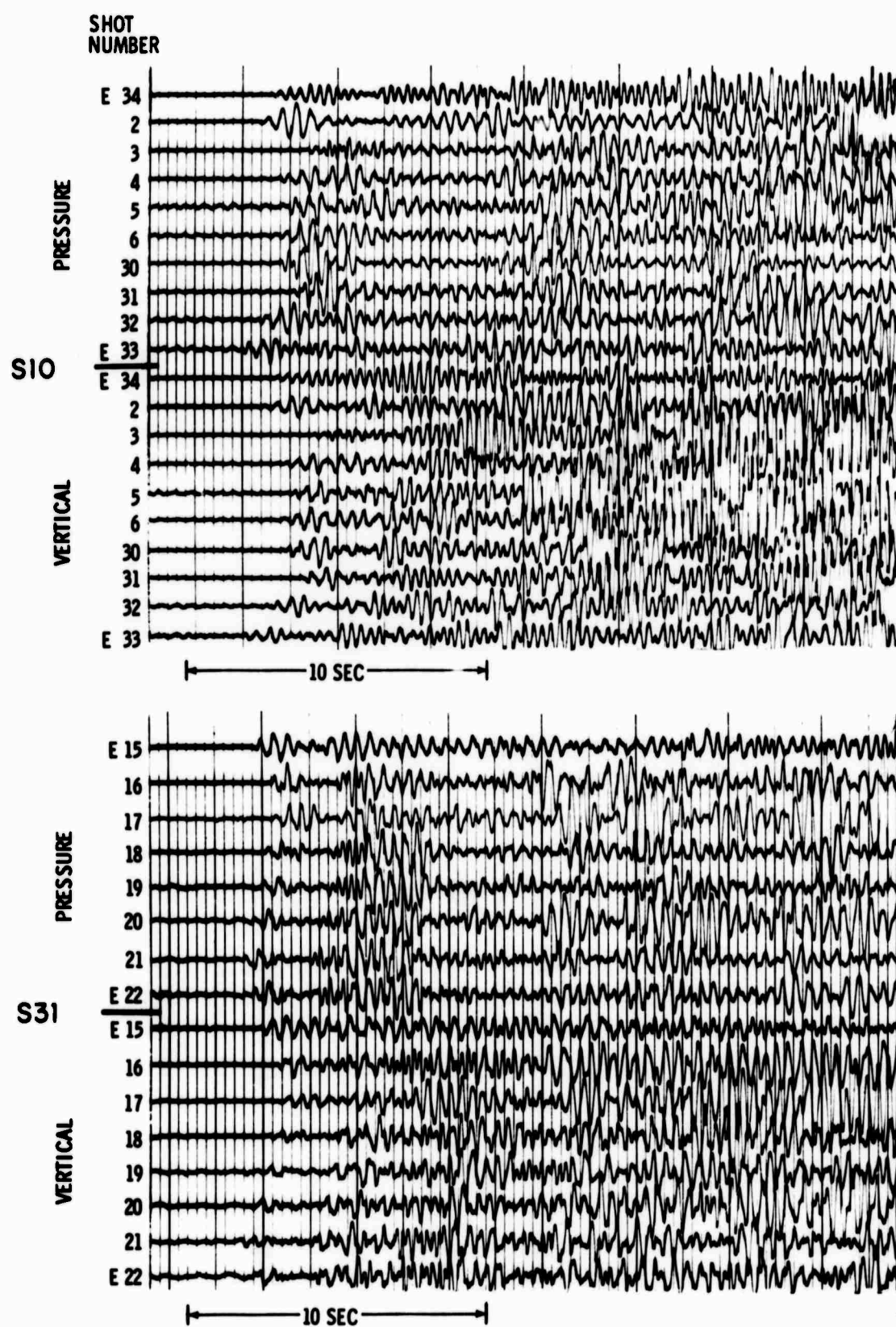


Figure II-3. Gathered Traces of All Shots Recorded at One Station,
Aligned at 8 km/sec with Trace Amplitudes Equalized

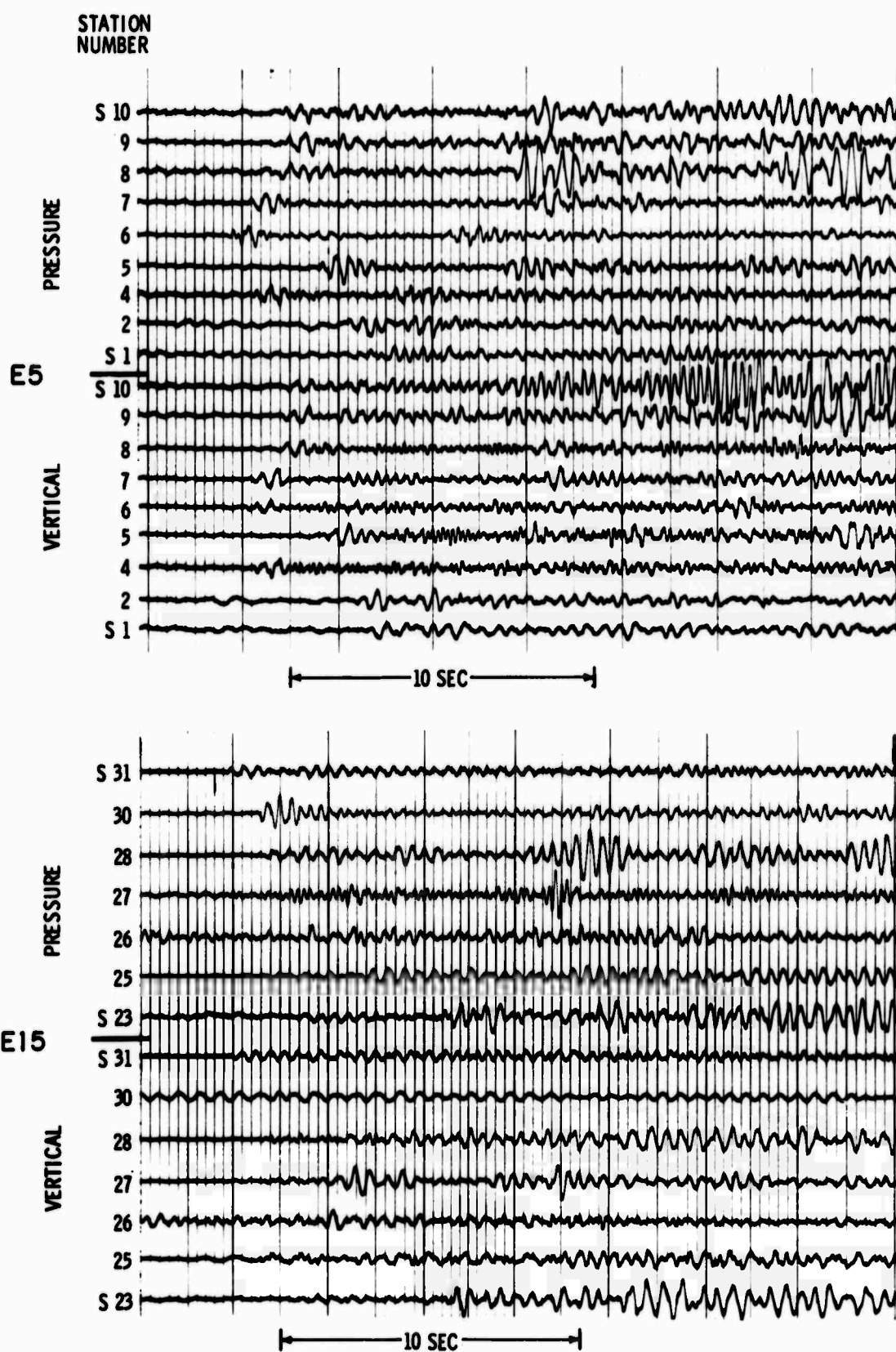


Figure II-4. Gathered Traces of One Shot Recorded at All Stations,
Aligned at 8 km/sec with Trace Amplitudes Equalized

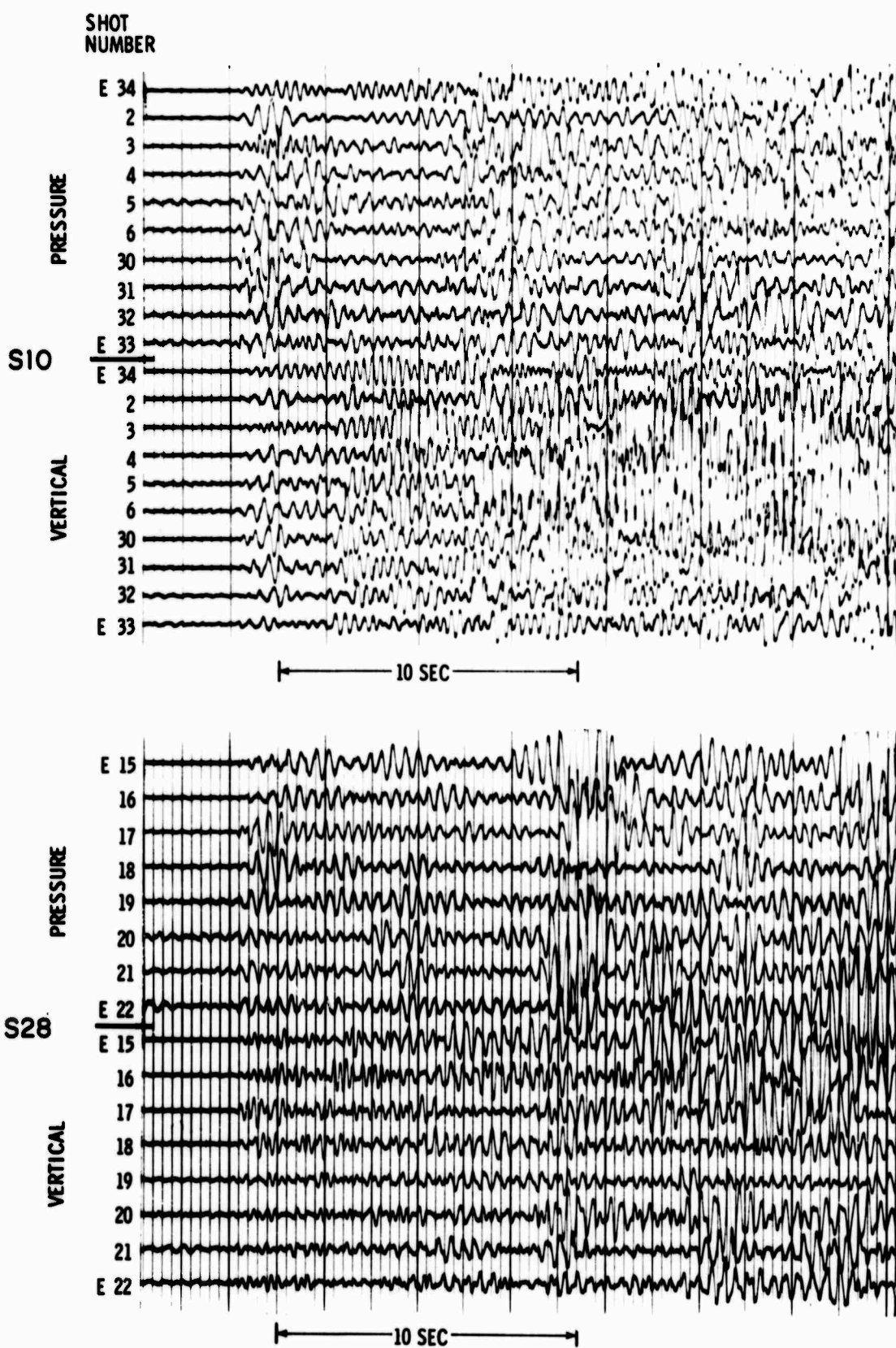


Figure II-5. Gathered Traces of All Shots Recorded at One Station,
Aligned Vertically with Trace Amplitudes Equalized

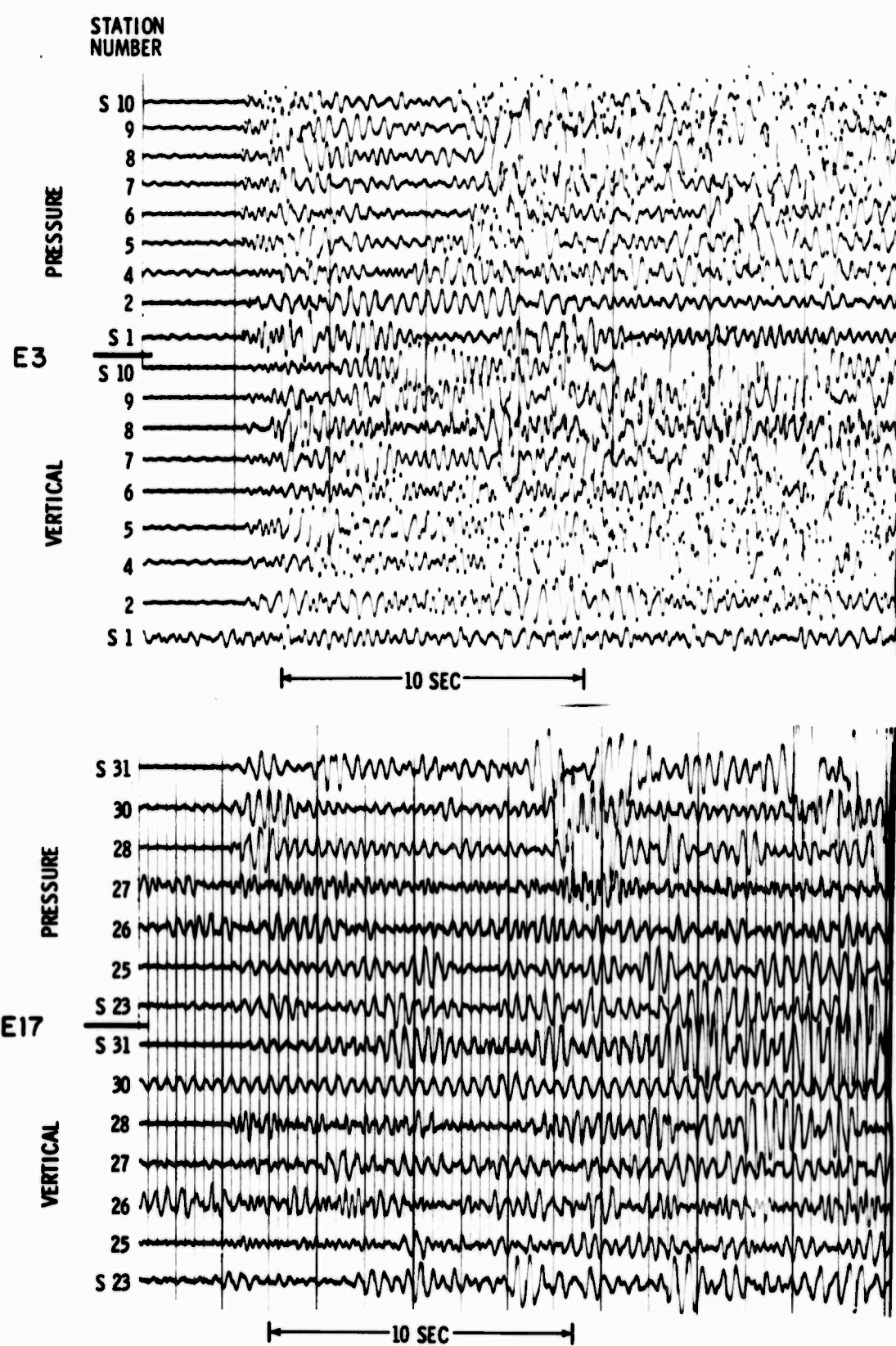


Figure II-6. Gathered Traces of One Shot Recorded at All Stations,
Aligned Vertically with Trace Amplitudes Equalized



SHOT
NUMBER

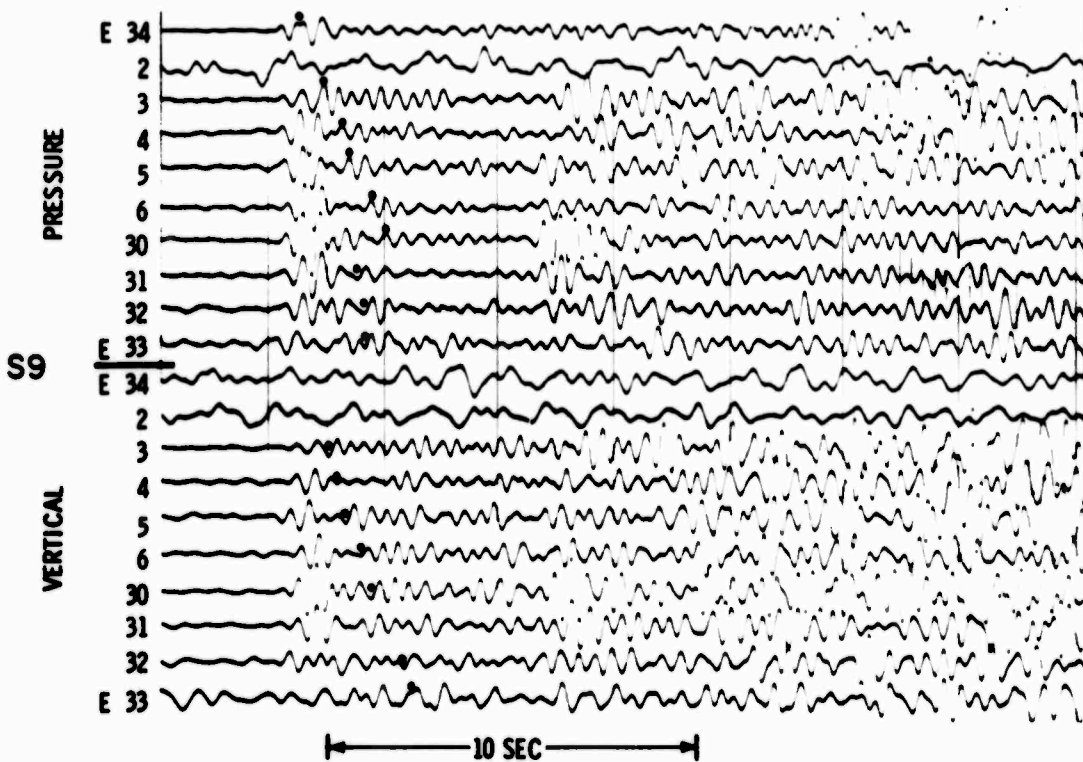
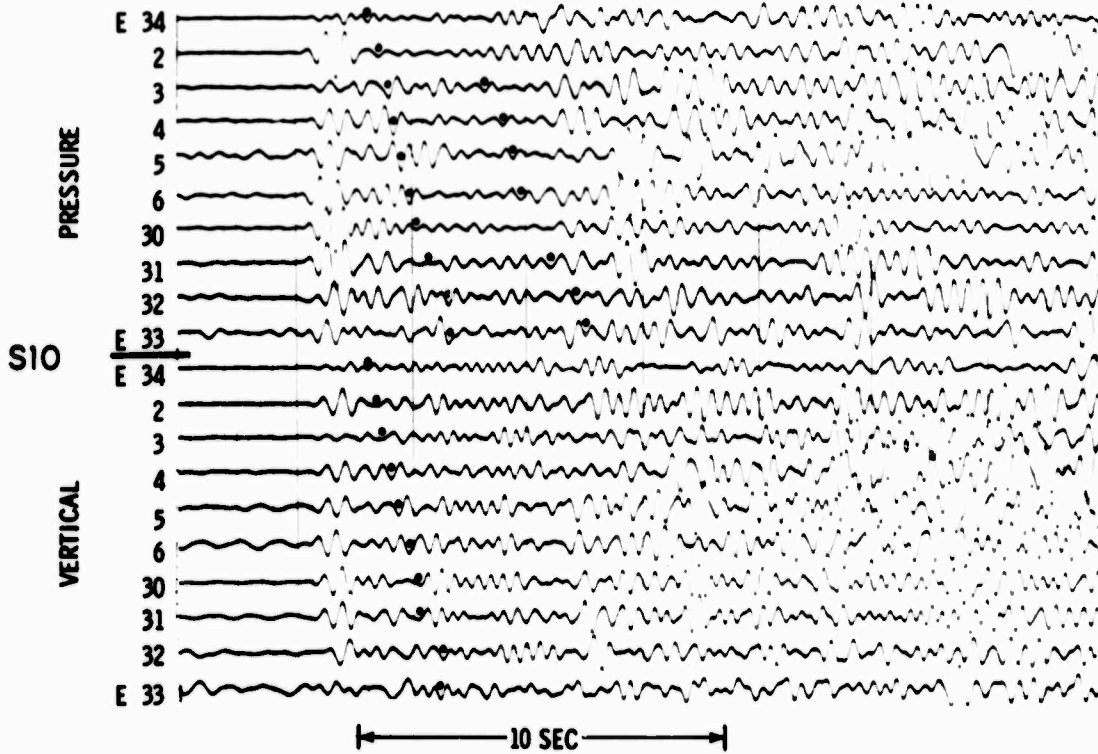


Figure II-7. Gathered Traces of All Shots Recorded at S10 (top)
and S9 (bottom)



SHOT
NUMBER

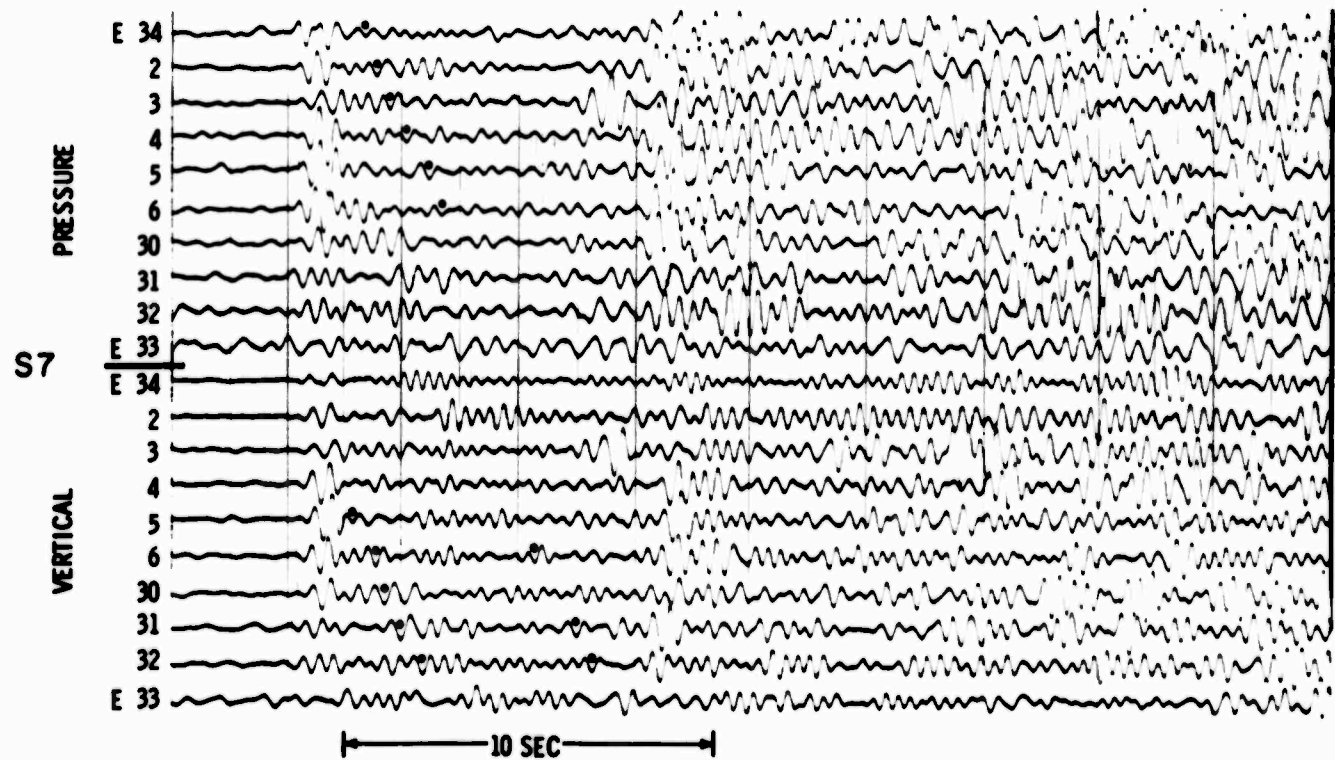
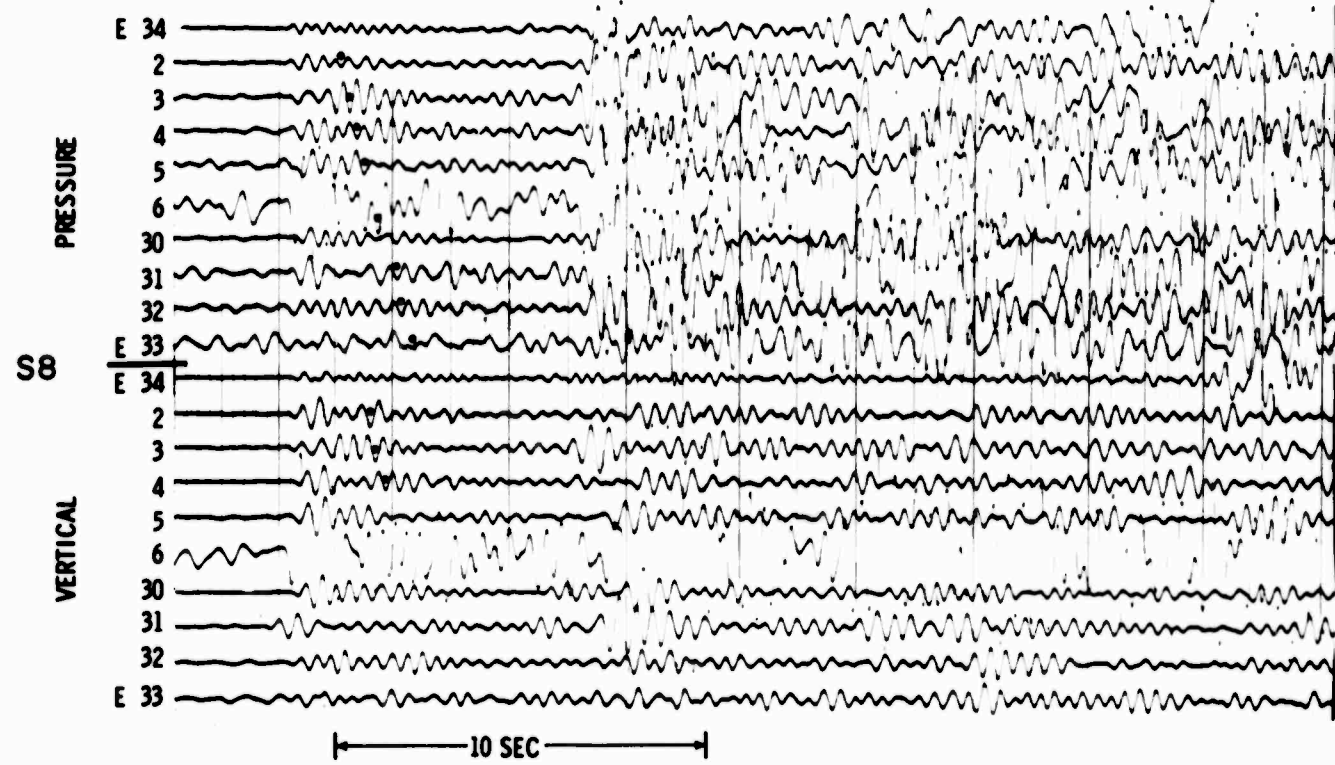


Figure II-8. Gathered Traces of All Shots Recorded at S8 (top) and S7 (bottom)



SHOT
NUMBER

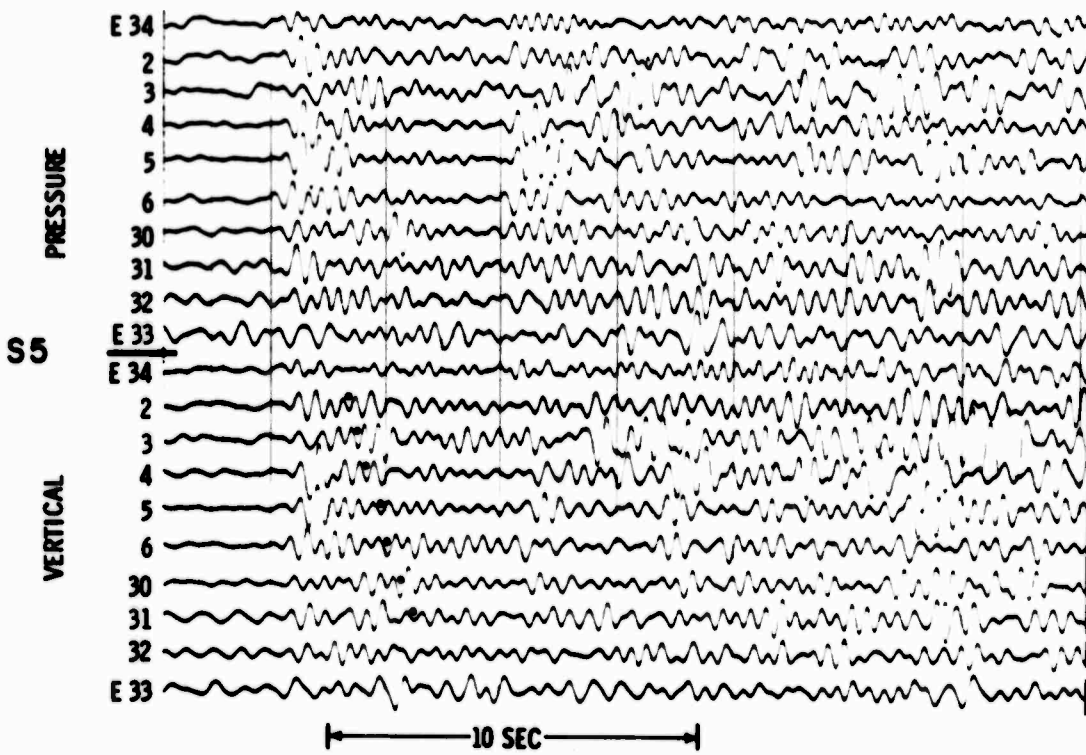
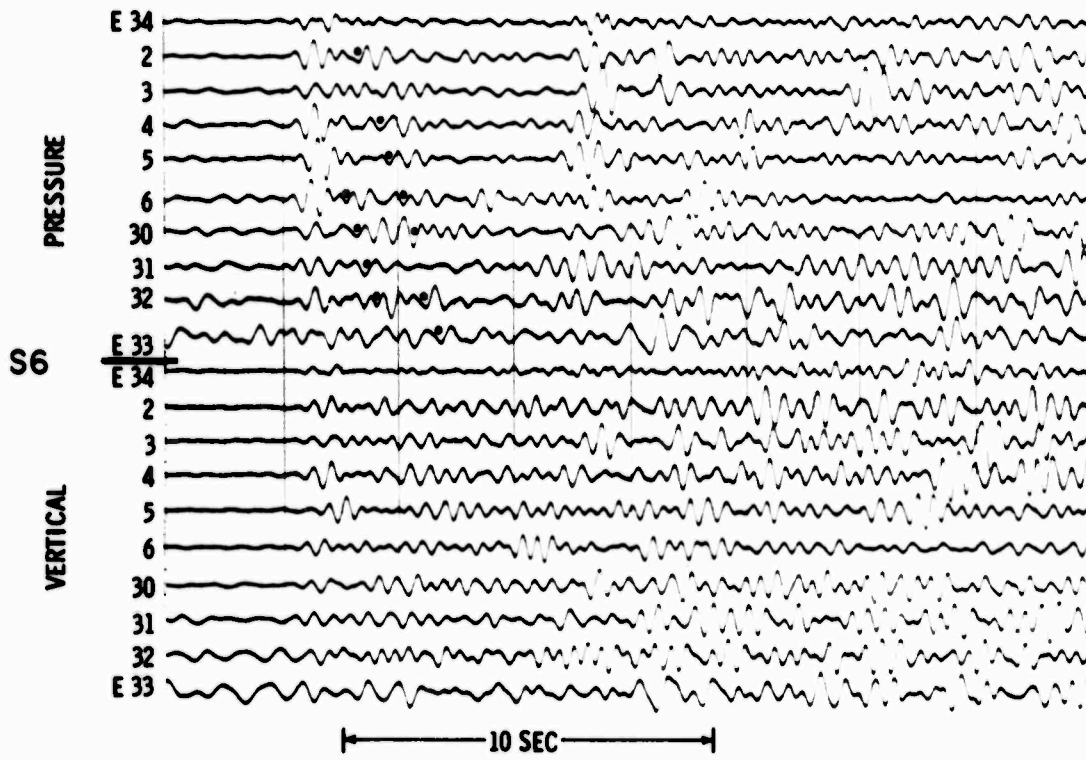


Figure II-9. Gathered Traces of All Shots Recorded at S6 (top) and S5 (bottom)

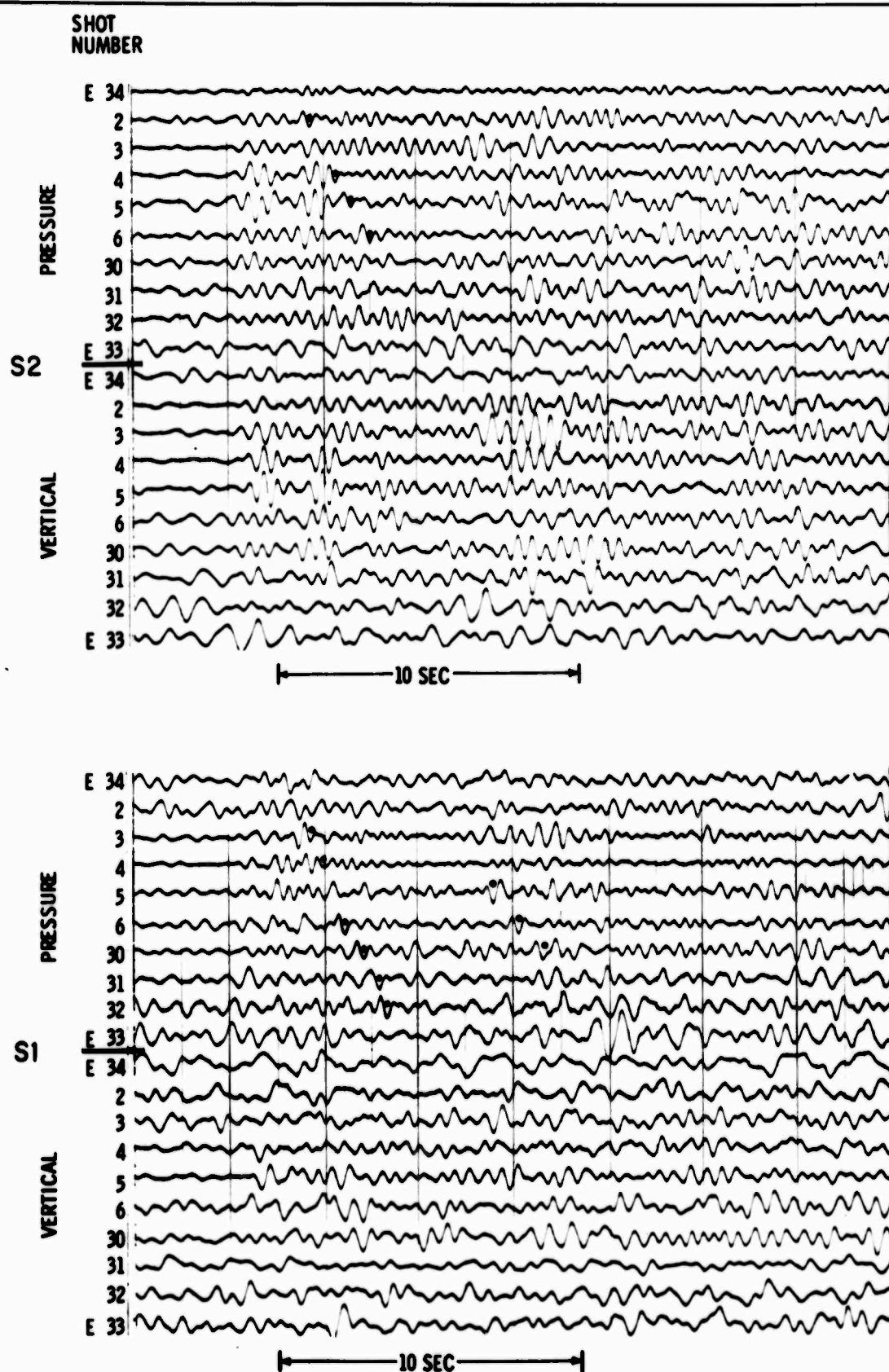


Figure II-10. Gathered Traces of All Shots Recorded at S2 (top) and S1 (bottom)



SHOT
NUMBER

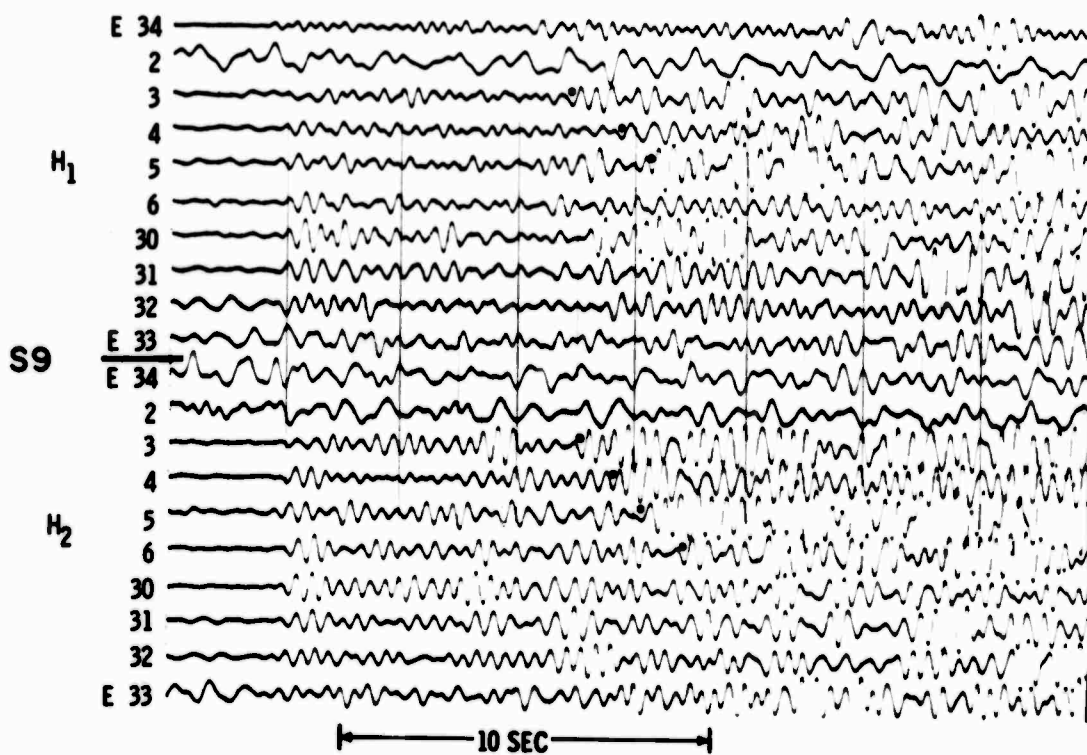
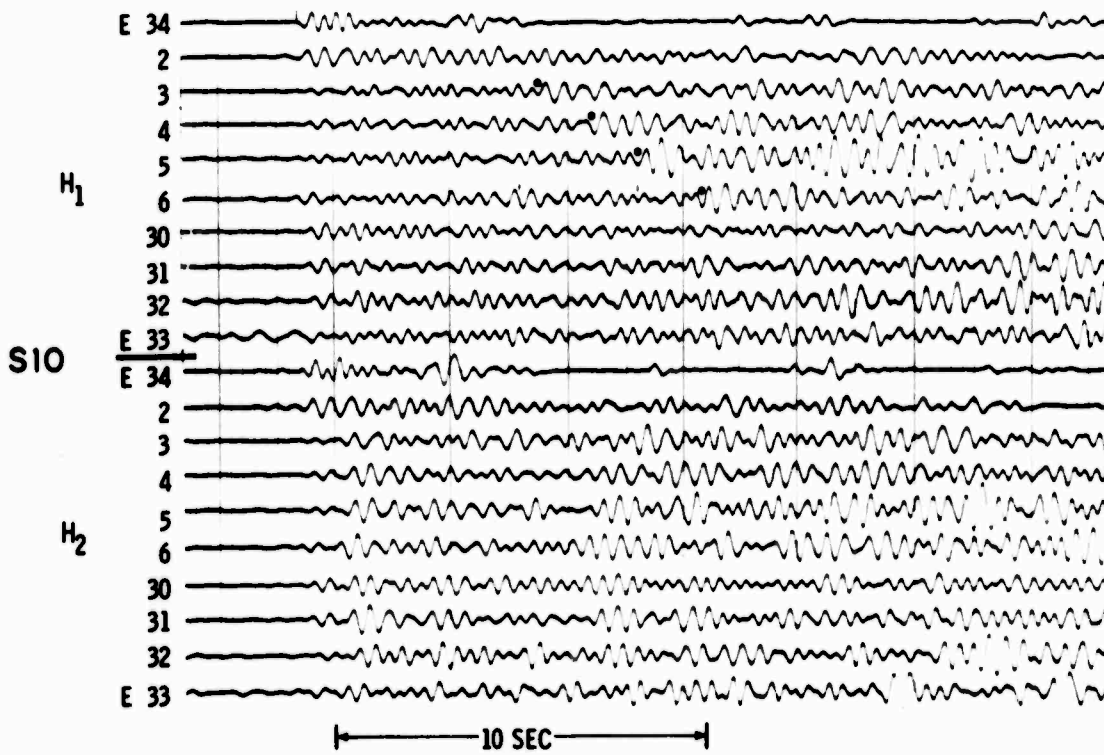


Figure II-11. Gathered Traces of All Shots Recorded at S10 (top) and S9 (bottom), Horizontal Instruments



SHOT
NUMBER

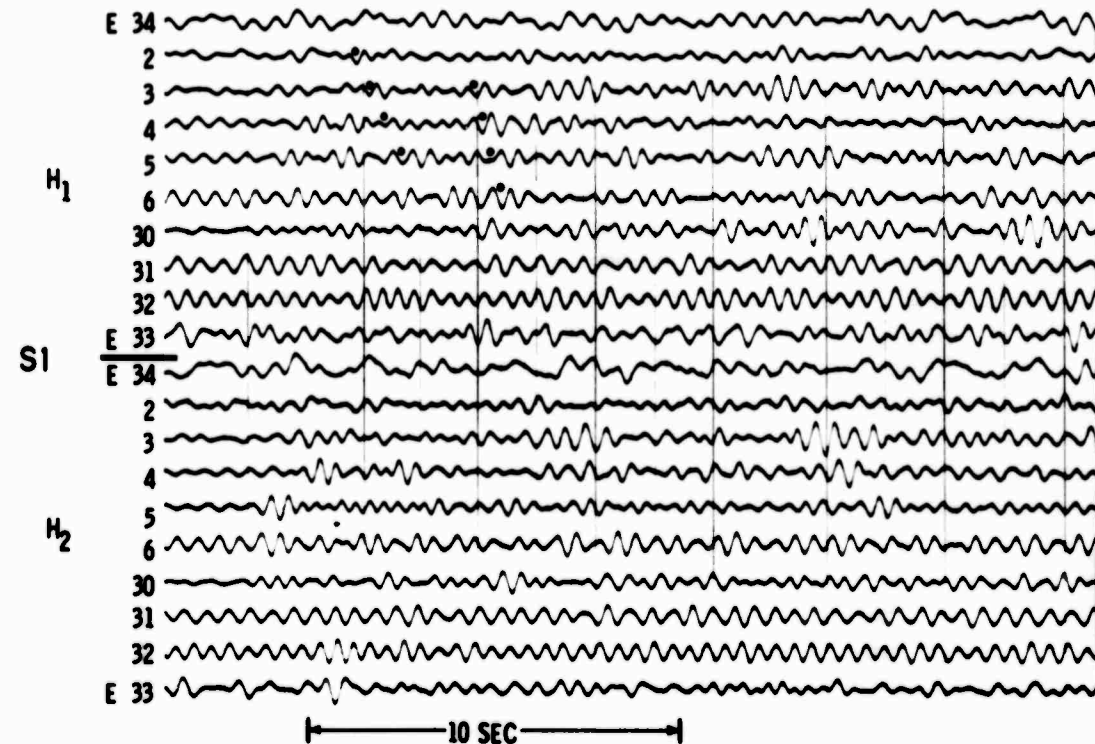
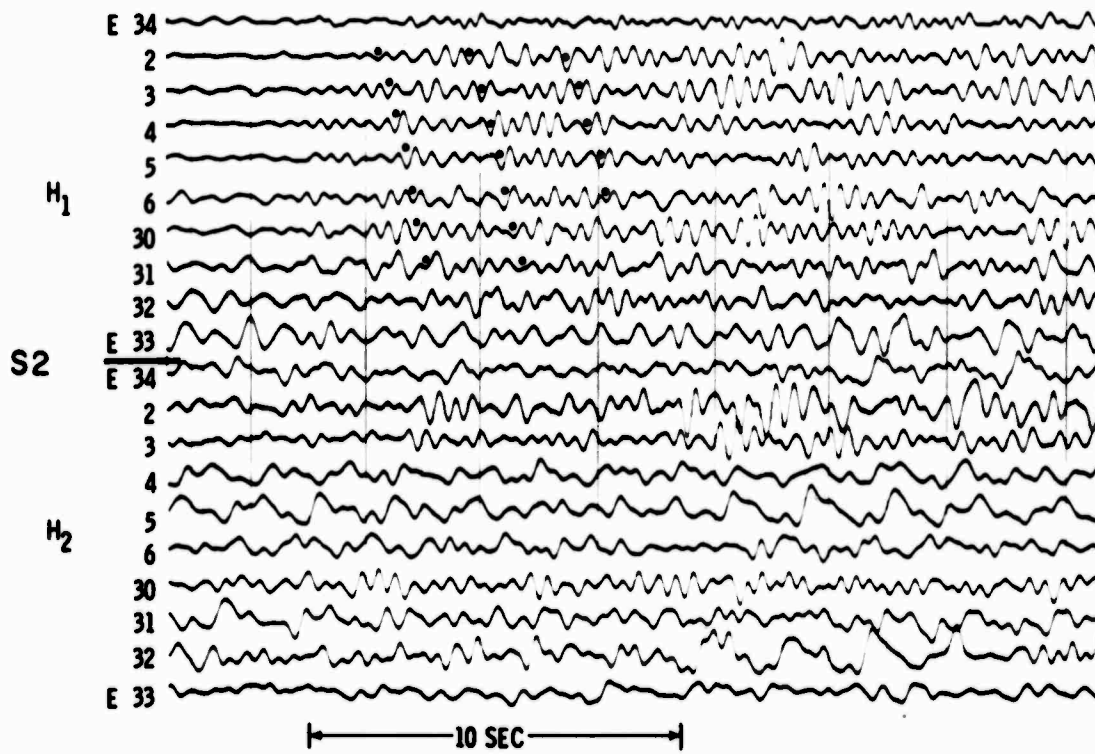


Figure II-12. Gathered Traces of All Shots Recorded at S2 (top) and S1 (bottom), Horizontal Instruments

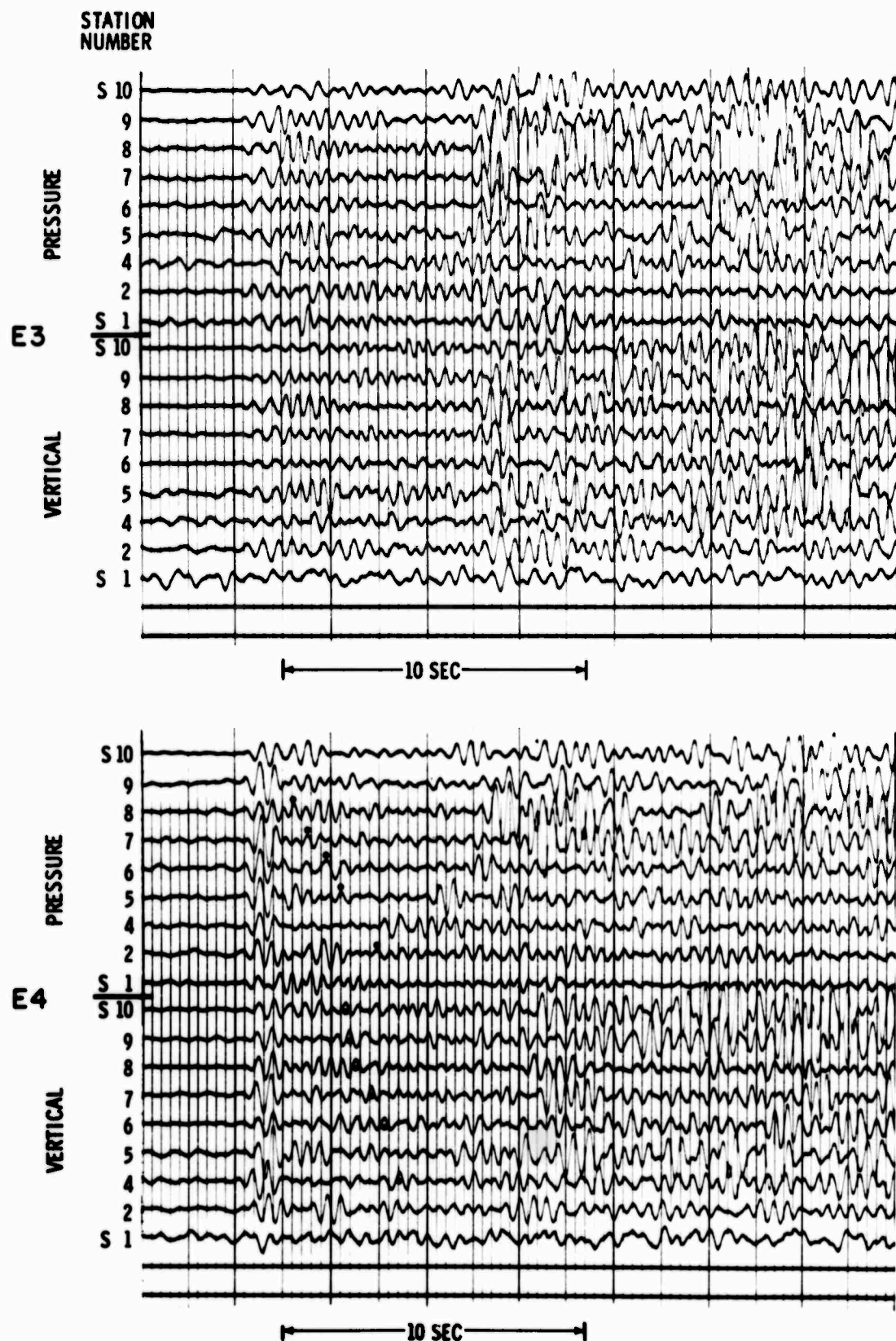


Figure II-13. Gathered Traces of E3 (top) and E4 (bottom)
Recorded at All Stations

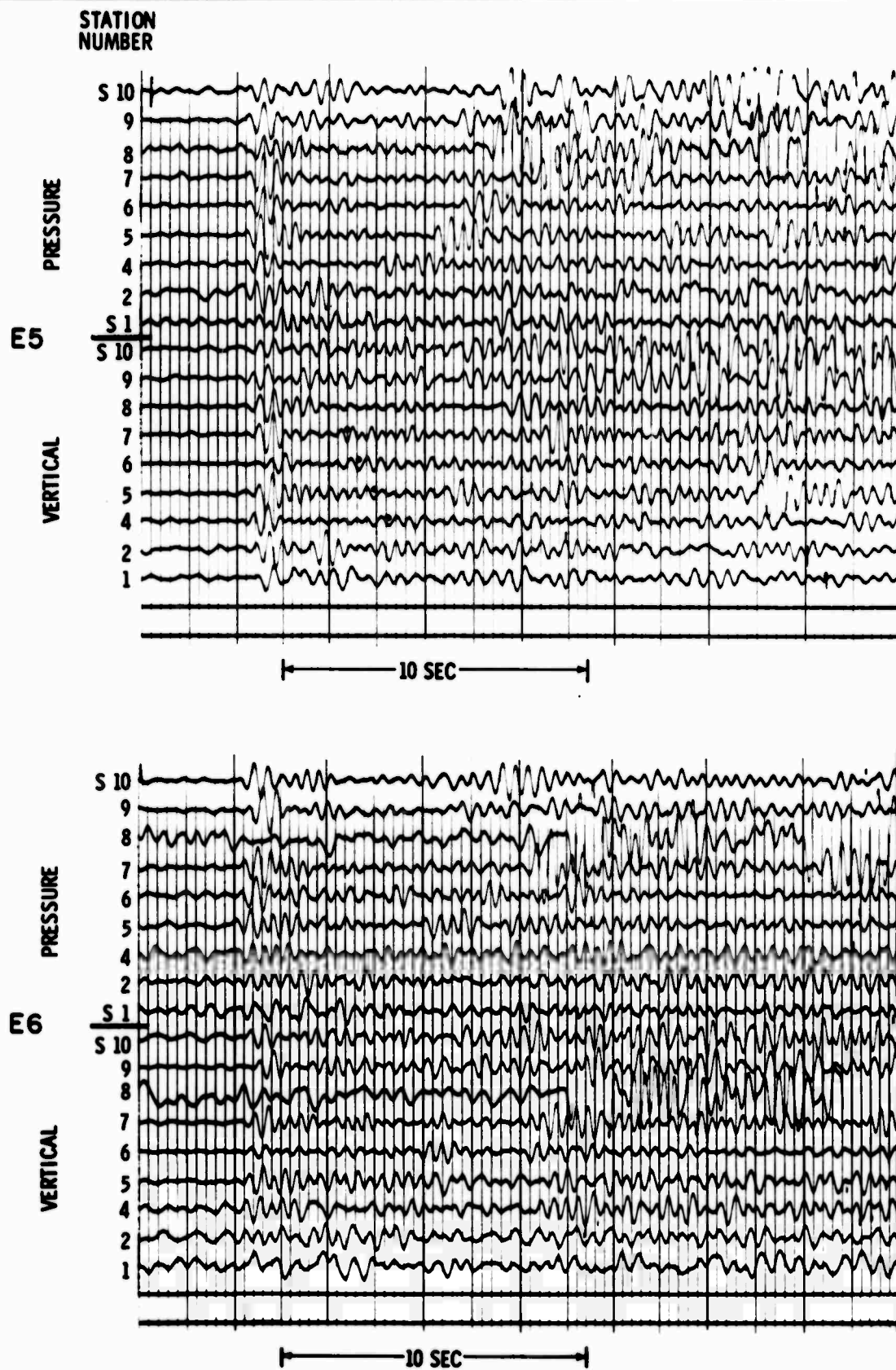


Figure II-14. Gathered Traces of E5 (top) and E6 (bottom)
Recorded at All Stations

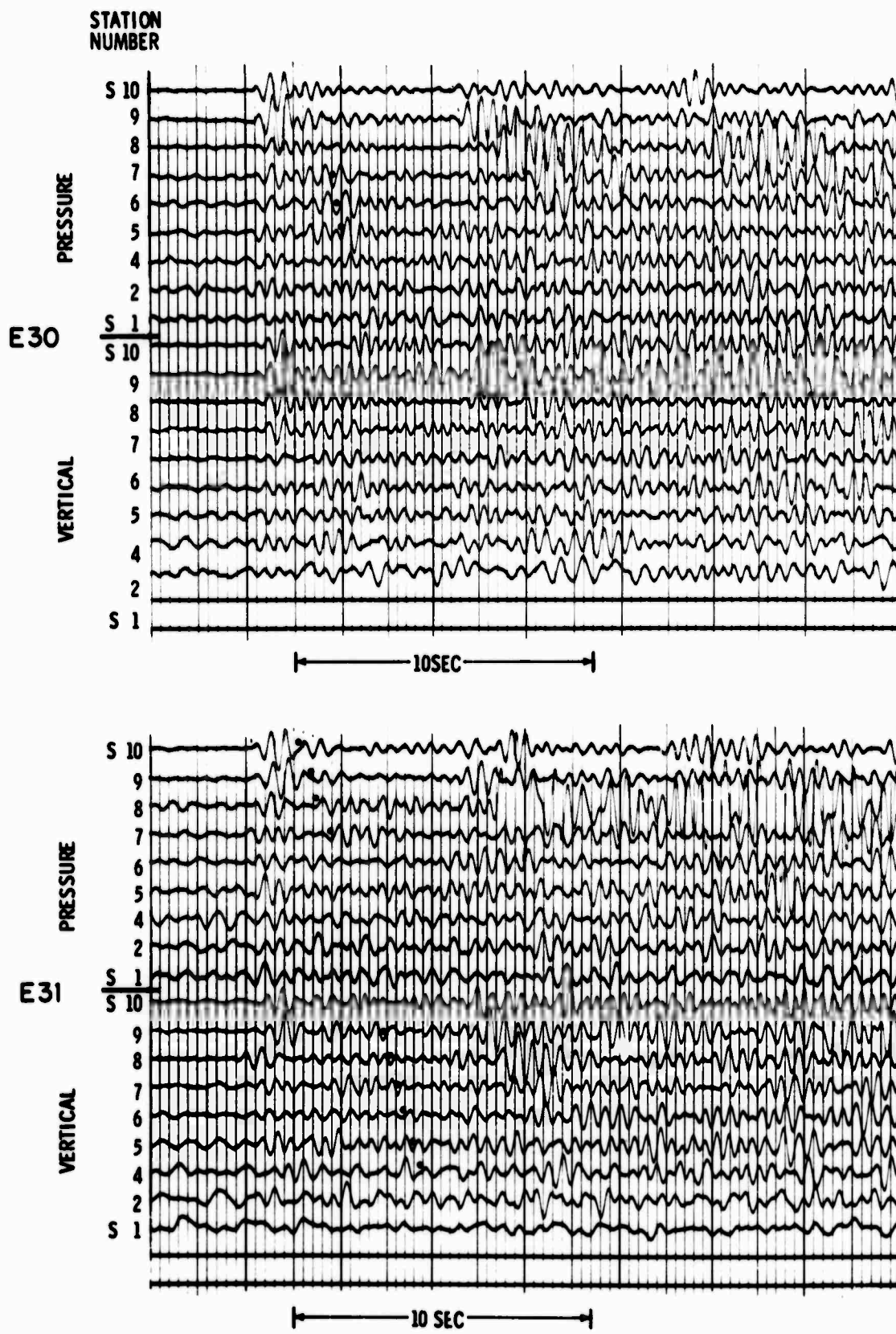


Figure II-15. Gathered Traces of E30 (top) and E31 (bottom)
Recorded at All Stations

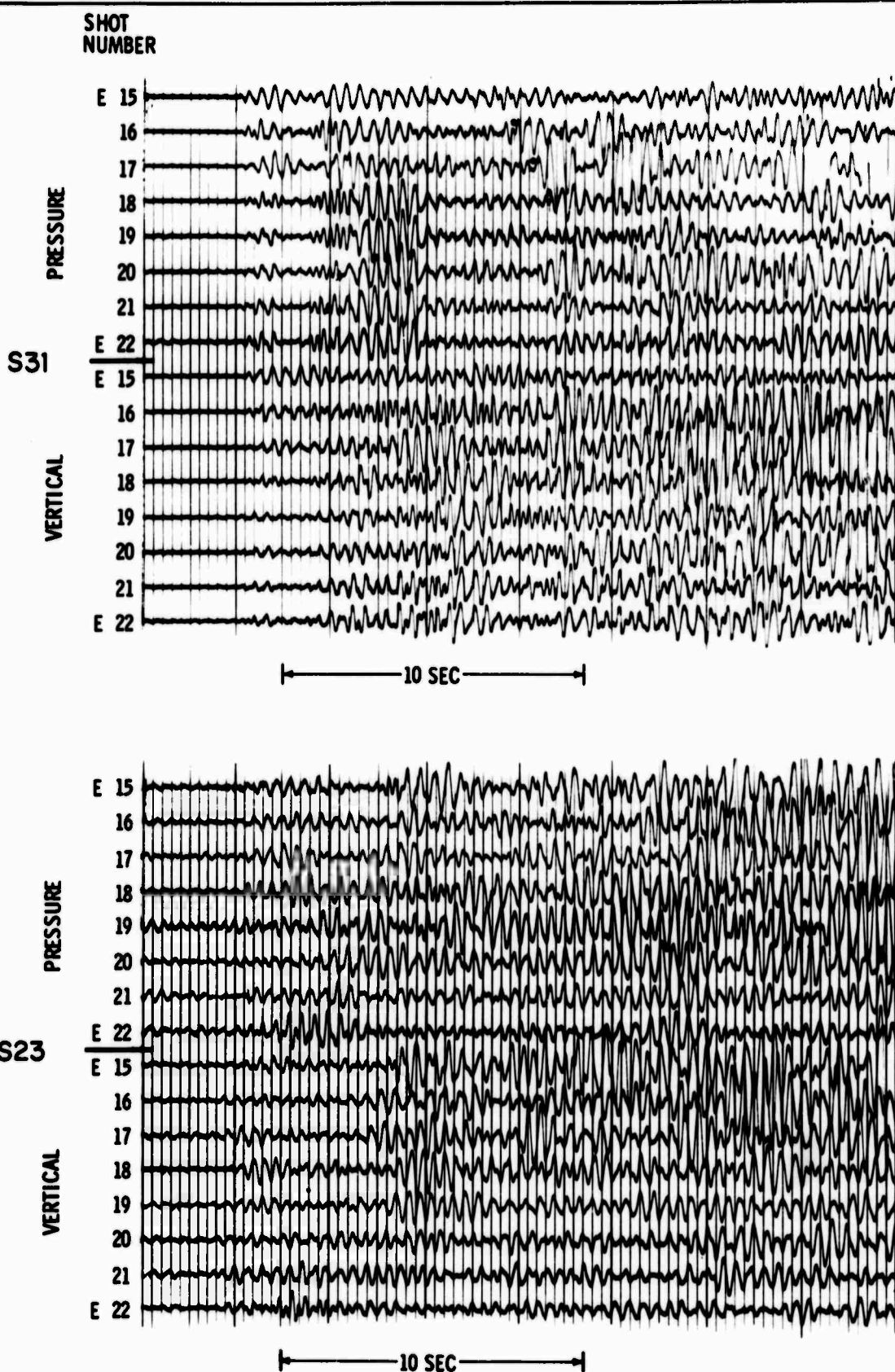


Figure II-16. Gathered Traces of All Shots Recorded at S31 (top) and S23 (bottom)

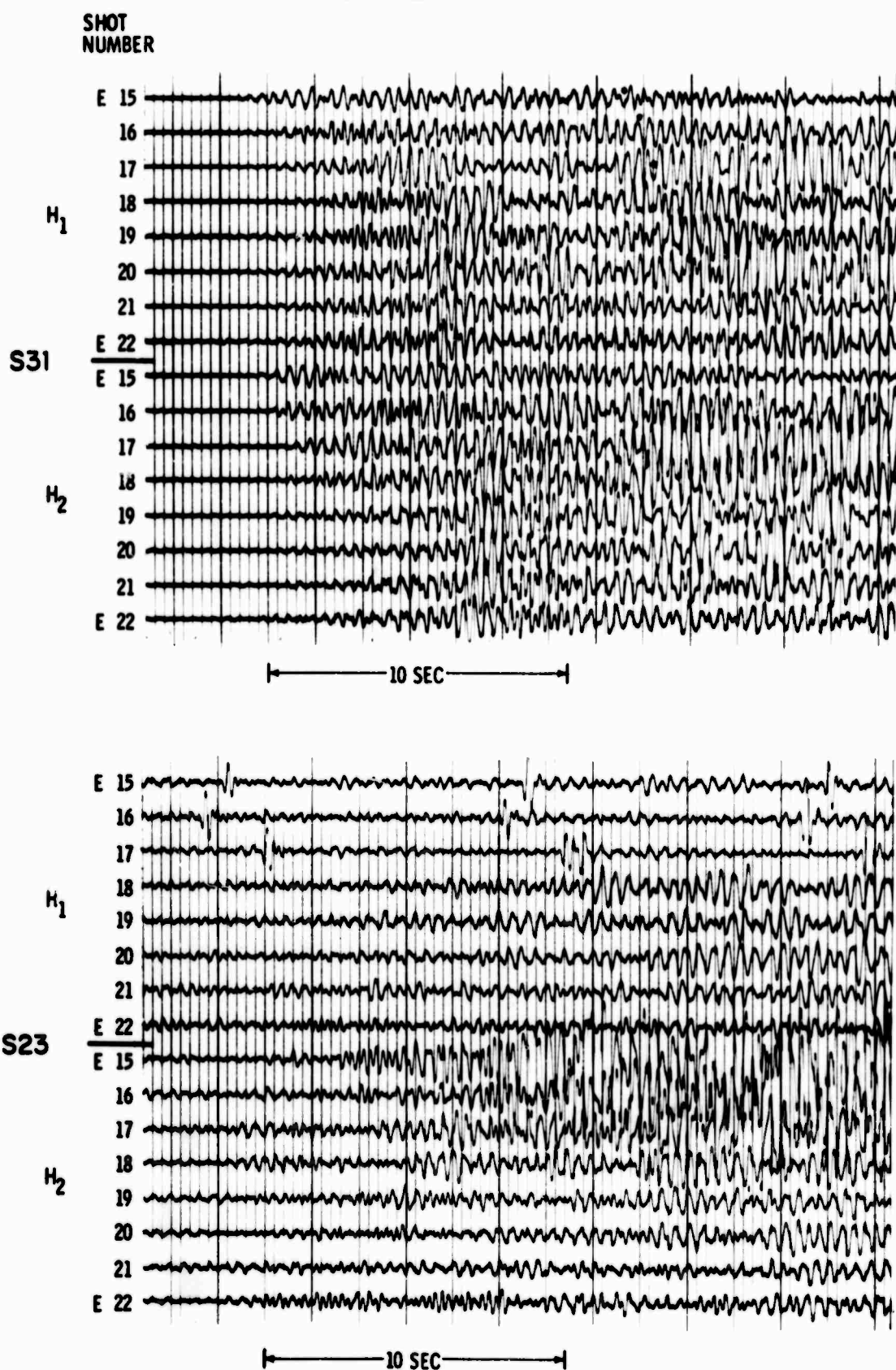
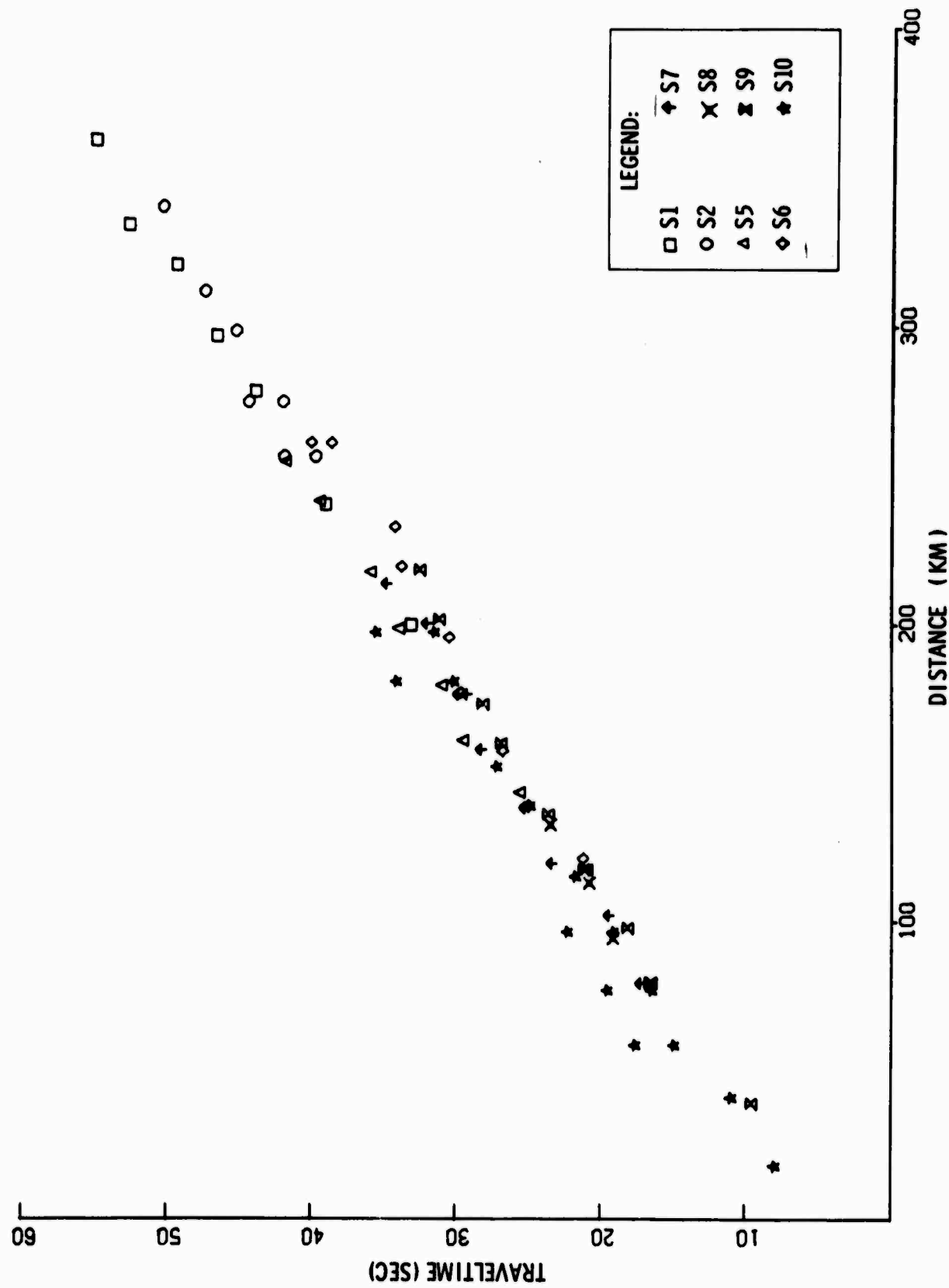


Figure II-17. Gathered Traces of All Shots Recorded at S31 (top) and S23 (bottom), Horizontal Instruments



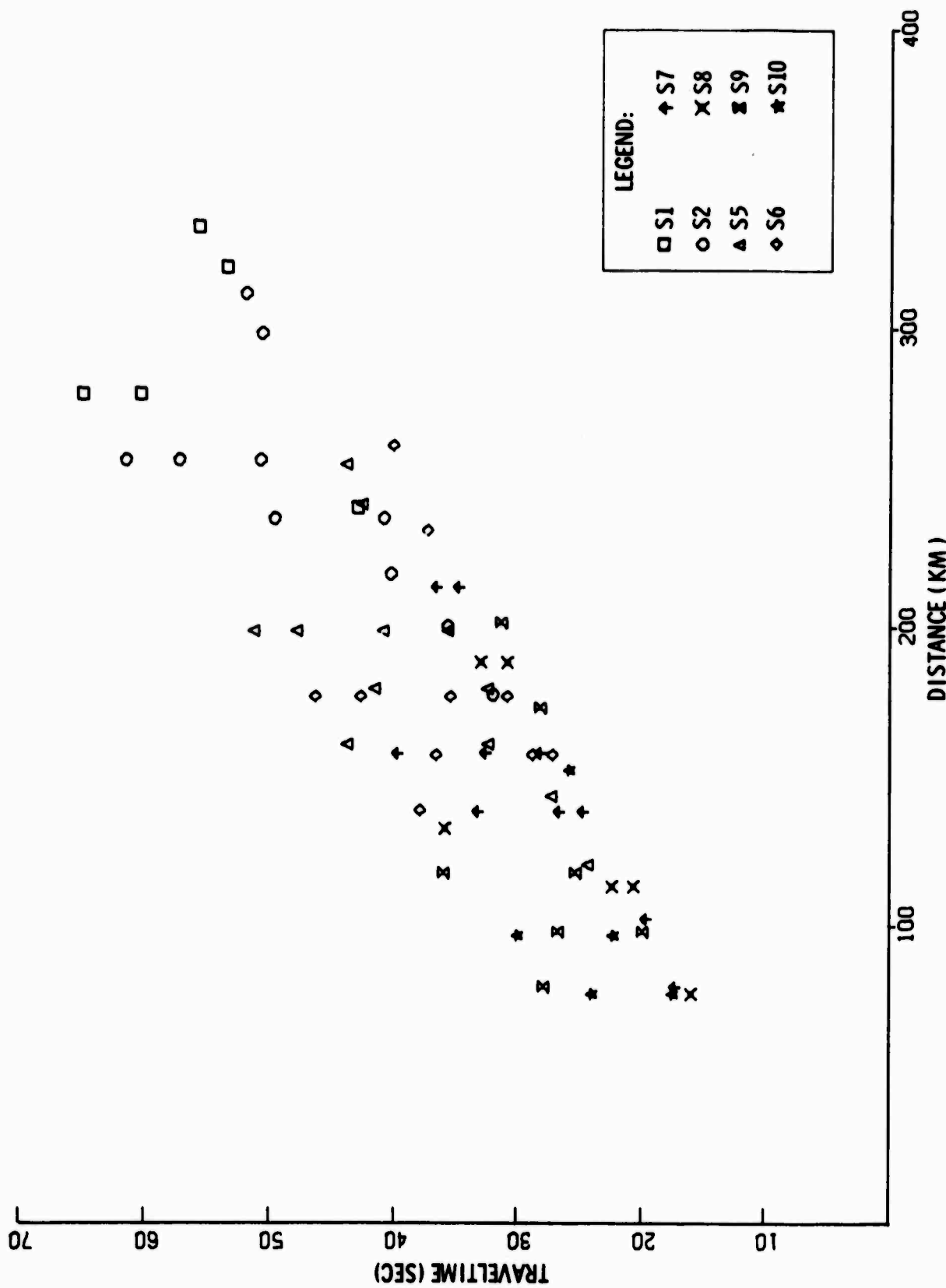


Figure II-19. Raw Traveltimes of Phase I Secondary Arrivals for Each Shot Recorded at All Stations

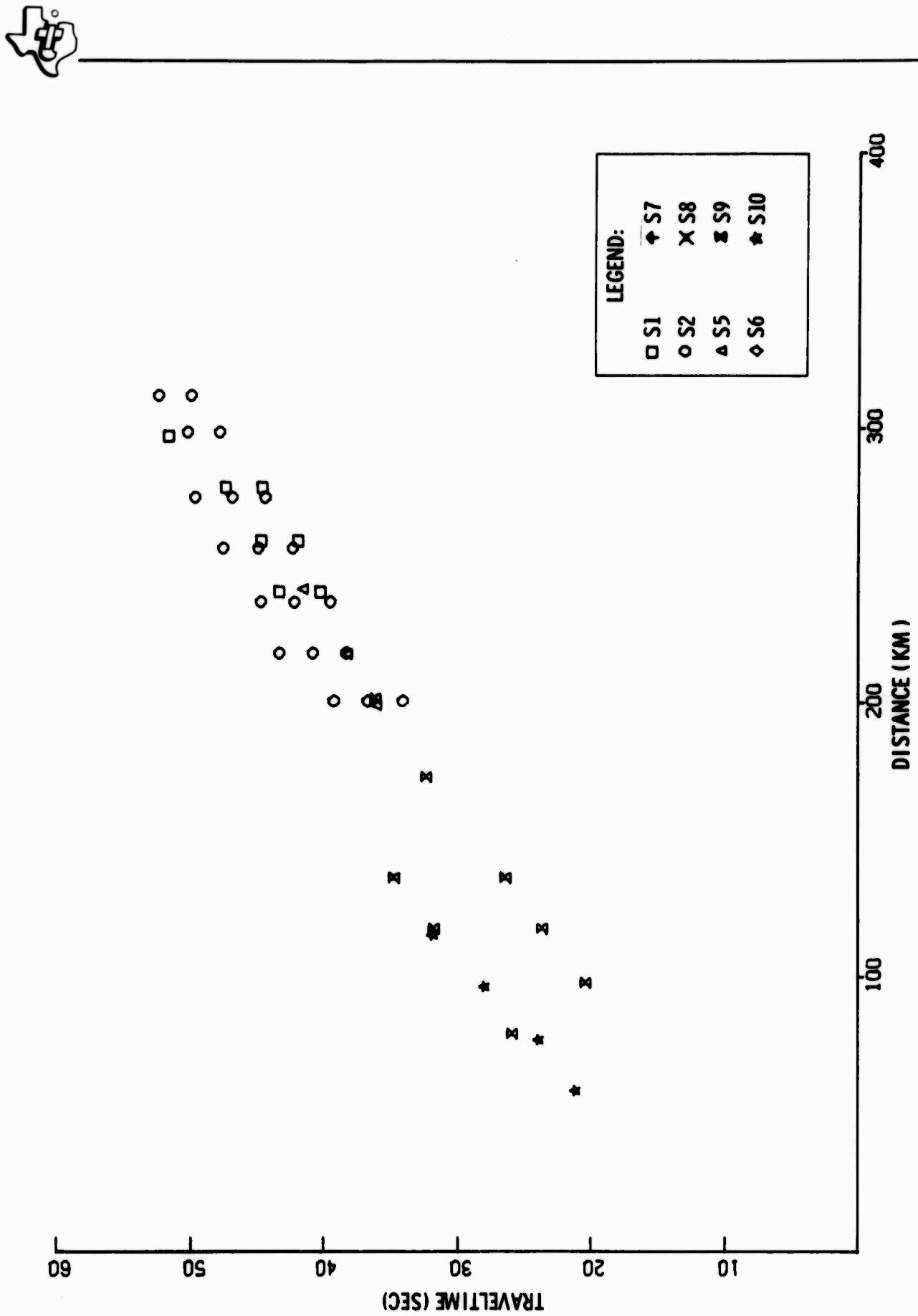


Figure II-20. Raw Traveltimes of Phase I Secondary Arrivals, Horizontal Instruments

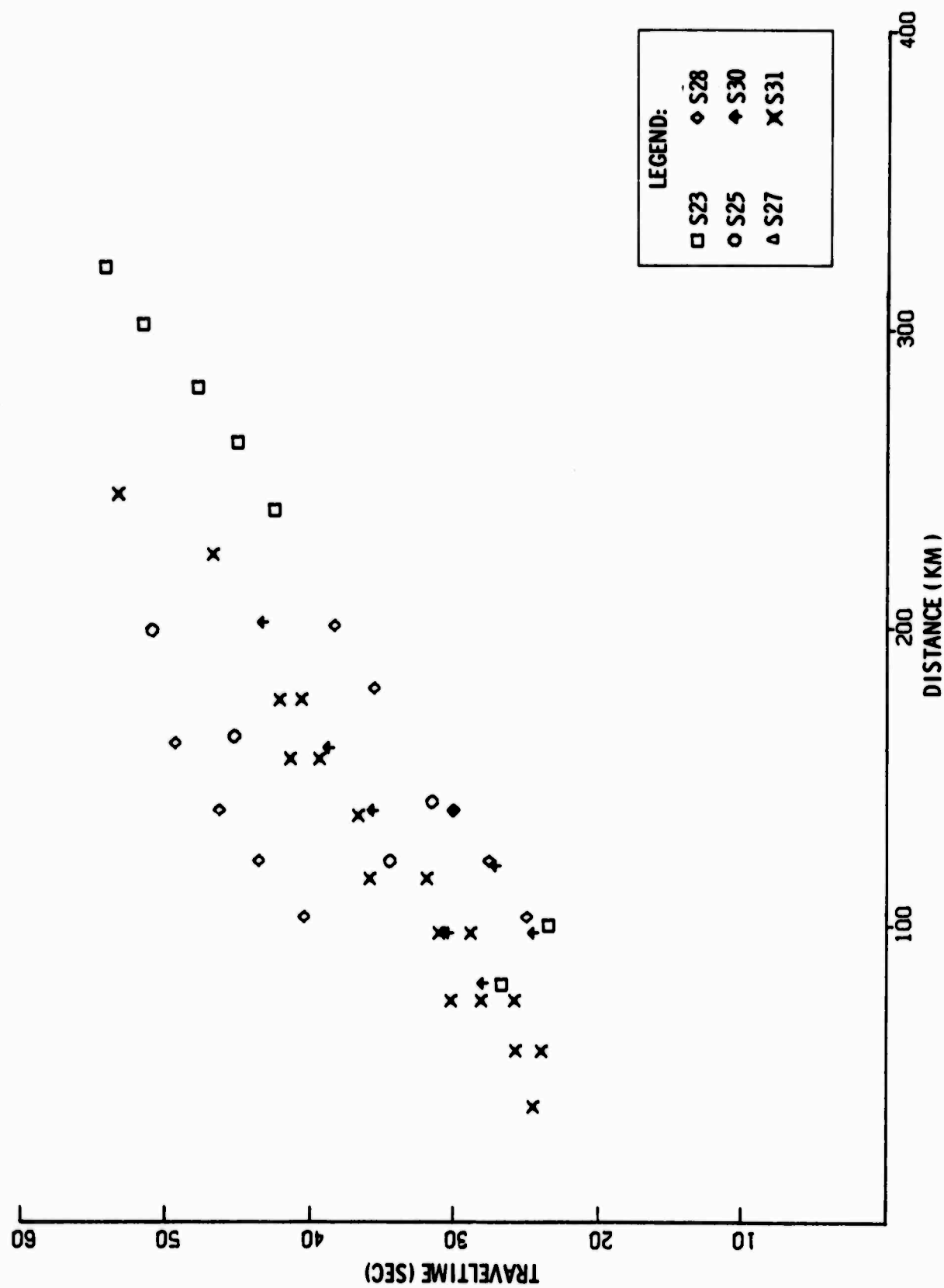


Figure II-21. Raw Traveltimes of Phase III Secondary Arrivals

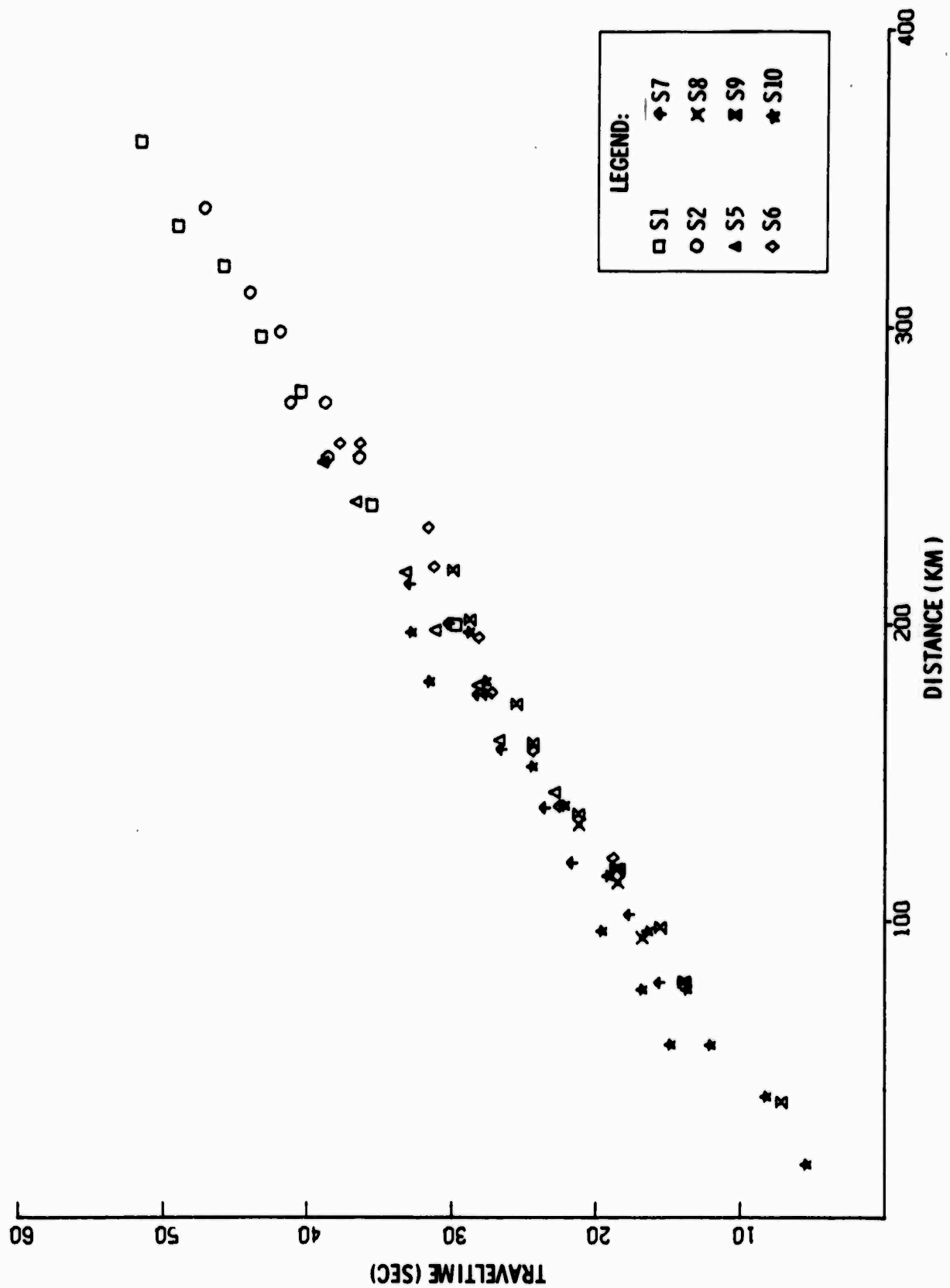


Figure II-22. Corrected Traveltimes of Phase I Secondary Arrivals
for All Shots Recorded at Each Station

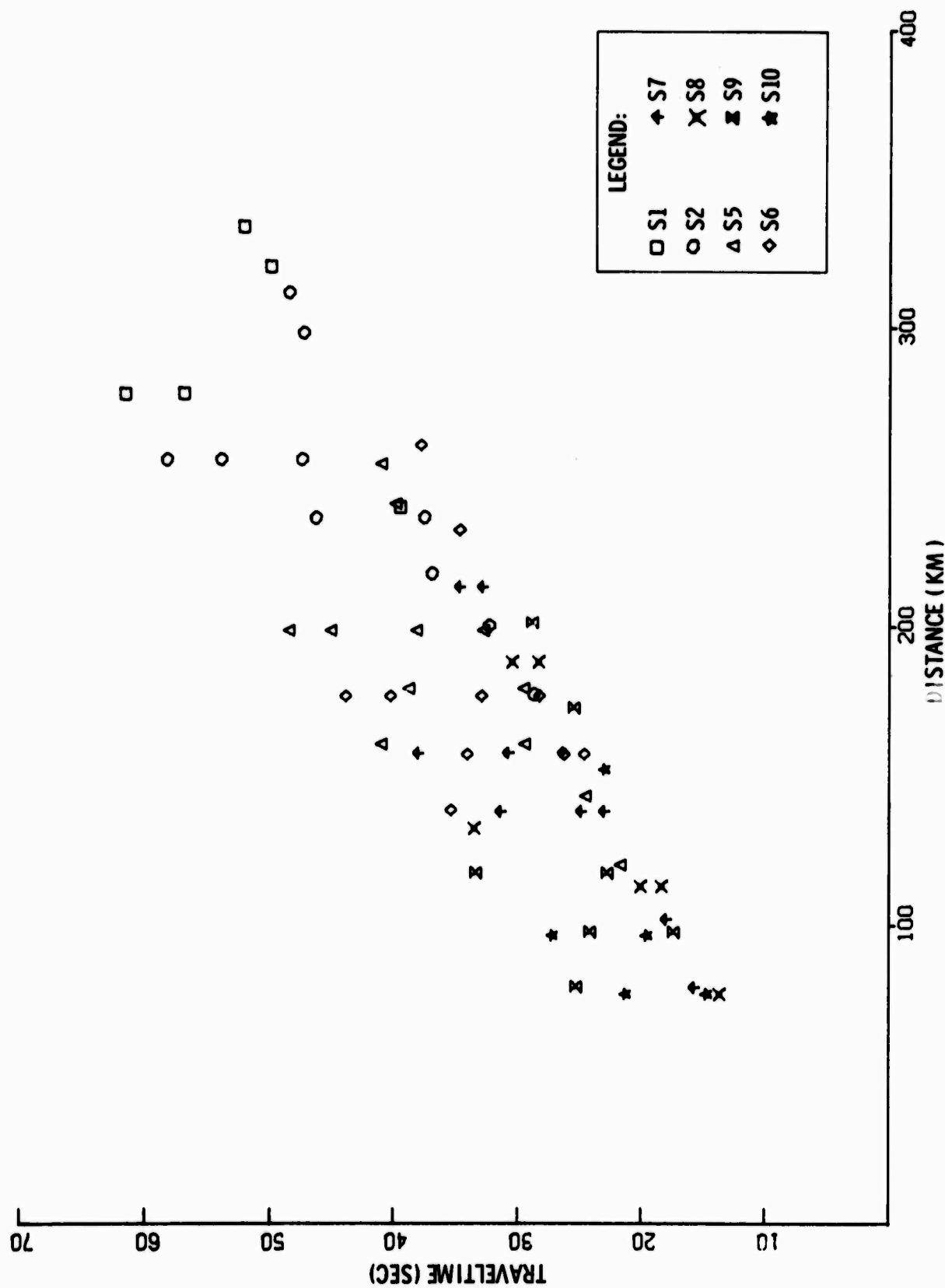


Figure II-23. Corrected Traveltimes of Phase I Secondary Arrivals for Each Shot Recorded at All Stations

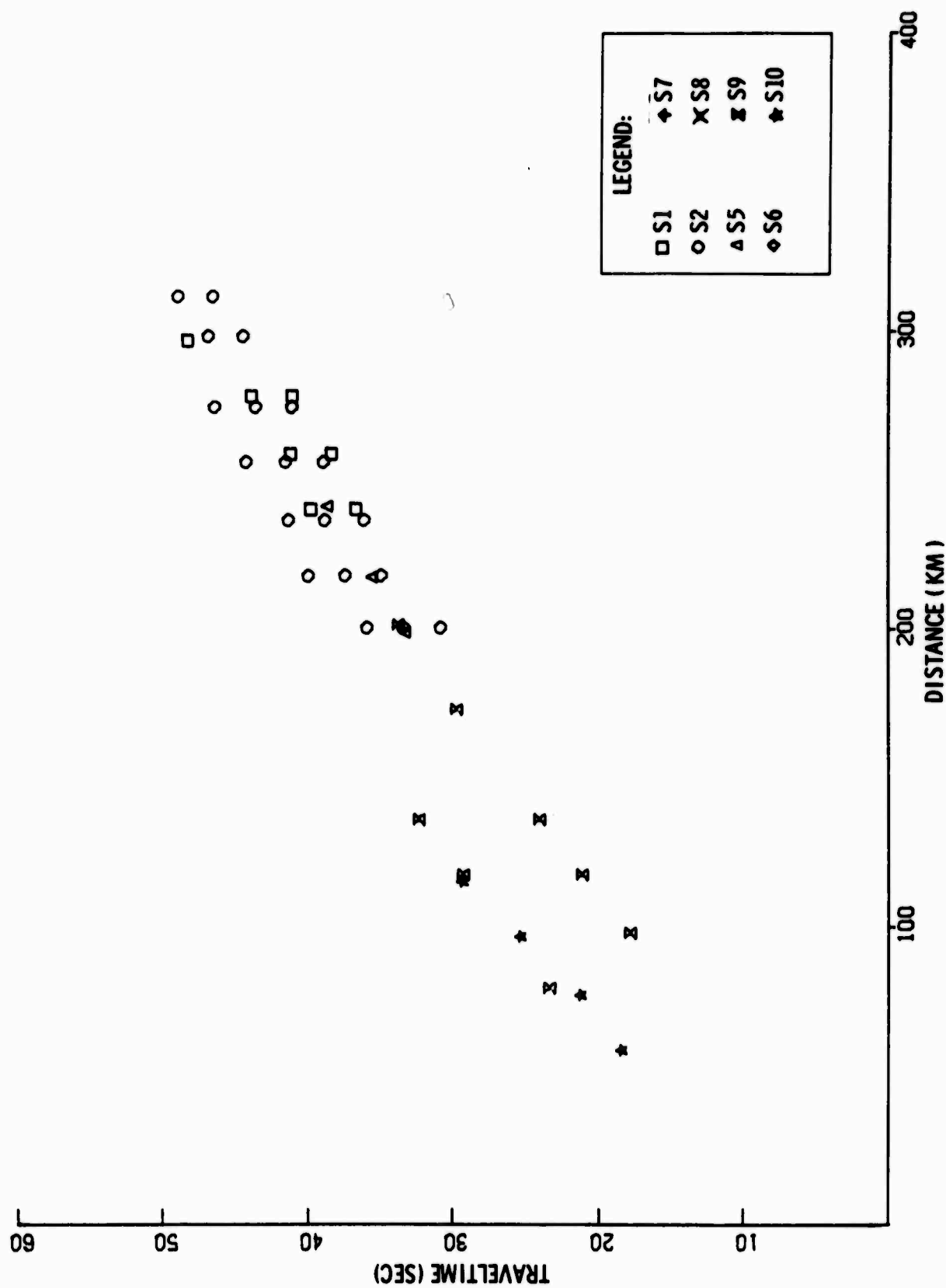


Figure II-24. Corrected Traveltimes of Phase I Secondary Arrivals,
Horizontal Instruments

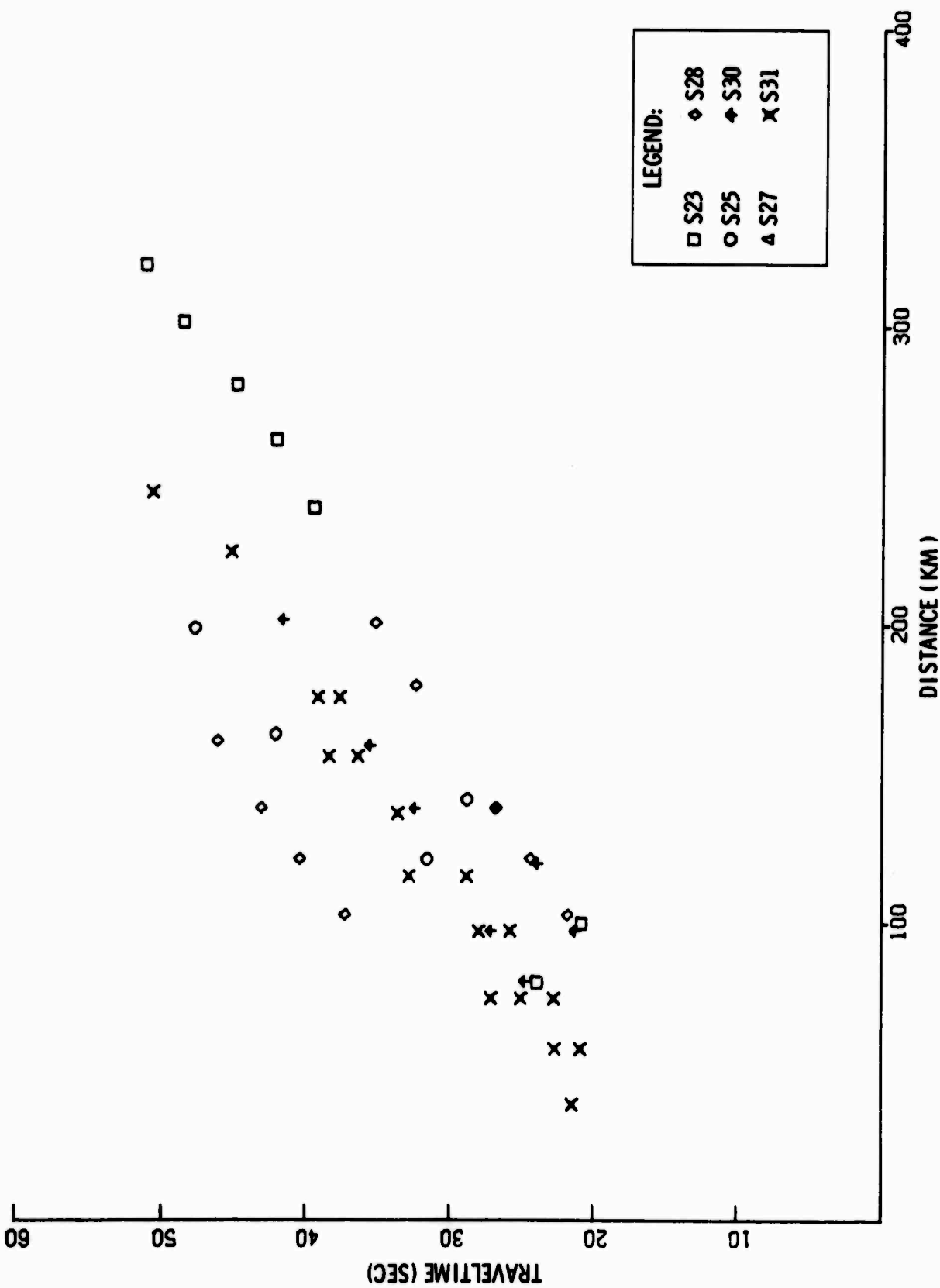


Figure II-25. Corrected Traveltimes of Phase III Secondary Arrivals

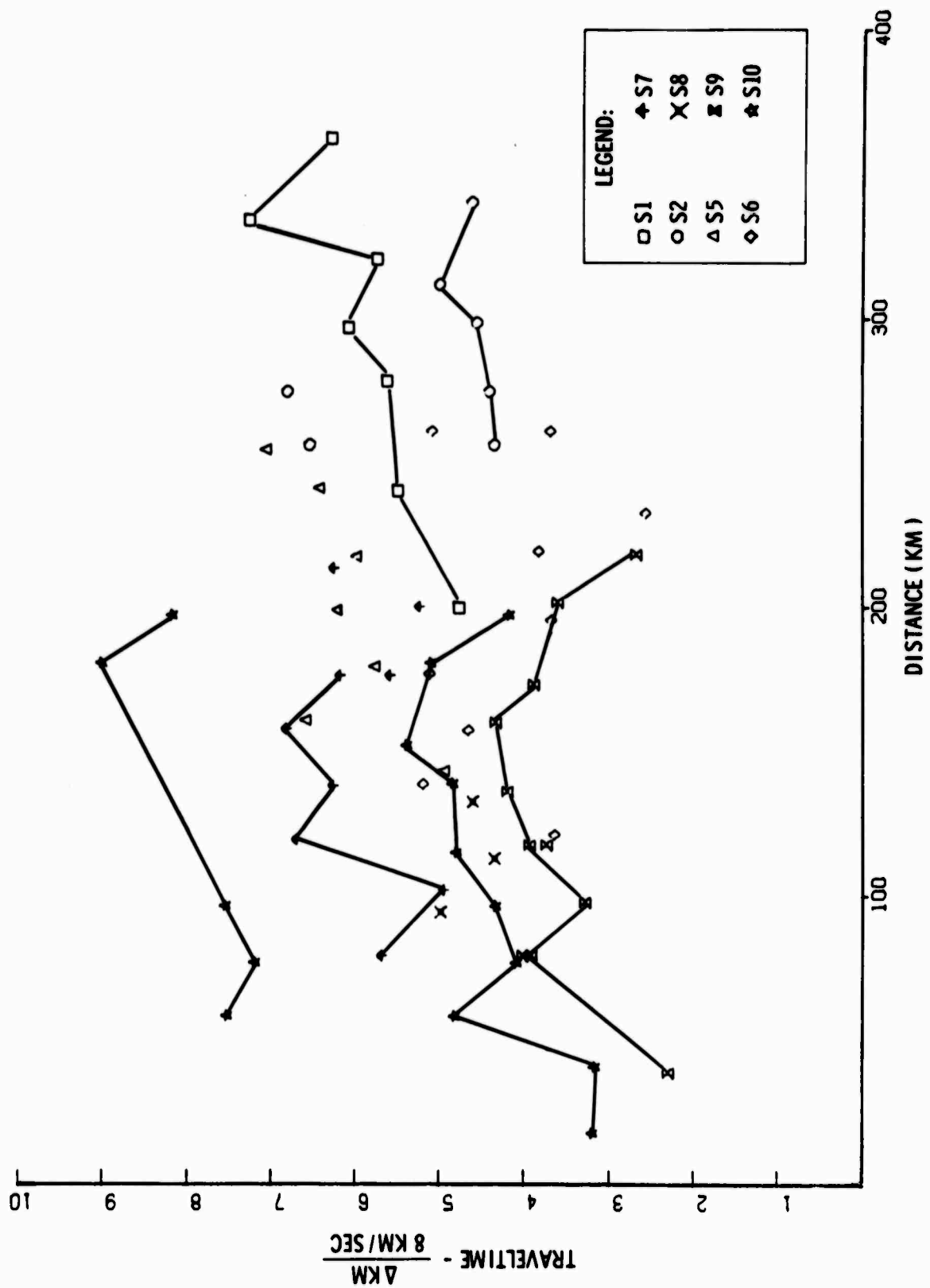


Figure II-26. Reduced Traveltimes of Phase I Secondary Arrivals for All Shots Recorded at Each Station

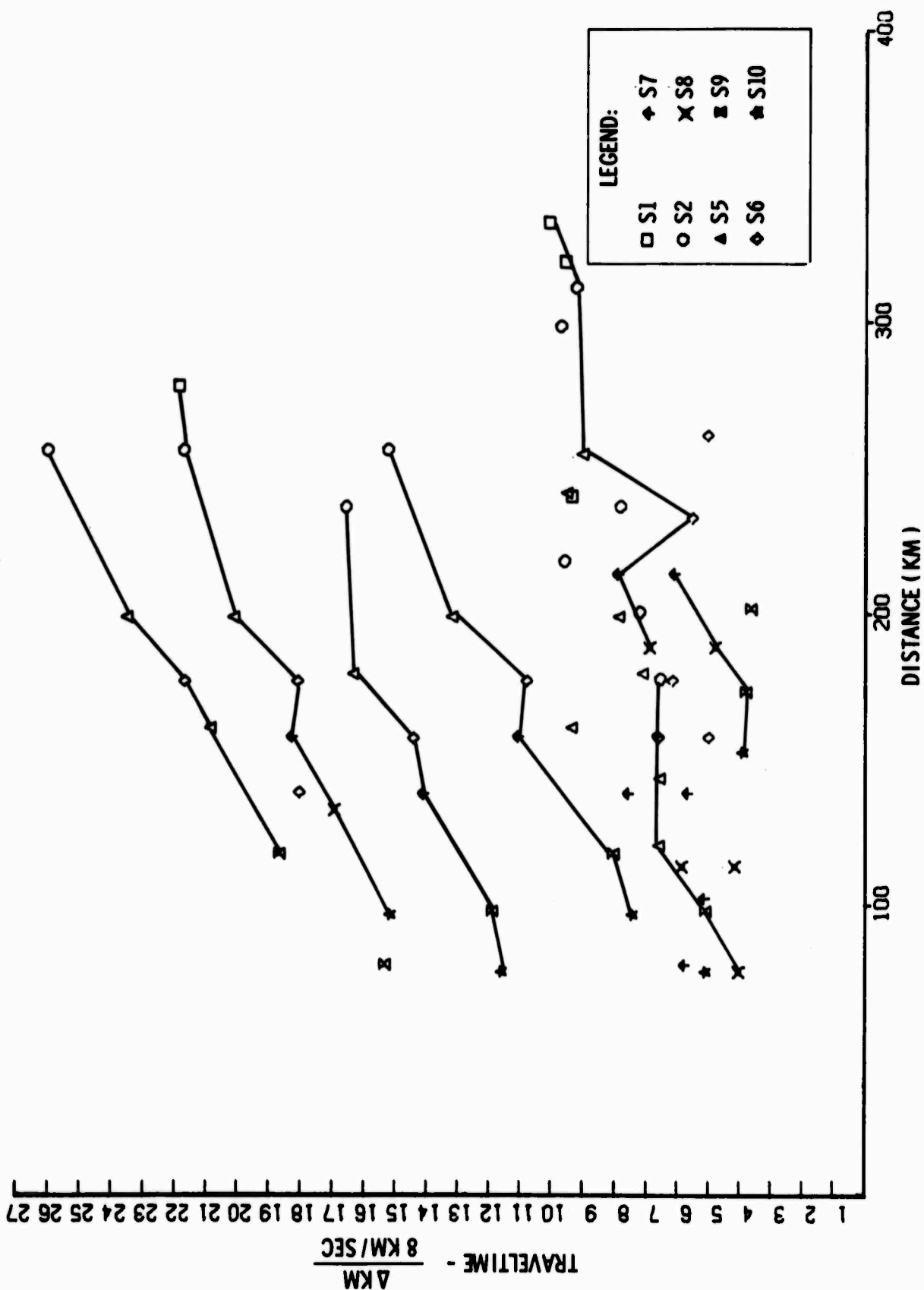


Figure II-27. Reduced Traveltimes of Phase I Secondary Arrivals for Each Shot Recorded at All Stations

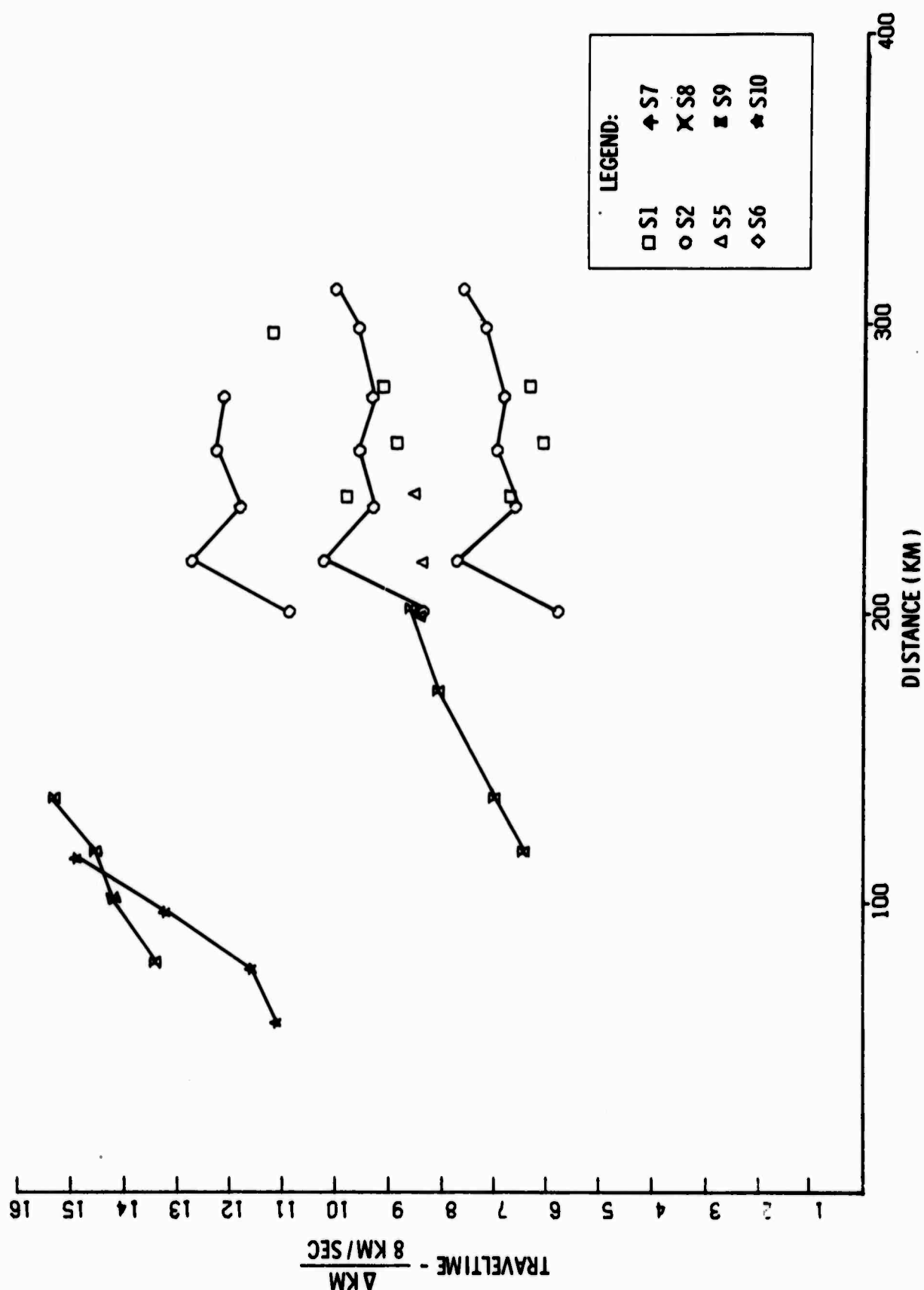


Figure II-28. Reduced Traveltimes of Phase I Secondary Arrivals,
Horizontal Instruments

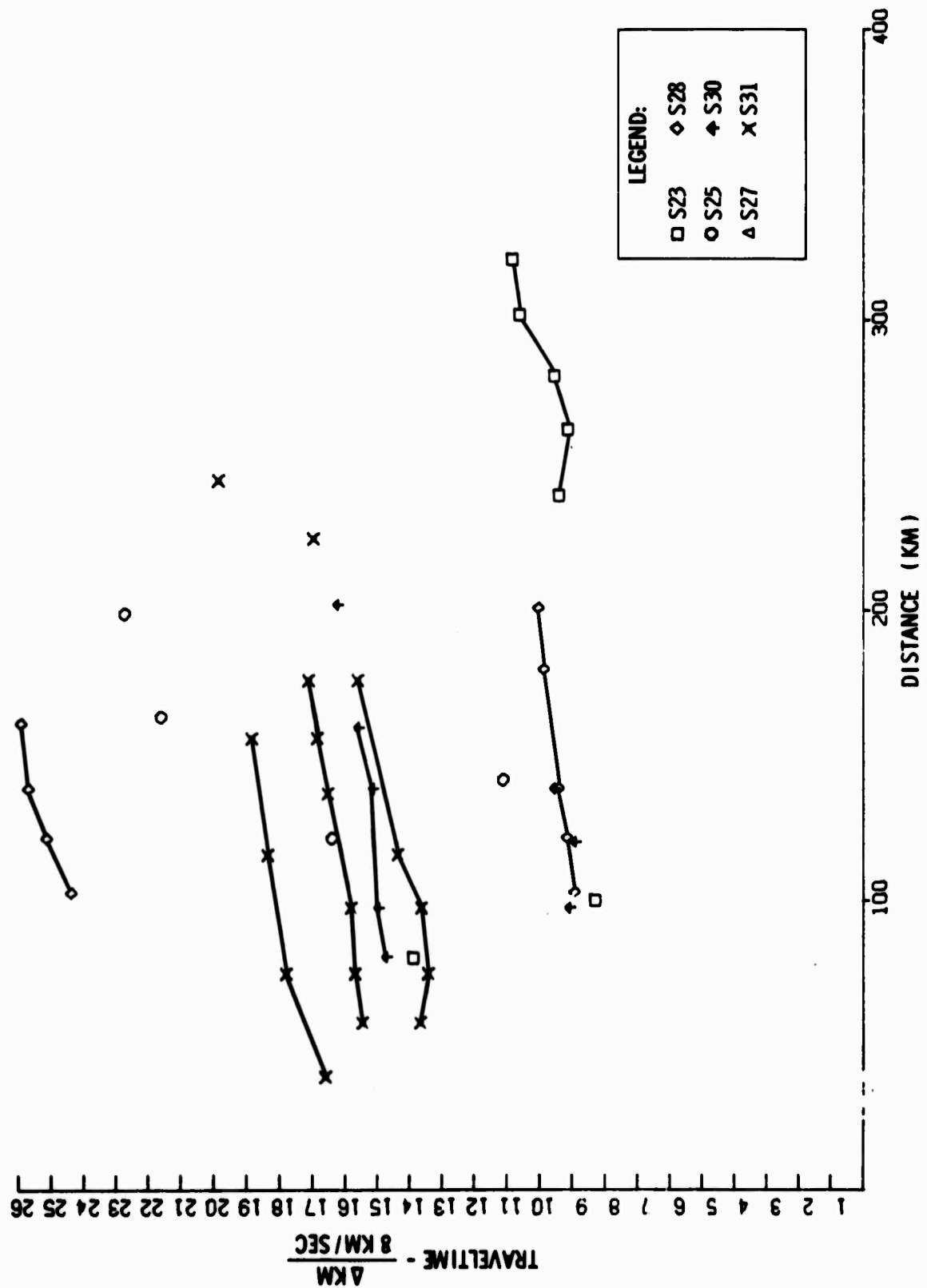


Figure II-29. Reduced Traveltimes of Phase III Secondary Arrivals



3. Deconvolution

In general, the shot recordings exhibit a reverberatory characteristic which is fairly typical of data recorded in an ocean environment. This effect is due to the water layering and tends to lengthen the refraction arrivals, making it difficult to detect separate refractions. This problem can be overcome theoretically by designing deconvolution filters which contract the arrival's duration by broadening its frequency band.

Deconvolution filters were designed and applied to records comprising all shots recorded at one station on the vertical and pressure channels. The stations used were S1, S7, S10, S23, and S31. Figures II-30 through II-34 show the input records, gate lengths used to compute the autocorrelation functions (and subsequent deconvolution filters), and the deconvolved records.

Deconvolution applied to station S31 is shown in Figure II-30. The top record shows the Phase-III north shots aligned at a velocity of 8.0 km/sec. The middle record shows deconvolution results using filters designed from each trace over the first gate, and the bottom record shows results from filters designed over the second gate. Broadening of the signal's frequency content by the process is apparent. Water depth at the station (1.5 km) and at the shots (3.7 km) indicates a 2-way traveltime in the water layer of about 2 sec for the station and 5 sec for the shots. The filter lengths of about 0.5 sec were not expected to eliminate the bounces associated with the large water depths at most recording stations and shot locations.



Figure II-31 shows deconvolution results using two gates for station S23. The water depth at this station was about 0.8 km, indicating a 2-way traveltime in the water of just over 1 sec. The traces have been whitened (including the noise preceding the signal), but little or no improvement in phase identification has been achieved.

Deconvolution results for station S1 are shown in Figure II-32. Water depth at this station was relatively shallow (0.34 km), and the noise level was high. Whitening of the traces was apparent; however, little improvement in the capability to identify masked secondaries was achieved.

Deconvolution results for stations S7 and S10 are shown in Figures II-33 and II-34. These show the water bounce in deep water quite clearly. In addition to using the two short gates, shown in (b) and (c), a long gate (17.6 sec) was used to design a longer deconvolution filter (1.73 sec). The result is shown in (d) where the traces have been shifted to vertically align the initial P-wave. Water depth at S7 is 7.02 km and is 4.92 km at S10, giving a 2-way traveltime in the water of 9.3 and 6.6 sec, respectively. No water-bounce arrivals are possible in the 5- or 6-sec interval following the initial P-wave; therefore, clear secondary arrivals would be expected in that interval. Fragmentary lineups are noted; however, they cannot be confidently picked across the records either before or after deconvolution.

The deconvolution technique generally does not appear to improve the capability to pick secondary arrivals, suggesting that secondary arrivals were usually weak. This observation again stresses the need to design shot and seismometer arrays which allow the use of first-arrival data to map all refractors.

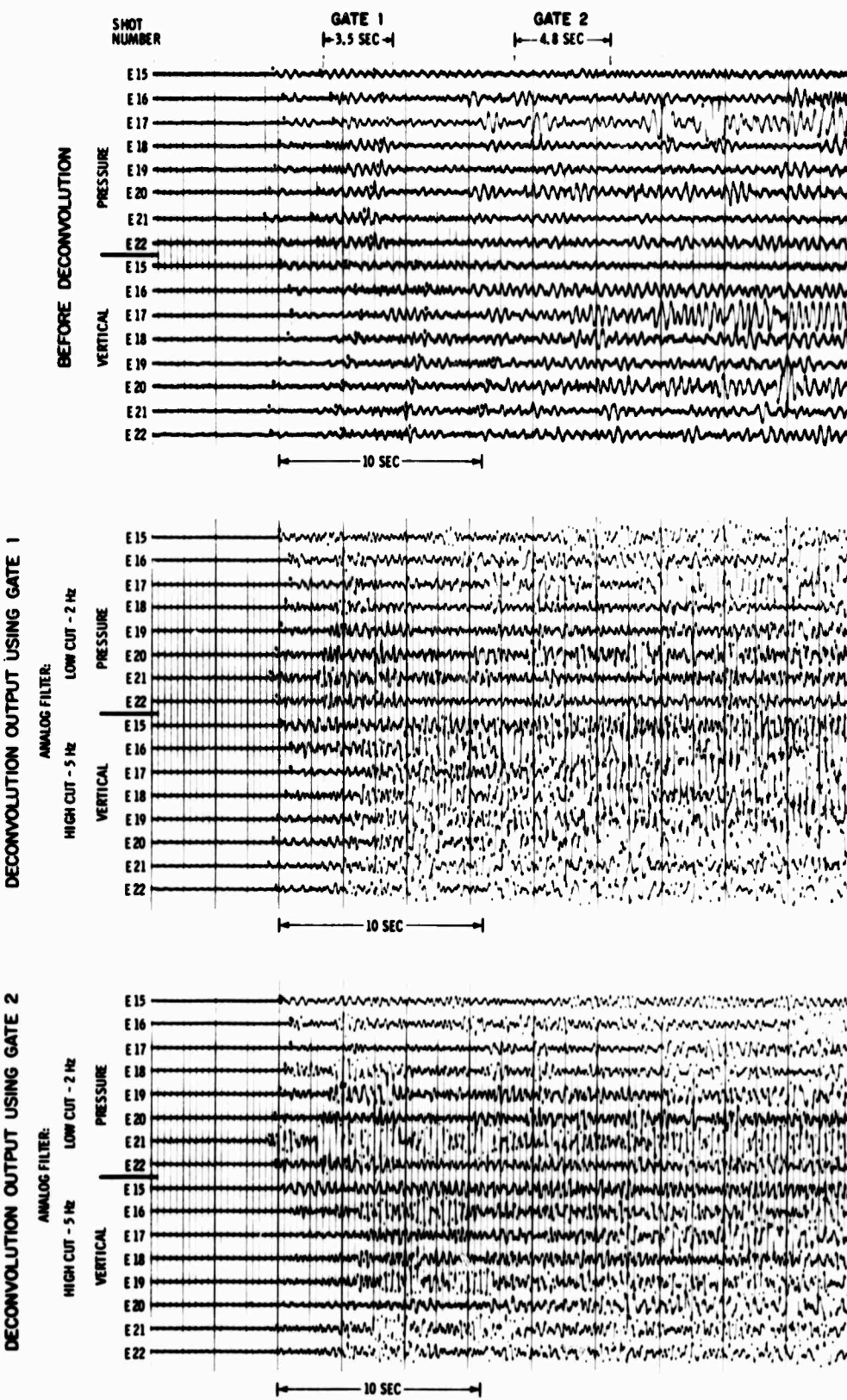


Figure II-30. Deconvolution, Station S31

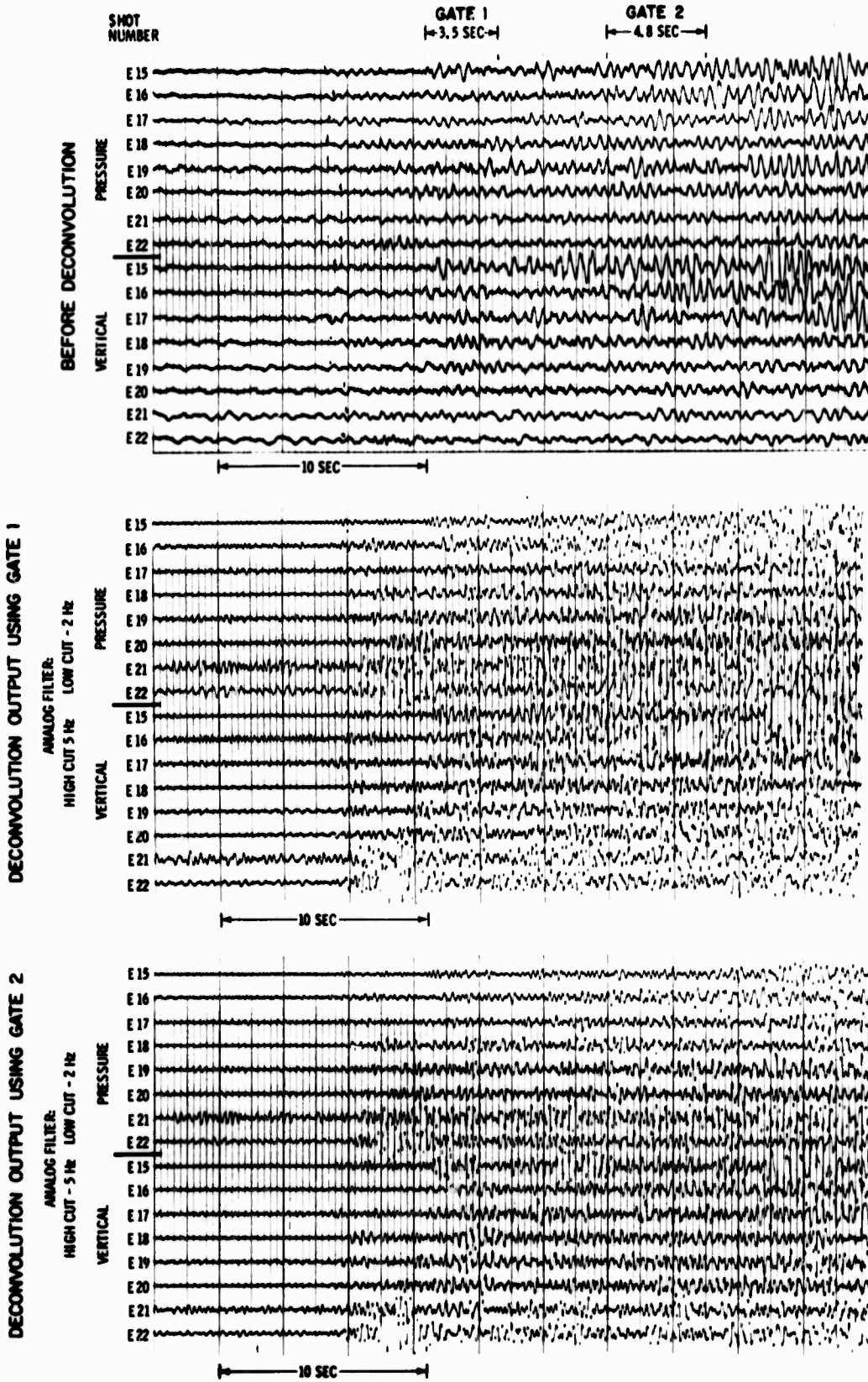


Figure II-31. Deconvolution, Station S23

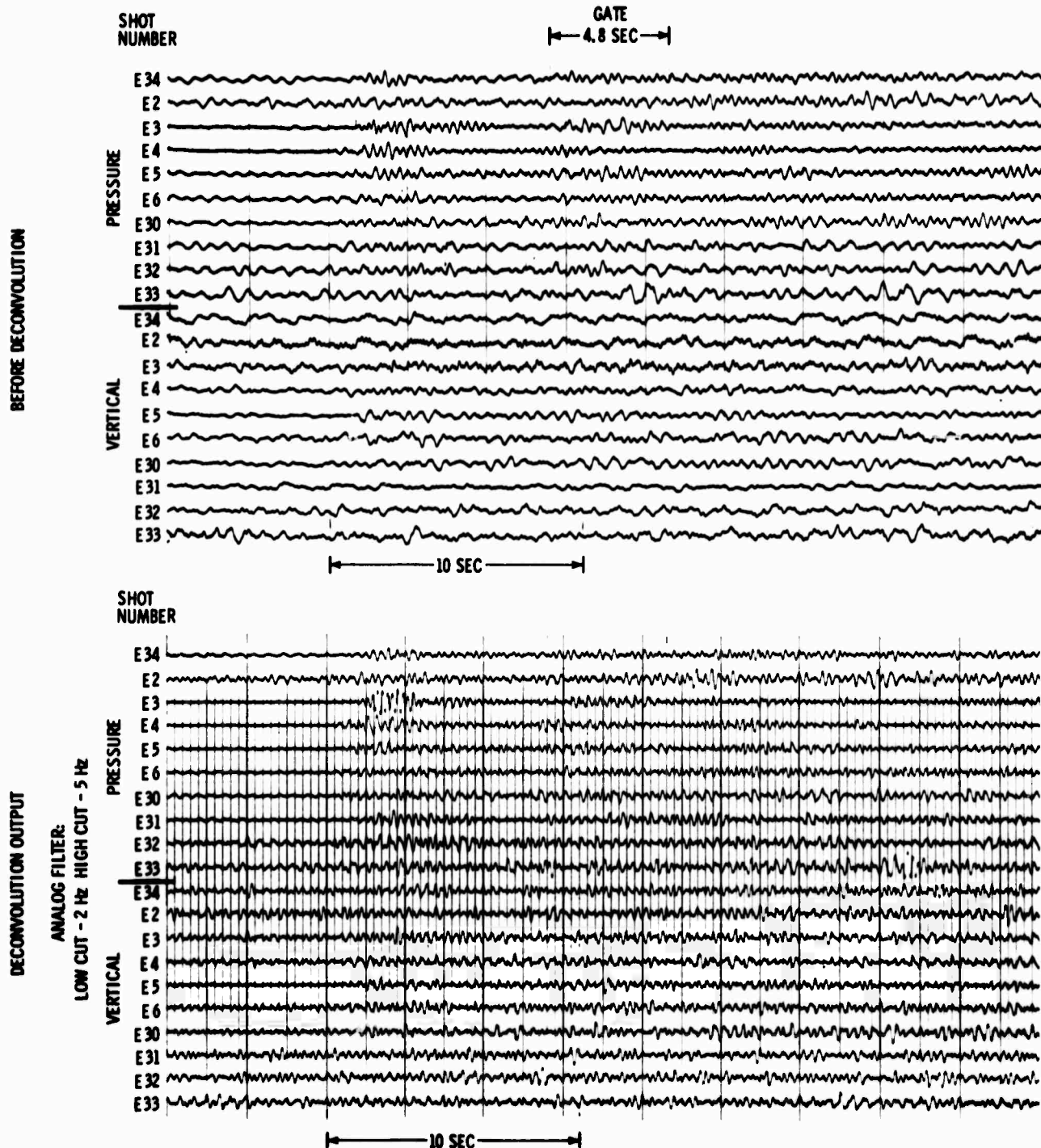
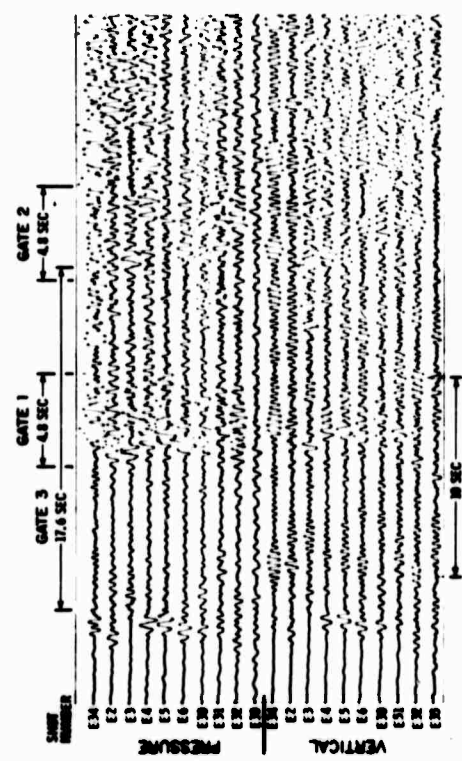


Figure II-32. Deconvolution, Station S1

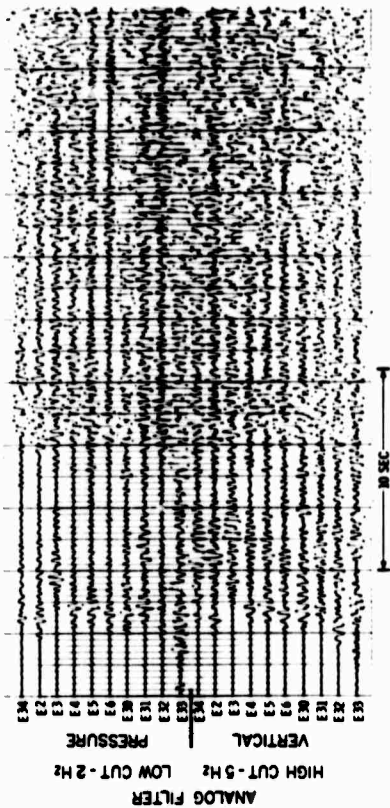


BEFORE DECONVOLUTION



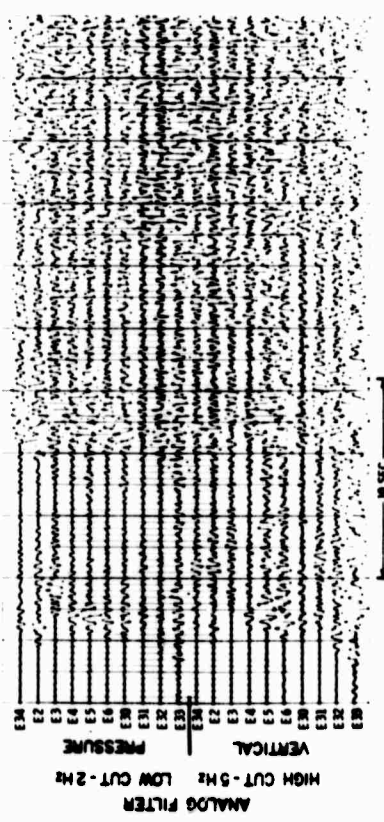
(a)

DECONVOLUTION OUTPUT USING GATE 1



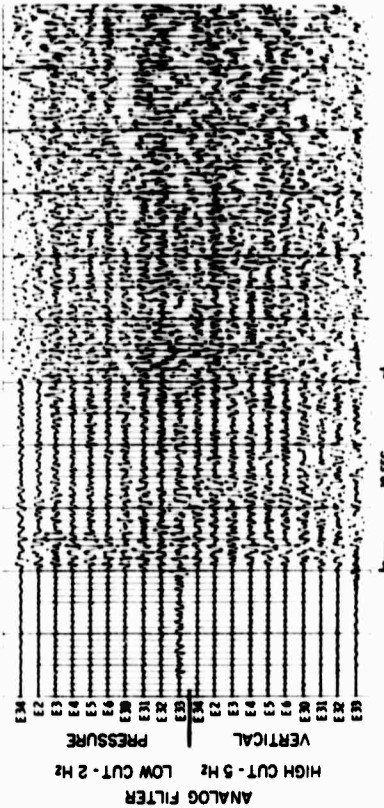
(b)

DECONVOLUTION OUTPUT USING GATE 2



(c)

DECONVOLUTION OUTPUT USING GATE 3



(d)

Figure II-33. Deconvolution, Station S7

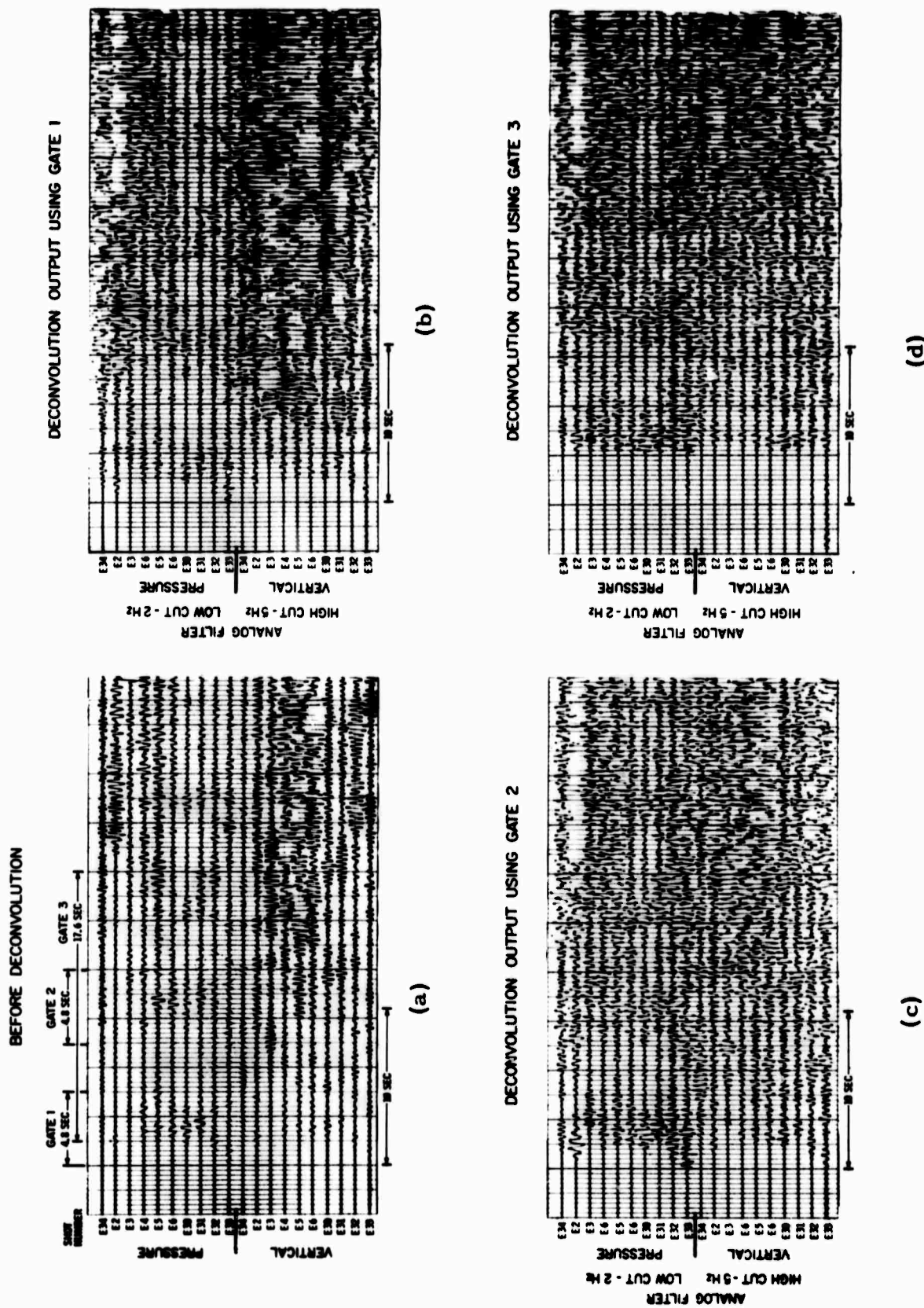


Figure II-34. Deconvolution, Station S10



B. REFRACTION ANALYSIS

The refraction analysis was fully described in the Preliminary Analysis Report.³ A brief description of that analysis and results are presented here for comparison with other methods.

The appendix gives the statistical confidence levels for the parameters of the refraction crustal model.

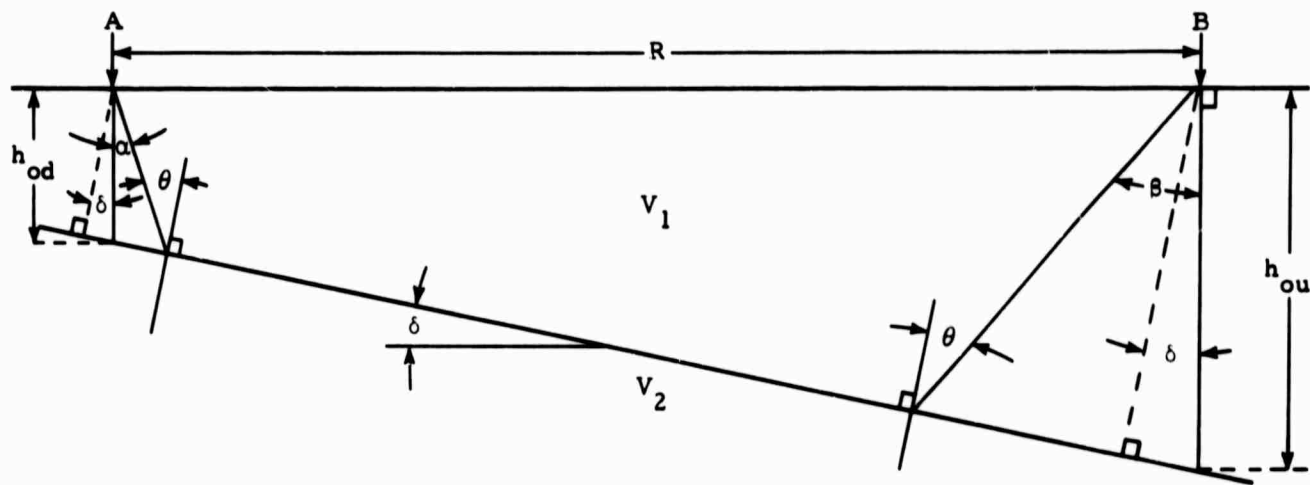
1. Iterations

Traveltimes of each first arrival were determined and input to a series of computer programs which reduced the data using standard refraction-analysis methods. The first program corrected the data to a reference plane; this correction was necessary because of the large lateral velocity variations in the uppermost 4 to 5 km below sea level because of large changes in water depth and structural environment. The reference plane was chosen to approximate the water bottom on either side of the Aleutian Ridge. Traveltime plots of the raw, corrected, and reduced times were generated by the second program. The third calculated least-square straight-line fits to the data. The final program resolved reverse-profile information to obtain the velocity, dip, and depth of the refractors.

The data analysis was iterative in nature. Using information from literature, the arrival-time data were reduced and crustal parameters estimated. The data were then recycled using the output of the previous iteration and were cycled through the computer programs three times.

2. Refraction Model

Model computation assumes plane constant-velocity dipping layers. Reverse-profile solutions were obtained from the equations given in Figure II-35. Dips and depths of the refractors were computed from measured apparent velocities and intercept times using the output of the final iteration. Line fits and points used are shown in Figure II-36 through II-39.



$$\sin \alpha = \frac{v_1}{v_{2u}}$$

$$\sin \beta = \frac{v_1}{v_{2d}}$$

$$\theta = \frac{\alpha + \beta}{2}$$

$$v_2 = \frac{v_1}{\sin \theta}$$

$$\delta = \frac{\beta - \alpha}{2}$$

$$h_{od} = \frac{v_1 t_{od}}{2 \cos \theta \cos \delta}$$

$$h_{ou} = \frac{v_1 t_{ou}}{2 \cos \theta \cos \delta}$$

where

R = horizontal distance between A and B

v_1 = velocity in layer 1

v_2 = velocity in layer 2

θ = critical angle defined by $\sin \theta = v_1/v_2$

v_{2d} = apparent velocity in the A-to-B direction for waves traveling in layer 2

v_{2u} = apparent velocity in the B-to-A direction for waves traveling in layer 2

t_{od} = zero-distance intercept time at A

t_{ou} = zero-distance intercept time at B

δ = dip of the interface in degrees

h_{od} = vertical depth to the interface at A

h_{ou} = vertical depth to the interface at B

Figure II-35. Equations for Solving Reverse Profile

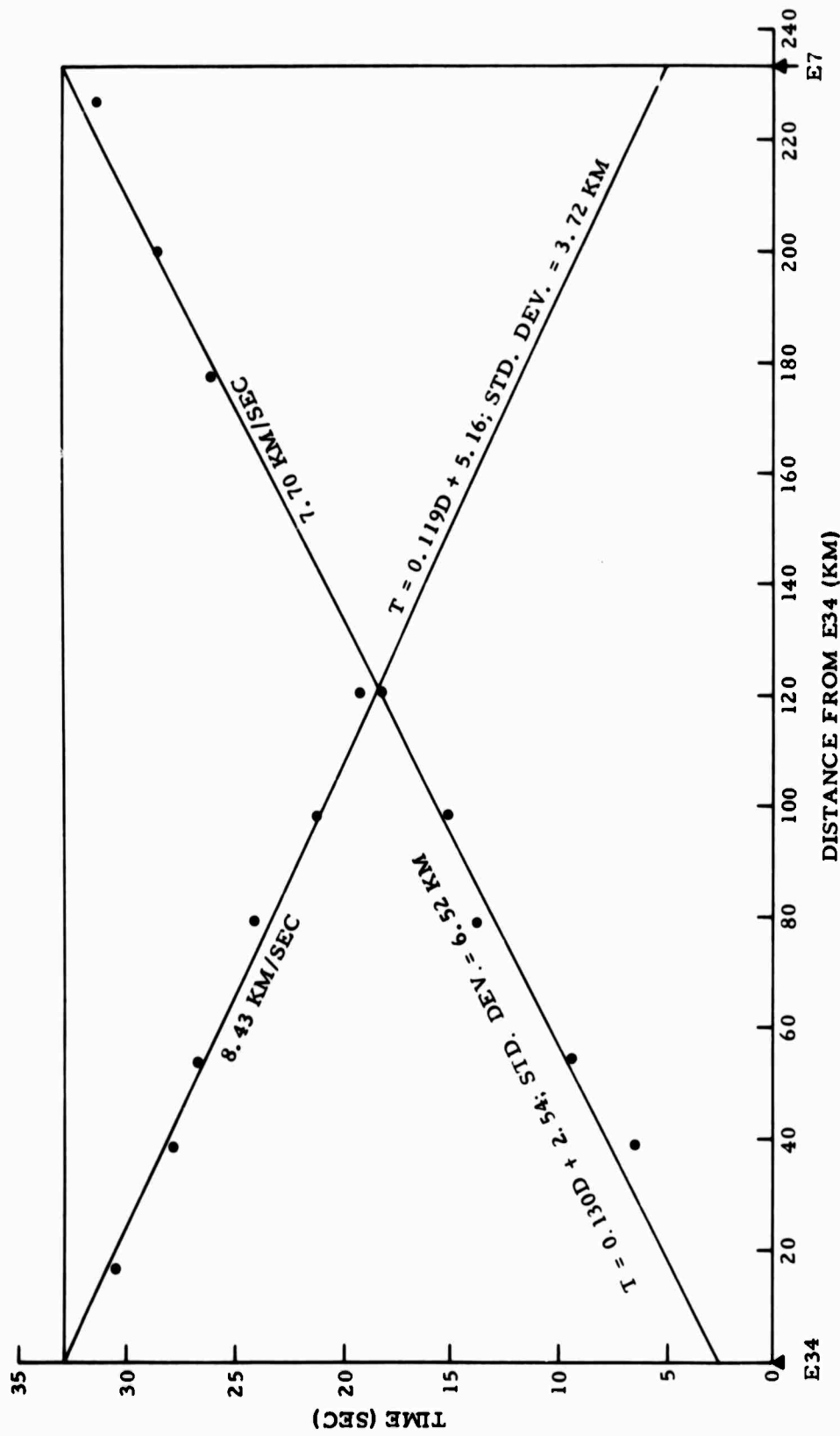


Figure II-36. Fitted Reverse Profile Between E34 and E7, Phase I

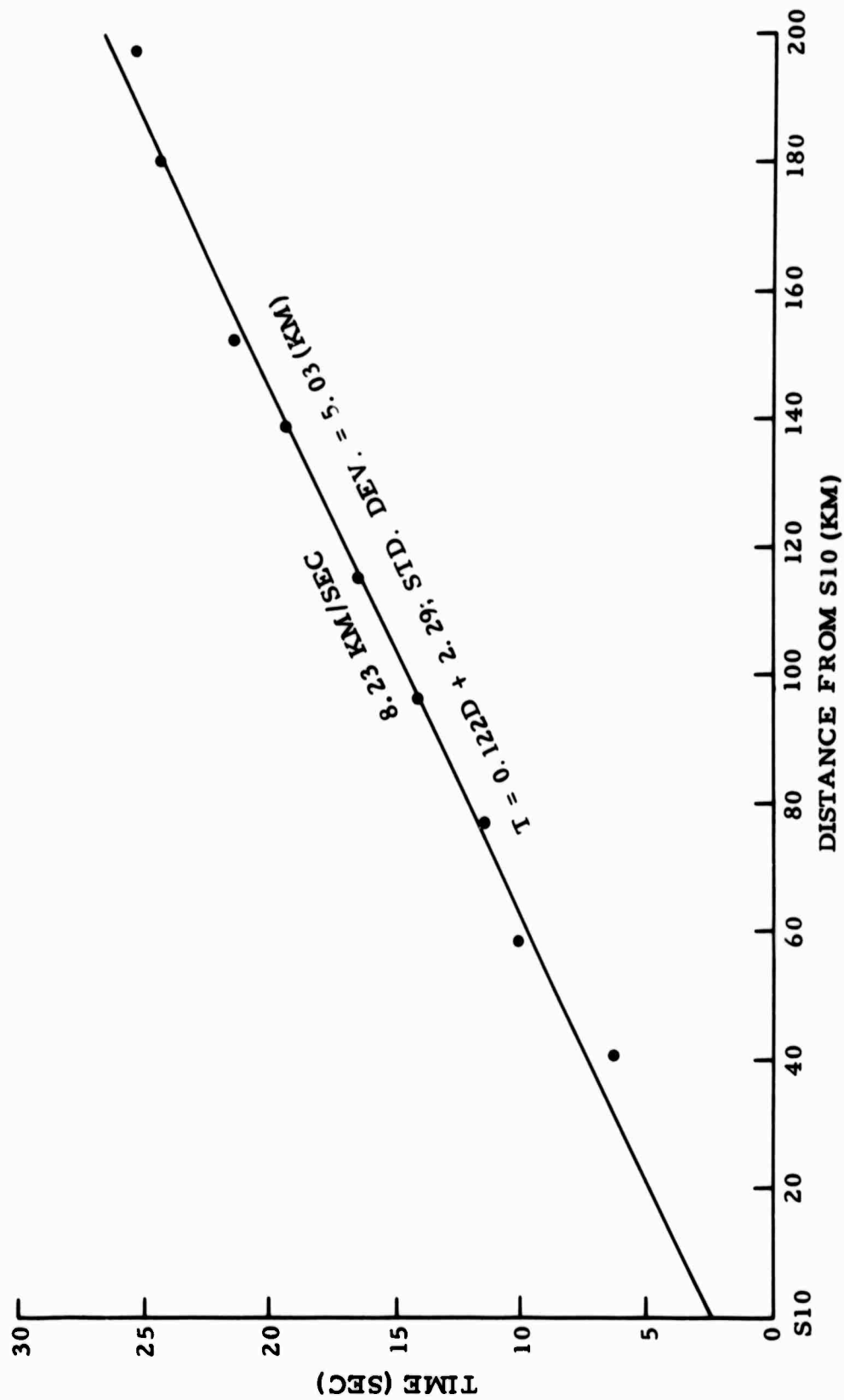


Figure II-37. Fitted Single Profile of Phase I Shots Recorded at S10

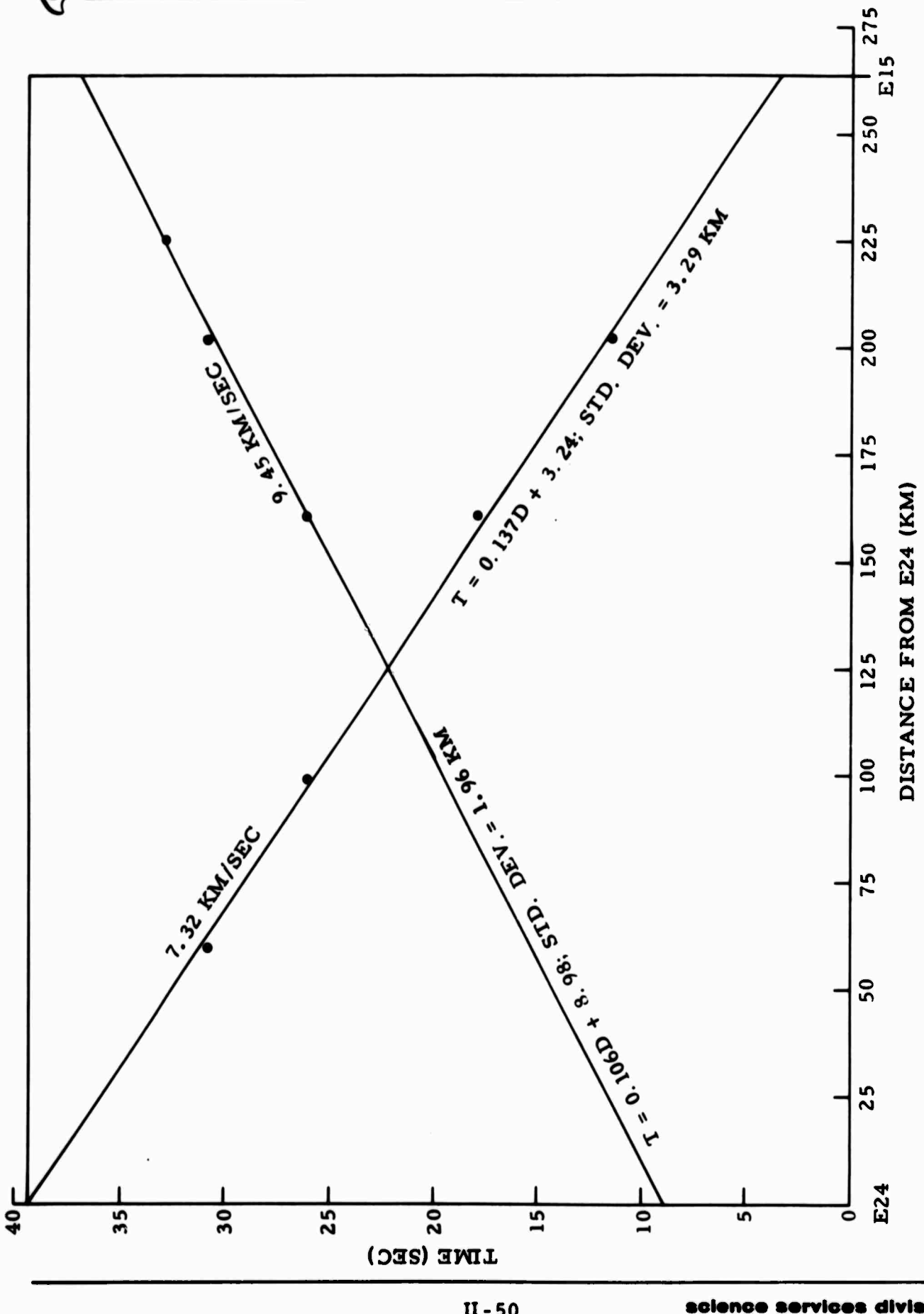


Figure II-38. Fitted Reverse Profile Between E24 and E15, Phase III

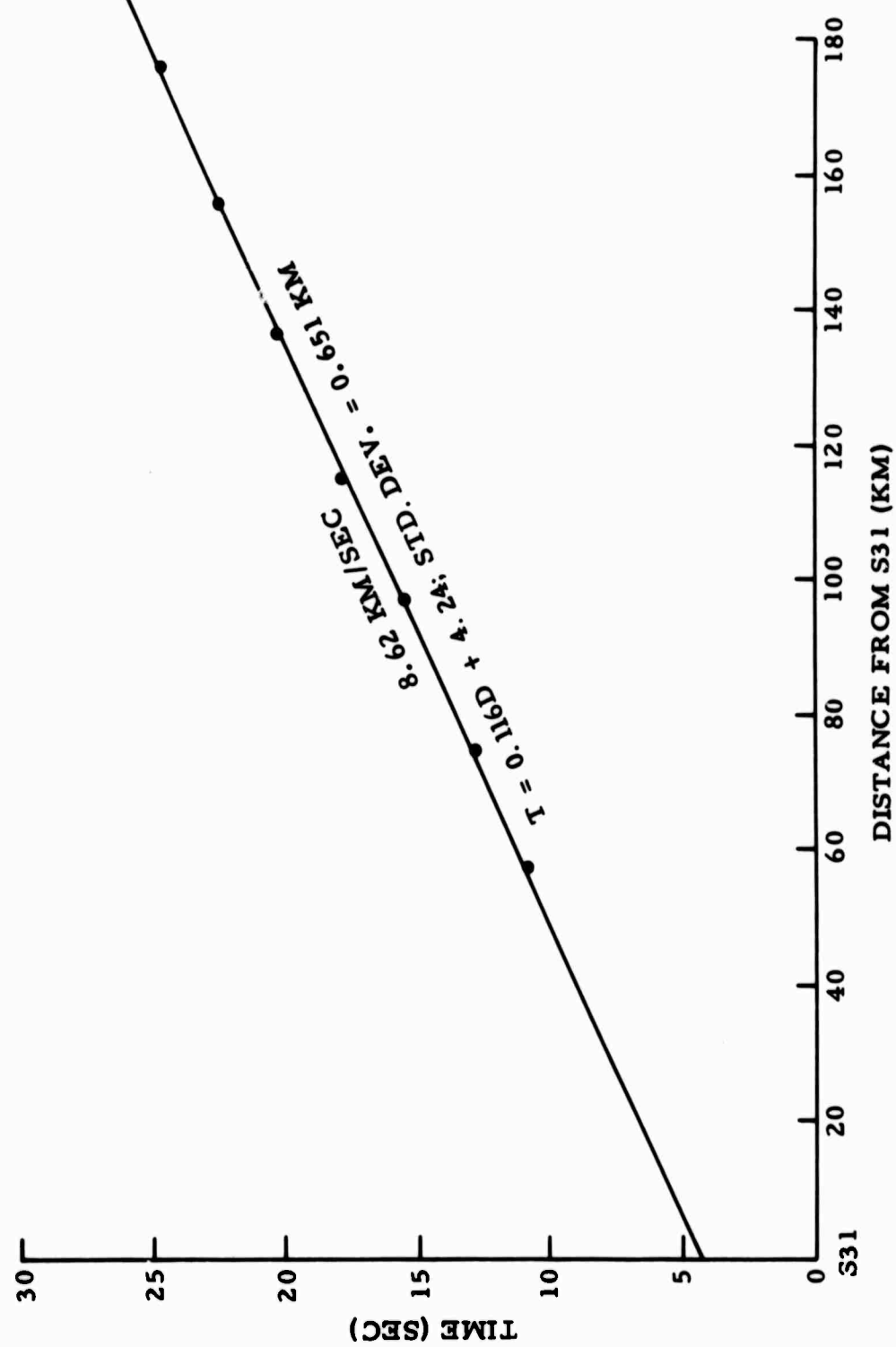
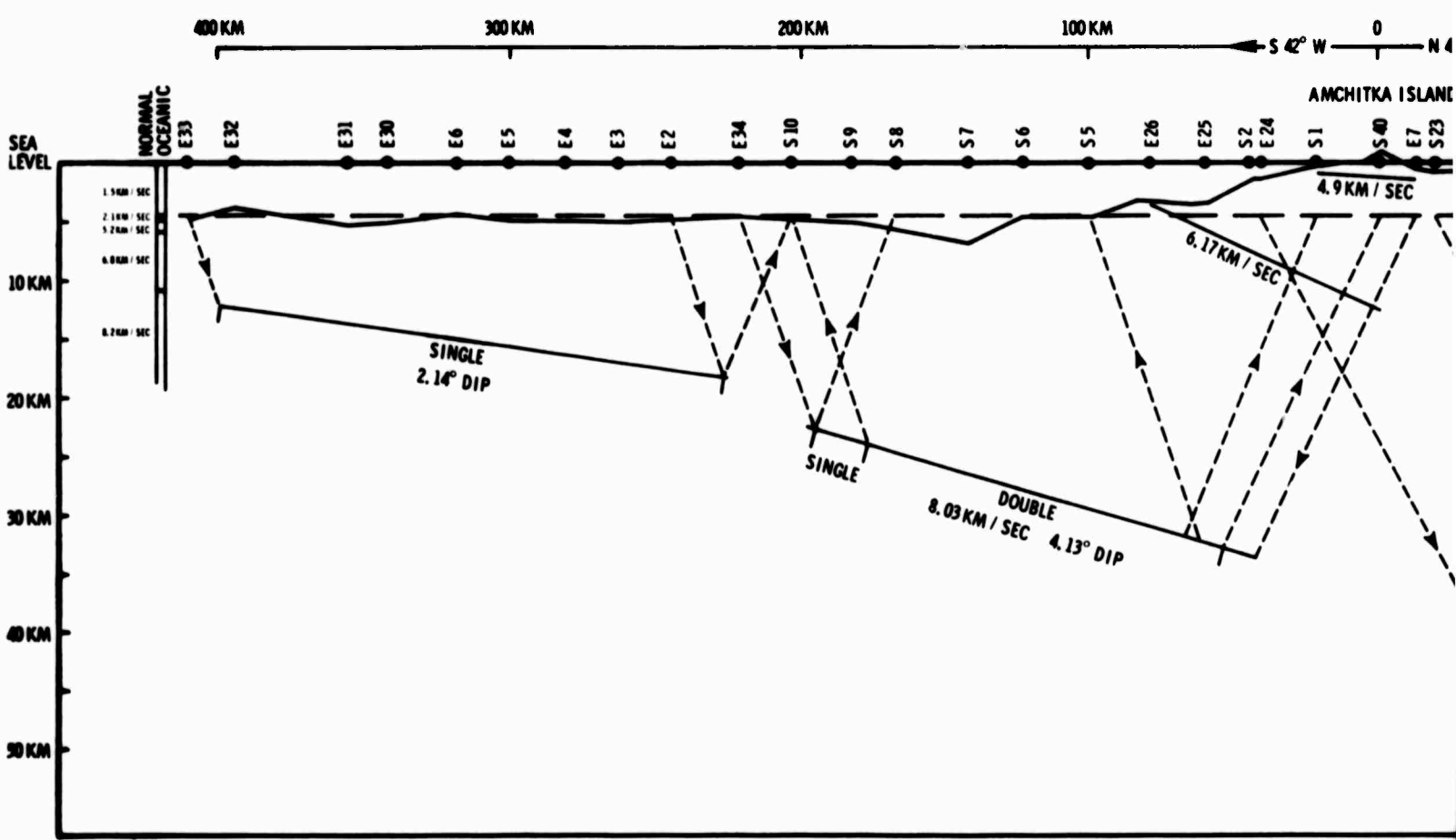


Figure II-39. Fitted Single Profile of Phase III Shots Recorded at S31



A

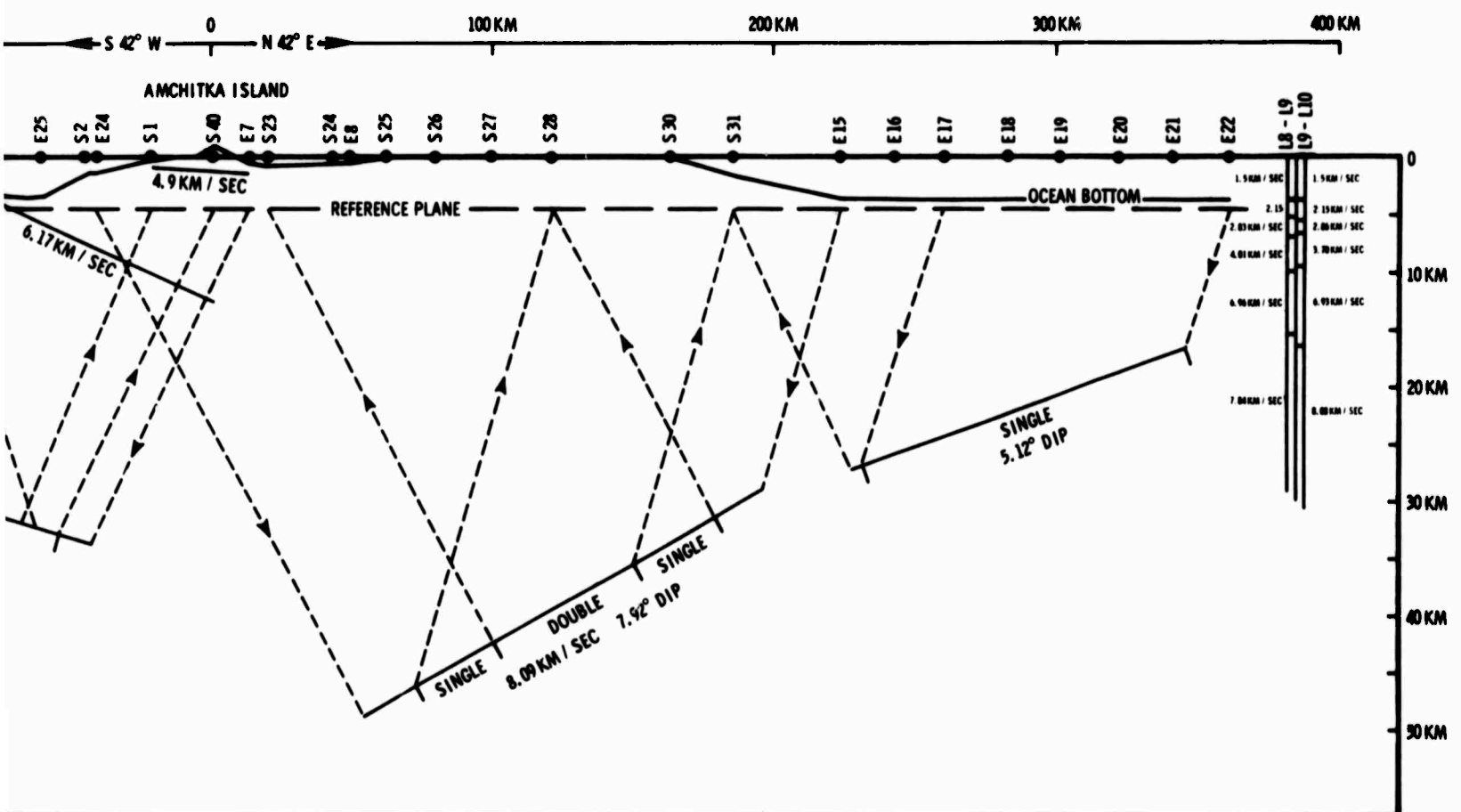


Figure II-40. Refraction Model Based on First Arrivals
(X4 vertical exaggeration)

BLANK PAGE



The refraction model is shown in Figure II-40. Areas of single (1-way) coverage and double (reverse) coverage are indicated on the figure. The resolved Moho velocity was 8.03 km/sec under the Phase I array and 8.09 km/sec under the Phase III array. A reverse-time mistie of the Phase III reverse profile indicated that the segment under the Phase III array could not be represented accurately by a single plane-dipping layer. The 1-way coverage under the two shot arrays was resolved by assuming that the Moho refractor velocity was the same as that determined under the stations for Phases I and III, respectively. Moho depth at the northern end of the Petrel Bank was about 15 km, which agrees with Shor's results for the Aleutian Basin.^{5,6} Near Amchitka, the depth increases to over 40 km. At the southern end of the Phase I array, the Moho depth is about 12 km, which is consistent with normal oceanic structure. In addition, two Pg refractors having velocities of 4.9 and 6.2 km/sec and depths of about 1 and 10 km were identified on the Aleutian Ridge.

C. WAVEFRONT ANALYSIS

1. Wavefront Methods

A wavefront is defined as the surface passing through the most advanced positions reached by a specific disturbance at any particular time. A "wavefront diagram" is therefore defined as a composite figure showing the intersections of the various wavefronts with a specified plane at successively equal time intervals.⁷ The entire construction of the wavefront diagram is based on Huygen's principle. Applying this principle in reverse, the wavefronts are traced backward from the receiver to the shot. Using this approach for two in-line explosions, one on each end of the line of receivers, wavefronts are determined for equal time intervals. The wavefronts from opposing explosions, with wavefront times adding to the reciprocal time (RT), intersect on or just below the refractor interface.



Plotting arrival times on a time-distance plot (Figure II-41) is the initial step in applying the wavefront method. By plotting the arrival times from two explosions at opposite ends recorded by several receivers in a line, a reverse time can be determined. Equal traveltimes over the whole spread, from one shotpoint to the other, are necessary for the method to produce a reliable model; i. e., the reverse traveltimes must agree. Reliability of the reverse-time data determines the reliability of the path interpretation and the refractor velocity determinations.

After the time-distance curves are plotted, x-positions corresponding to regular increments of arrival time at some convenient Δt are marked off on the curves. The x-positions are then transferred to the surface line of the receivers. The reversed curve is marked off in similar increments of time; however, these are at values of reverse time minus the integral time values. From this point, different variations of the wavefront method may be applied. The two methods used were the general wavefront method⁸ and wavefront targeting.⁹

Using the general wavefront method, arcs of small circles of radii equal to $\Delta t \cdot V_1$, $2\Delta t \cdot V_1$, $3\Delta t \cdot V_1$, etc., were drawn from the surface position of the arriving wavefronts back toward the event. Tangents to these sets of wavelets represent the wavefront system emanating from one of the explosions. This same procedure was used to produce a wavefront system from the other explosion. Since the time values of one set of wavefronts are chosen at the regular increments of Δt and the other set of wavefronts have time values of reverse time minus $n \cdot \Delta t$, the wavefronts intersect at some depth so that the sum of the times of intersecting wavefronts represents a total time equal to the reverse time. This point of intersection is a point on the refractor. The horizontal diagonal formed by the intersection of consecutive wavefronts is proportional to the true velocity of the refractor. This velocity equals the measured length of this diagonal divided by the Δt used.

The second wavefront method used was wavefront targeting. This method permits the rapid construction of the refractor from reversed



data. The method consists of reproducing two complete complementary wave-front systems for a given refractor, including image portions below the refractor and imaginary portions above the surface. These systems, as in the general wavefront method, intersect on or slightly below the refractor. One wavefront is constructed by drawing arcs of circles with centers at positions of arrival time and with radii equal to the difference between the arrival time and the wavefront time multiplied by V_1 . The wavefront is formed by connecting the arcs by tangents to the arcs. The other wavefront, with time equal to $RT - t$ - time of the other wavefront, is constructed in a similar manner using arrival times from the other source as the centers for the arcs.

A wavefront target, concentric circles of radii equal to $\Delta t \cdot V_1$, $2\Delta t \cdot V_1$, $3\Delta t \cdot V_1$, etc., was drawn on a transparent plastic sheet. A small hole was punched in the center of the target to accommodate a sharp pencil point. If a circle is tangent to both wavefronts of the complementary system, the center of the circle should be another point on the refractor. The target was maneuvered so that each successive circle was tangent to both wavefronts, and the location of the center was marked each time. The series of points produced in this manner were spaced at intervals of Δt along the refracting interface. The measured length between each pair of successive points divided by Δt readily gives the refractor velocity for that interval.

2. Wavefront Model

Since the Aleutian Islands Experiment was shot with the receivers on the water bottom and the explosions effectively on the surface, the arrival times were corrected to a reference plane in order to have source and receiver on the same plane. The corrected arrival times were plotted as time (sec) vs distance (km), giving a time-distance plot (Figure II-41). Since there was no explosion located at either receiver location, the exact reverse time could not be measured. Therefore, to determine the reverse time, the line through the plotted points on the time-distance curve must be projected to the distance which locates the source; the corresponding time



represents the reverse time. Phase I data were used (Figure II-41). The reverse time for E34 to E7 equals 33 sec.

Data recorded at six locations (S5, S6, S7, S8, S9, and S10) were used. First arrivals from E7 to S1 and S2 were refracted by a shallow interface; therefore, S1 and S2 cannot be used, since only one refractor at a time can be mapped using these methods. The arrival time from E34 to S10 cannot be used because it was a reflection (or refraction from a shallow interface) and only refractions from the same interface can be used in this method. Although only a few arrival times from the same interface were available, the plotted points were connected, allowing points to be picked at a convenient Δt , say 1 sec; those points were spotted at their corresponding distances along the surface line. Thus, the number of times available were increased, giving better coverage.

After the times were transferred to the surface line (in this case, the reference plane), arcs were drawn with radii equal to $1 \text{ sec} \cdot V_1$, $2 \text{ sec} \cdot V_1$, $3 \text{ sec} \cdot V_1$, etc., where $V_1 = 6.4 \text{ km/sec}$. In places, arcs drawn from adjacent points overlapped, thus making drawing tangents to these arcs impossible. This problem occurs in the area of S8 and S9. In order to obtain a wavefront solution, the curve connecting the arrival times on the time-distance plot was smoothed, thereby adjusting the estimated arrival times and allowing arcs to be properly drawn.

By employing the general wavefront method, wavefronts from E7 with times of 16 sec, 17 sec, 18 sec, ..., 25 sec, 26 sec were used. These wavefronts intersected with wavefronts from E34 with times of 17 sec, 16 sec, 15 sec, ..., 8 sec, 7 sec to form points on the refractor. This procedure produced the model shown in Figure II-42 with a refractor velocity (V_2) equal to 7.88 km/sec.

This model slopes downward toward E7 with an average dip of 13° . The shallowest point was under S10 (13.5 km), and the deepest point was under S5 (34 km); all depths were measured from the 4.5-km reference



plane. The portion of the refractor determined by the intersection of wavefronts with times to the north of S5 is projected points and therefore was not necessarily reliable. This includes the last two segments on the north end of the refractor. The last three segments on the south end also were not necessarily reliable, since the wavefronts for arrival times of 27 sec, 28 sec, and 29 sec were based on only 1-way data. (Arrival times from E34 were not available in this area, so there were no wavefronts to intersect with those from E7). In order to get the points south of S9, a radius equal to Δt times the already determined refractor velocity drawn with the center at the extreme point on the refractor intersects with 1-way wavefronts from E7. In this manner, the refractor can be extended to S10. The model, therefore, is most reliable in the area between S8 and a point 10 km north of S6.

Using the wavefront targeting method, a wavefront system, which included a wavefront from E34 with a time of 12 sec and a wavefront with a time of 21 sec from E7, was developed. By maneuvering the wavefront target so that each successive circle was tangent to both complements of the system, the wavefront targeting model was produced (Figure II-43). This method gave a refractor velocity of 7.98 km/sec.

This model was very similar to that produced by the other method. The dip trend was in the same direction as that of the previous model; the average dip was 12° , which agrees with refractor dip determined by perturbation techniques over the same segment. The shallowest point (13.5 km) was 3.5 km south of S9, and the deepest point (29.5 km) was 7 km north of S6.

Both of the wavefront methods produce models of the refractor which are reliable; however, to achieve the best model possible, a more accurate method of measuring the reverse traveltime must be used. Ideally, there should be a receiver at each source location to directly record the entire traveltime from both directions. Also, there should be more receivers along the line to directly record more arrival times. These would give better coverage over the spread and thus give better reliability to the interpretation.

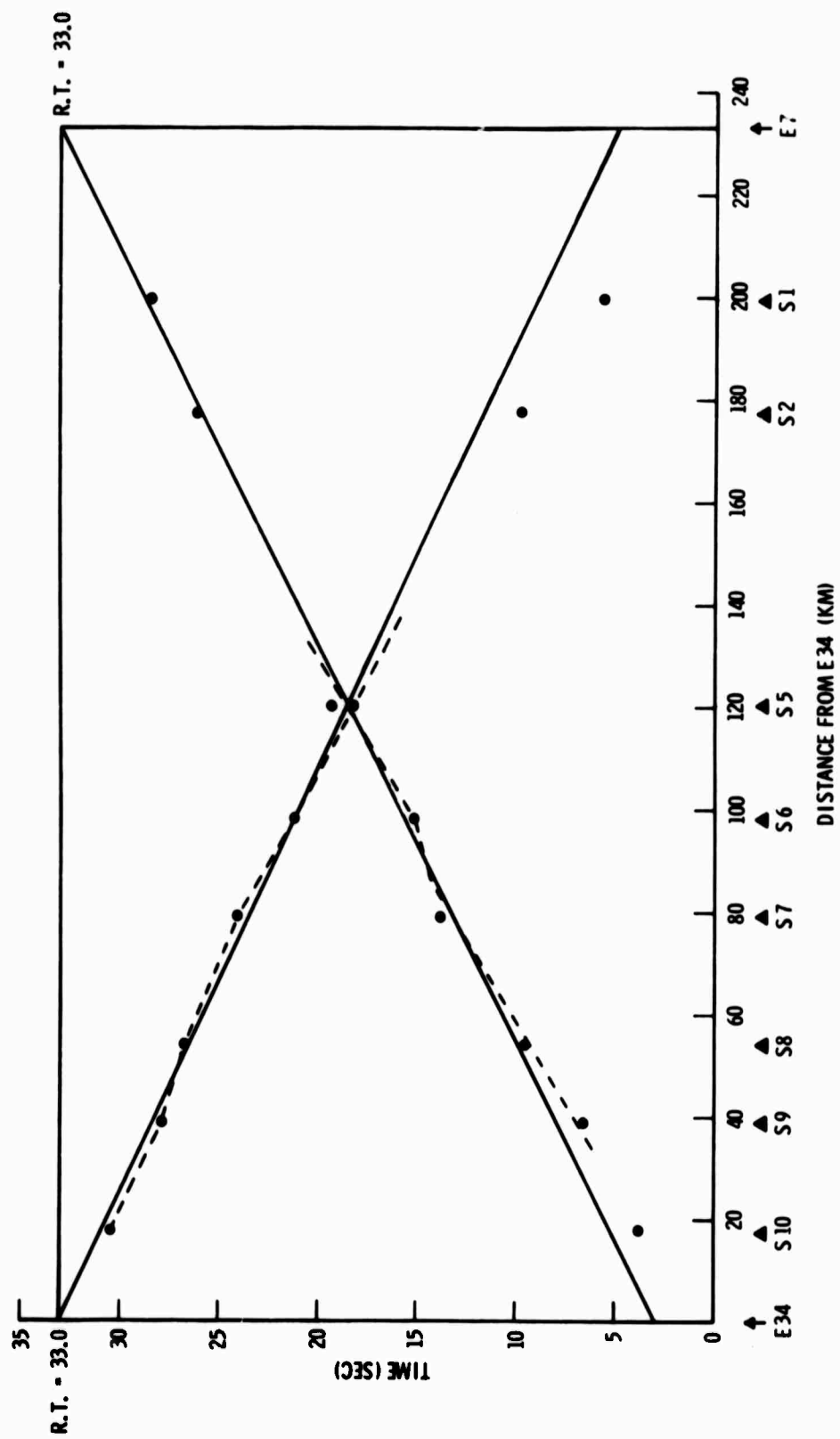


Figure II-41. Reverse Profile Plot Between E34 and E7, Phase I

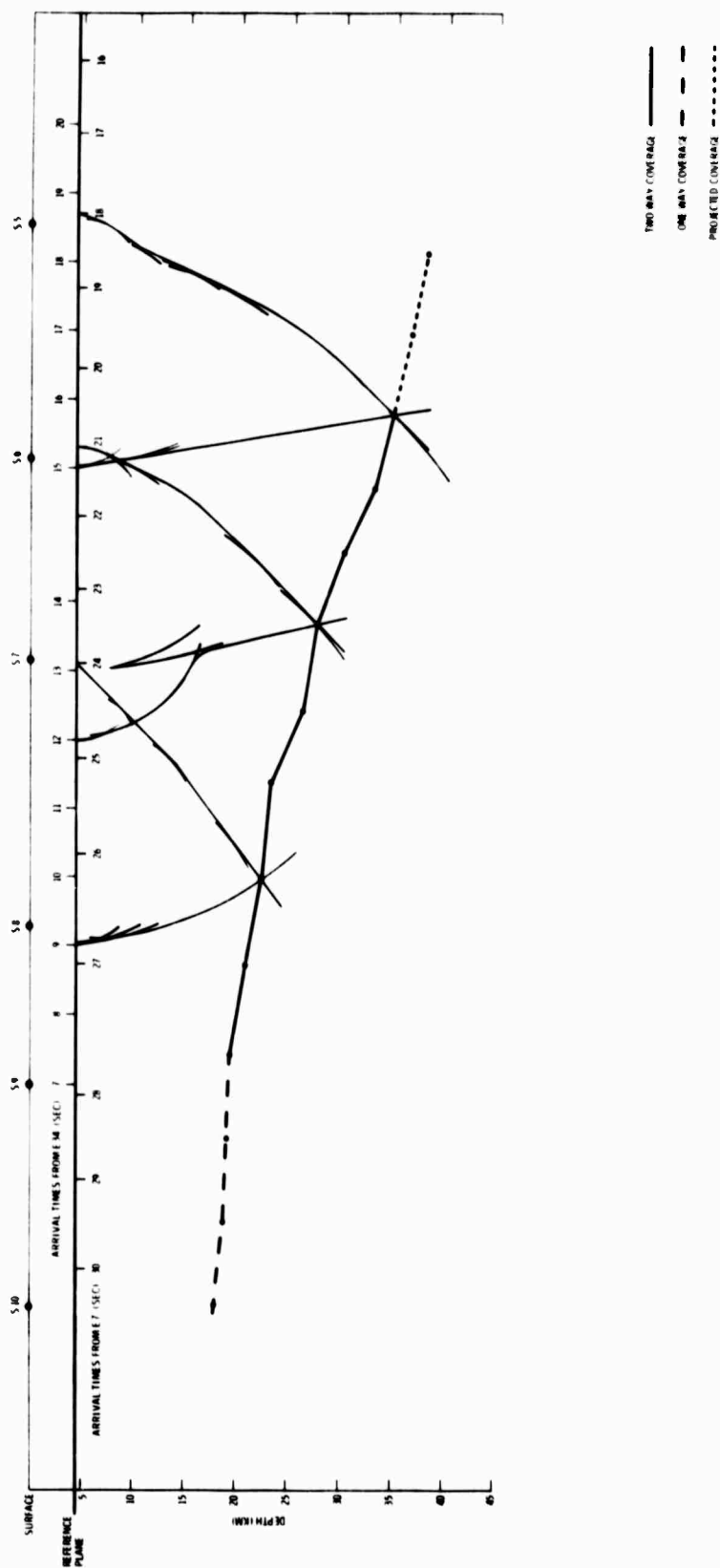


Figure II-42. Wavefront Model Using General Wavefront Method

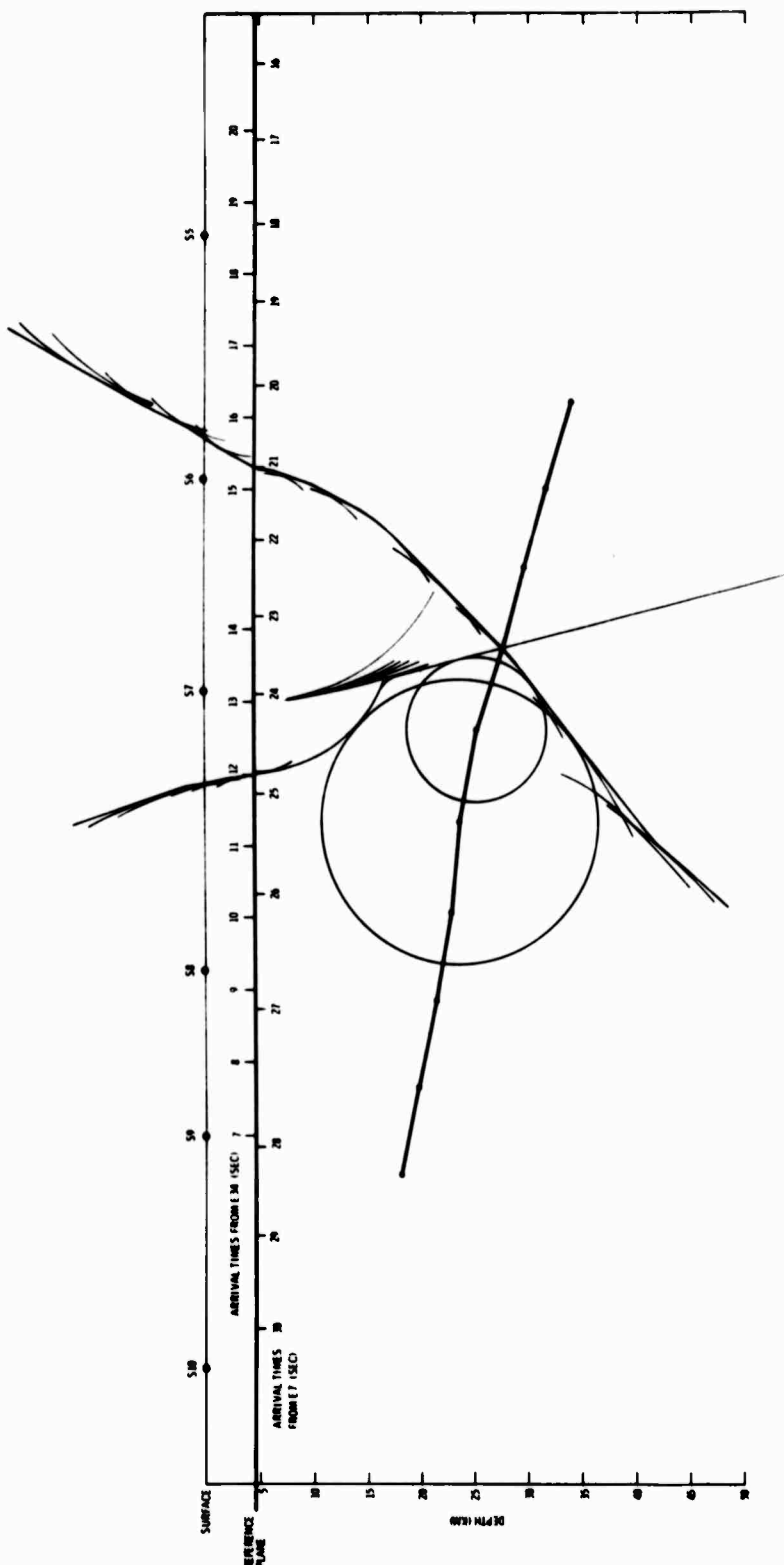


Figure II-43. Wavefront Targeting Method



D. TIME-TERM ANALYSIS

1. Time-Term Theory

The basic equation of the time-term method of seismic refraction analysis is derived from the geometry of a refraction model consisting of two layers separated by a plane interface. The solution of a system of such equations for experimental traveltimes data from a 2-layered structure yields a seismic velocity in the lower layer and the contour of the interface. The contour is given in terms of the depth to the interface beneath each shot and station of the experimental array.

In Figure II-44, Δ is the distance between shot A and station B; H_a and H_b are the perpendiculars from the refracting layer to A and B; θ is the angle of incidence of the critically refracted ray; ϕ is the dip angle of the refractor; V_1 and V_2 are the seismic velocities in the upper layer and refractor, respectively; and d_1 , d_2 , and d_3 are the three segments of the ray path from A to B. The traveltime t of the ray from A to B is

$$t = \frac{d_1}{V_1} + \frac{d_2}{V_2} + \frac{d_3}{V_1} \quad (2-1)$$

Also from Figure II-44,

$$d_1 = \frac{H_a}{\cos \theta} \quad (2-2)$$

$$d_2 = \Delta \cos \phi - d_1 \sin \theta - d_3 \sin \theta \quad (2-3)$$

$$d_3 = \frac{H_b}{\cos \theta} \quad (2-4)$$

Therefore,

$$t = \frac{H_a}{V_1 \cos \theta} + \frac{H_b}{V_1 \cos \theta} + \frac{\Delta \cos \phi}{V_2} - \frac{H_a \sin \theta}{V_2 \cos \theta} - \frac{H_b \sin \theta}{V_2 \cos \theta} \quad (2-5)$$

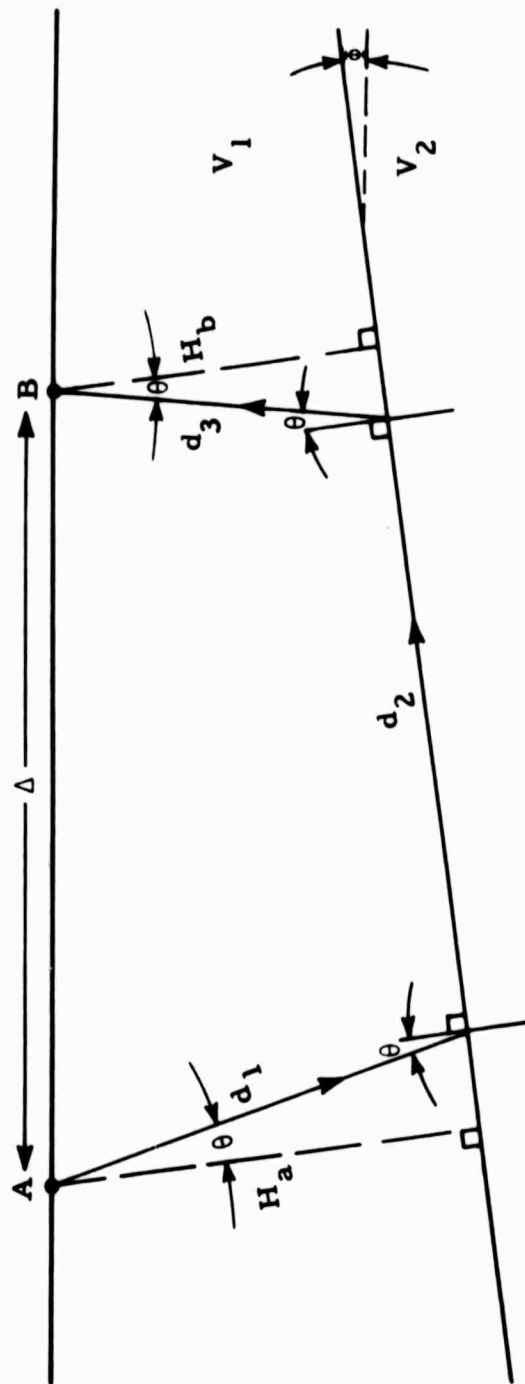


Figure II-44. Ray Path Diagram for Critically Refracted Rays



Applying the relation $V_1/V_2 = \sin \theta$ to Equation 2-5 yields

$$t = (H_a + H_b) \frac{\cos \theta}{V_1} + \frac{\Delta \cos \phi}{V_2} \quad (2-6)$$

It may be shown that for dip angles normally encountered, the error in $(H_a + H_b)$ which arises from setting $\cos \phi = 1$ in Equation 2-6 is negligibly small.¹⁰ Making this approximation in Equation 2-6 results in the time-term equation

$$t = p + q + \frac{\Delta}{V_2} \quad (2-7)$$

where

$$p = \frac{H_a \cos \theta}{V_1} = \frac{H_a \sqrt{V_2^2 - V_1^2}}{V_1 V_2} \quad (2-8a)$$

$$q = \frac{H_b \cos \theta}{V_1} = \frac{H_b \sqrt{V_2^2 - V_1^2}}{V_1 V_2} \quad (2-8b)$$

Therefore, in the time-term equation, the time-term p for a given shot and the time-term q for a given station are characteristic of the velocities V_1 and V_2 and the depth H of the refractor beneath the shot or station site.

The refractor velocity in Equation 2-7, previously considered constant, may be replaced with a refractor velocity which is a linear function of the distance Δ . Changes in $V_2 (\Delta)$ may be attributed to a velocity gradient in the refracting medium.¹¹ This velocity function may be written as

$$V_2(\Delta) = V_a + V_b \Delta \quad (2-9)$$



Substituting this function in Equation 2-7 yields

$$t = p + q + \frac{\Delta}{V_a + V_b \Delta} \quad (2-10)$$

Since it is desirable to have the time-term Equation 2-10 remain linear for ease of solution, the last term may be rewritten using the relation

$$\frac{1}{1+x} = 1 - x + x^2 - \dots \quad |x| < 1 \quad (2-11)$$

Therefore,

$$\frac{\Delta}{V_a + V_b \Delta} = \frac{\Delta}{V_a} \left(\frac{1}{1 + \left[\frac{V_b}{V_a} \right] \Delta} \right) = \frac{\Delta}{V_a} \left[1 - \frac{V_b}{V_a} \Delta + \left(\frac{V_b}{V_a} \Delta \right)^2 - \dots \right]$$

or

$$\frac{\Delta}{V_a + V_b} = \frac{1}{V_a} \Delta - \frac{V_b}{V_a^2} \Delta^2 + \frac{V_b^2}{V_a^3} \Delta^3 - \dots \quad (2-12)$$

It may be shown that for typical values of V_a , V_b , and Δ , the right side of Equation 2-12 may be approximated by its first two terms with negligibly small error.¹¹ Using this approximation and rearranging, Equation 2-10 becomes

$$p + q = t - k_1 \Delta - k_2 \Delta^2 \quad (2-13)$$

where

$$k_1 = \frac{1}{V_a} \quad (2-14a)$$

and

$$k_2 = -\frac{V_b}{V_a^2} \quad (2-14b)$$



In an array consisting of m shots and n stations, a maximum of $m \times n$ equations of the form of Equation 2-13 may be written. However, if no shot and station locations coincide, this system will not have a unique solution. As inspection of Equation 2-13 shows, an arbitrary constant α may be subtracted from each shot time-term and added to each station time-term without affecting the equation otherwise. To overcome this difficulty, one of the time-terms may be set equal to 0 arbitrarily and the constant α reintroduced after the system of equations has been solved.

The system of Equations 2-13 for an array of m shots and n stations may be represented in matrix form as

$$AB = T - k_1 D - k_2 E \quad (2-15)$$

The matrix B is a column matrix of $m + n - 1$ elements, the first m elements b_j ($j = 1, 2, \dots, m$) being the shot time-terms and the last $n - 1$ elements b_j ($j = m + 1, m + 2, \dots, m + n - 1$) being the station time-terms. The last station time-term b_{m+n} has been set equal to 0, as previously explained. The matrix A is a matrix of L rows and $m + n - 1$ columns, where $L \leq (m \times n)$ is the number of observations obtained from the array. Its elements a_{ij} are either 1's or 0's, depending on whether or not the i^{th} observation was either initiated or recorded at the j^{th} site. The matrix T is a column matrix of the L traveltimes observed; D is the corresponding matrix of the Δ for each observation; and E is the corresponding matrix of the squared Δ for each observation.

Multiplying Equation 2-15 on the left by A' (the transpose of A) yields

$$QB = P - k_1 R - k_2 S \quad (2-16)$$



where $Q = A'A$, $P = A'T$, $R = A'D$, and $S = A'E$. Multiplying on the left by Q^{-1} , the inverse of Q , yields

$$B = X - k_1 Y - k_2 Z \quad (2-17)$$

where $X = Q^{-1}P$, $Y = Q^{-1}R$, and $Z = Q^{-1}S$.

Equation 2-17 gives the solution for the $m + n - 1$ time-terms, but the values of k_1 and k_2 are not yet determined. To find the best-fitting values of k_1 and k_2 , Equation 2-17 is first substituted into Equation 2-15, yielding

$$C - k_1 F - k_2 G = 0 \quad (2-18)$$

where

$$\begin{aligned} C &= AX - T \\ F &= AY - D \\ G &= AZ - E \end{aligned} \quad (2-19)$$

The matrices C , F , and G are each column matrices with L elements. To find the least-squares value of k_1 and k_2 , it is necessary to consider the equivalent system of L equations which can be formed from Equation 2-18. Considering the i^{th} such equation and using δ_i to designate the residual which results from fitting experimental data,

$$c_i - k_1 f_i - k_2 g_i = \delta_i \quad (2-20)$$

where c_i , f_i , and g_i are the i^{th} elements of the matrices C , F , and G , respectively. For k_1 and k_2 to best fit the data in the least-squares sense, the sum of the squared residuals must be a minimum with respect to k_1 and k_2 .

The expression for the sum I of the squared residuals is

$$I = \sum_{i=1}^L \delta_i^2 = \sum_{i=1}^L \left[c_i - (k_1 f_i + k_2 g_i) \right]^2 \quad (2-21)$$



Taking the partial derivative of I with respect to k_1 and equating the result to 0 yields the equation

$$k_1 \sum_{i=1}^L f_i^2 + k_2 \sum_{i=1}^L f_i g_i = \sum_{i=1}^L c_i f_i \quad (2-22)$$

or, employing the summation convention for repeated subscripts,

$$k_1 f_i f_i + k_2 f_i g_i = c_i f_i \quad (2-23)$$

Similarly, taking the partial derivative of I with respect to k_2 and equating the result to 0 yields

$$k_1 f_i g_i + k_2 g_i g_i = c_i g_i \quad (2-24)$$

Equations 2-23 and 2-24 may be solved for k_1 and k_2 , yielding

$$k_1 = \frac{(c_i f_i) (g_i g_i) - (c_i g_i) (f_i g_i)}{(f_i f_i) (g_i g_i) - (f_i g_i)^2} \quad (2-25)$$

and

$$k_2 = \frac{(f_i f_i) (c_i g_i) - (f_i g_i) (c_i f_i)}{(f_i f_i) (g_i g_i) - (f_i g_i)^2} \quad (2-26)$$

Equations 2-25 and 2-26 give the least-squares values for k_1 and k_2 in terms of known quantities. These values may then be substituted into Equation 2-17 to solve for the $m + n - 1$ time-terms and into Equation 2-14 to determine the two parameters of the refractor velocity.



2. Time-Term Model

The Moho refraction arrivals from Phase I, Phase III, and four land stations were processed through the time-term computer program. Input to the program were the time-distance pairs for each shot-station observation shown in Table II-3. The time-term for S8 was arbitrarily set equal to 0, thereby reducing the order of the matrix by 1 and removing the singularity in the coefficient matrix. After solving the system of equations, the normalizing constant α was reintroduced by assuming that shot E24 and station S2 were sufficiently close together to have identical time-terms (the separation was 2.9 km). The time-term results can be presented in either of two ways: shown in sec or converted to depths (H), where

$$H = P \frac{V_2 V_1}{\sqrt{V_2^2 - V_1^2}}$$

In this report, time-terms are converted to depths using a crustal velocity (V_1) of 6.4 km/sec for comparison with models developed using other techniques (i.e., refraction, wavefront, and model perturbation).

The time-term-model solution, Moho velocity, and rms residual (for all observations) are shown in Figure II-45. An examination of these results shows (in addition to observational scatter) that the refractor is dipping toward Amchitka and that the deepest part of the structure lies under the Phase III stations. This is in general agreement with the refraction-model and perturbation-model results; however, a large vertical mistie beneath Amchitka (S40) and an apparent lack of continuity between Phase III north shots and stations were noted.



Table II-3
SHOT/STATION EXPERIMENTAL DATA

Station	Explosion																					
	E34	E2	E3	E4	E5	E6	E30	E31	E32	E33	E7	E8	E15	E16	E17	E18	E19	E20	E21	E22	E24	E25
S1	x	x	x	x	x	x	x	x	x	x	x	x	x	x	x	x	x	x	x	x	x	
Phase I	S2	x	x	x	x	x	x	x	x	x	x	x	x	x	x	x	x	x	x	x	x	
	S5	x	x	x	x	x	x	x	x	x	x	x	x	x	x	x	x	x	x	x	x	
	S6	x	x	x	x	x	x	x	x	x	x	x	x	x	x	x	x	x	x	x	x	
	S7	x	x	x	x	x	x	x	x	x	x	x	x	x	x	x	x	x	x	x	x	
	S8	x	x	x	x	x	x	x	x	x	x	x	x	x	x	x	x	x	x	x	x	
	S9	x	x	x	x	x	x	x	x	x	x	x	x	x	x	x	x	x	x	x	x	
	S10	x	x	x	x	x	x	x	x	x	x	x	x	x	x	x	x	x	x	x	x	
	S23																x	x	x	x	x	x
	S25												x	x								
	S28												x	x	x	x	x	x	x	x	x	x
	S30												x	x	x	x	x	x	x	x	x	x
	S31												x	x	x	x	x	x	x	x	x	x
Land Station	S35 (Adak)	x	x	x	x	x					x	x	x	x	x	x	x	x	x	x	x	x
	S38 (Atka)	x	x								x	x	x	x	x	x	x	x	x	x	x	x
	S39 (Shemya)	x	x	x	x	x					x	x	x	x	x	x	x	x	x	x	x	x
	S40 (Amchitka)	x	x	x	x	x																

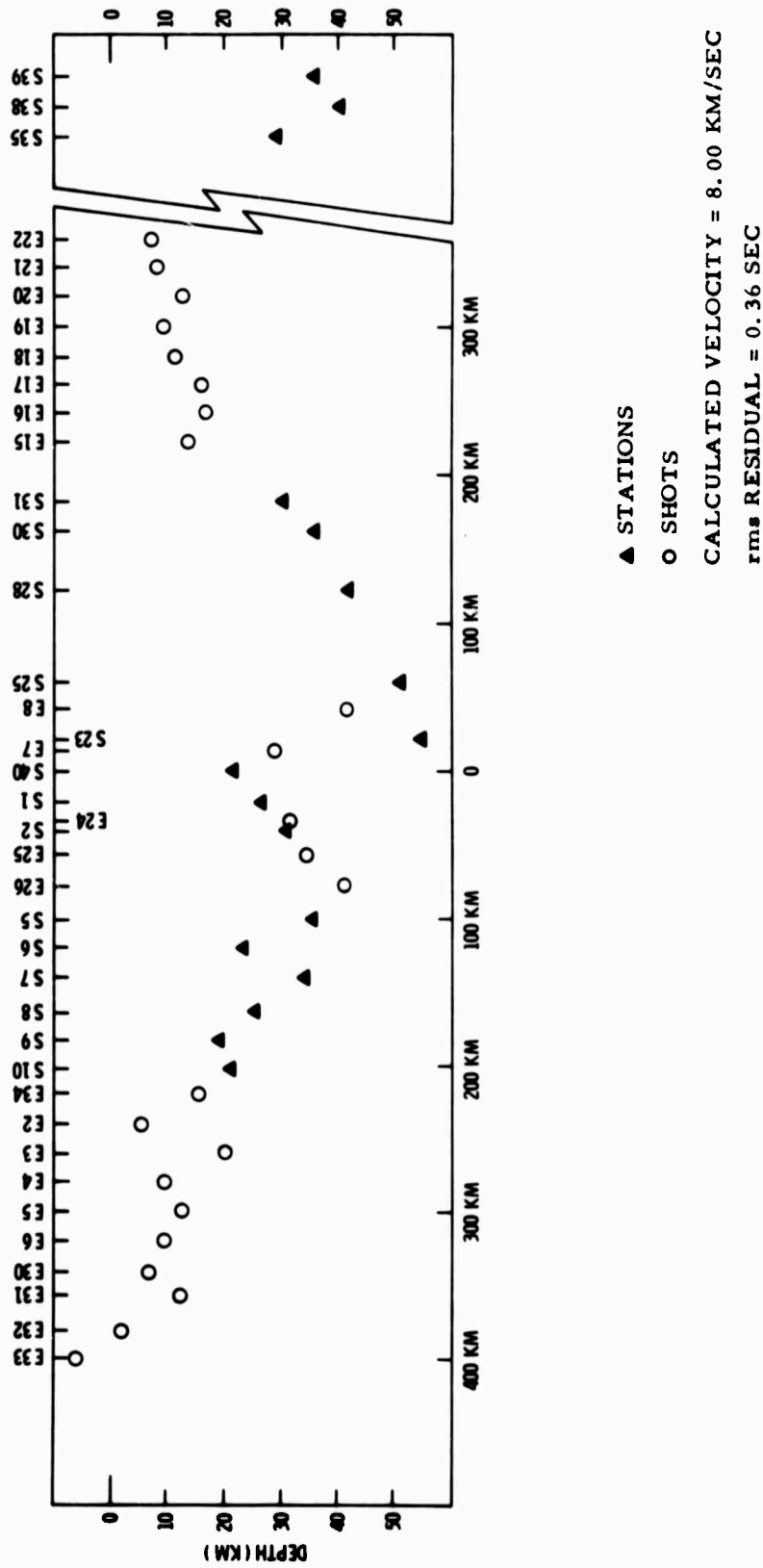


Figure II-45. Time-Term Model Using Data from Phase I, Phase III, and Land Stations at Adak, Atka, Shemya, and Amchitka (X4 vertical exaggeration)



The OBS unit and shot arrays were deployed in-line, while the land stations at Adak, Atka, Shemya, and Amchitka were generally off-line (Amchitka being most nearly in-line with the profile). Since scatter in some of the land-station observations was noted, the OBS data were processed independently; however, the Phase I and Phase III operations were conducted at different times which produced a singular observational matrix. The USC&GS station at Adak had very consistent arrival times and was included to provide a connection between Phase I and Phase III observations. The resulting time-term-model solution, Moho velocity, and rms residual (for all observations) are shown in Figure II-46. The results were not significantly different from previous results (Figure II-45).

Phase I and Phase III data were processed independently through the time-term program; and although better continuity could be obtained between Phase III north shots and stations by adjusting the Phase III constant (α), the structure shown under Amchitka was not continuous and exhibited essentially the same structural pattern as before.

The constrained velocity solutions for each of these cases (7.85 through 8.20 km/sec in increments of 0.5 km/sec) produced some tilting of the structure under the shots with respect to structure under the stations. However, the same basic structural pattern was observed (i. e., vertical mistie beneath Amchitka and poor continuity of structure beneath Phase III north shots and stations).

3. Theoretical Example

To examine the structure yielded by the time-term method for a simplified version of the final crustal model, the 2-layer crustal model of Figure II-47 (the interface of which is indicated by the solid line) was input to the theoretical traveltime program. The resulting theoretical traveltimes were then input to the time-term program, yielding the time-term depths indicated by the points in Figure II-47.

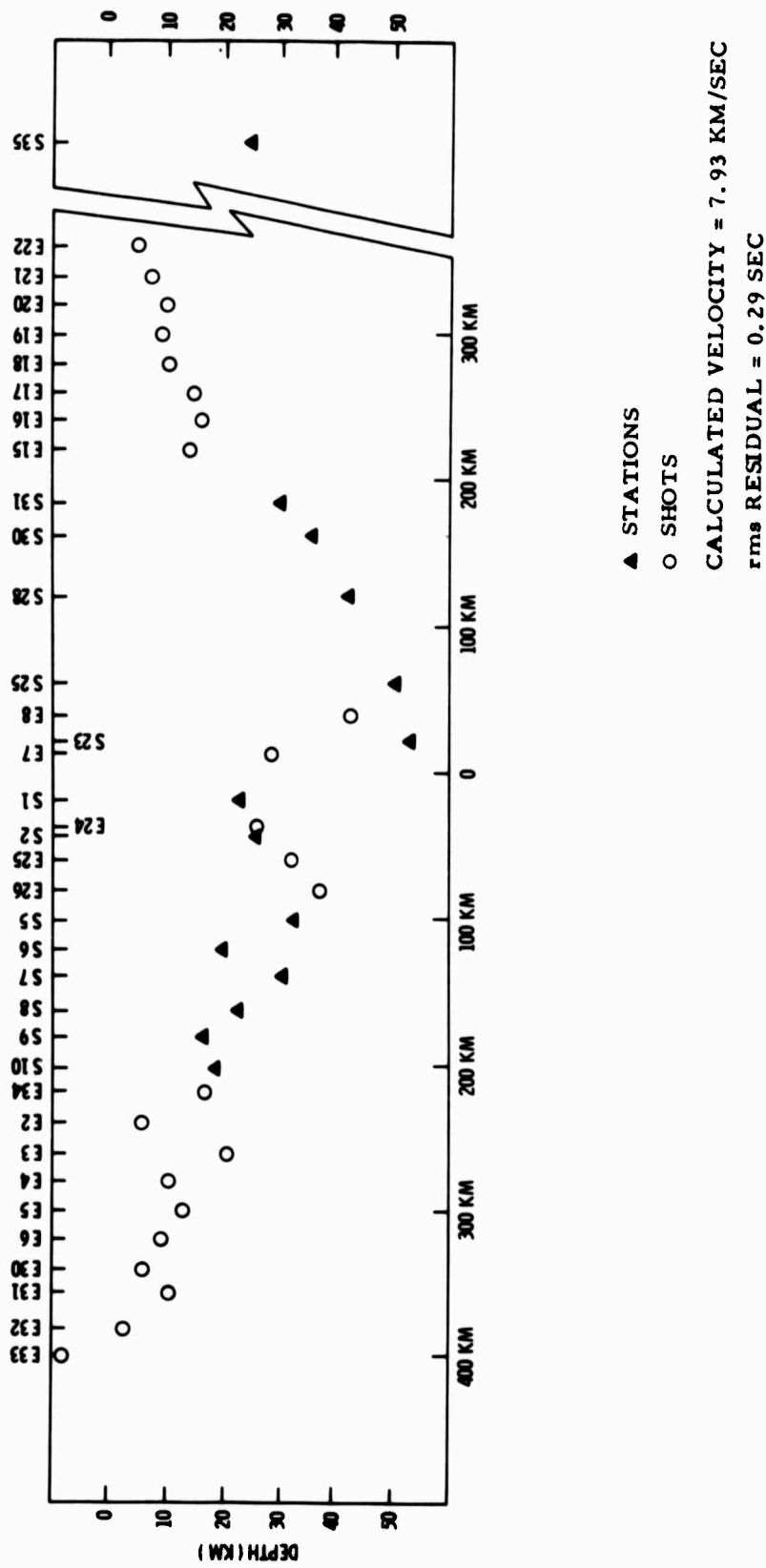


Figure II-46. Time-Term Model Using Data from Phase I, Phase III,
and Adak Land Station (X4 vertical exaggeration)

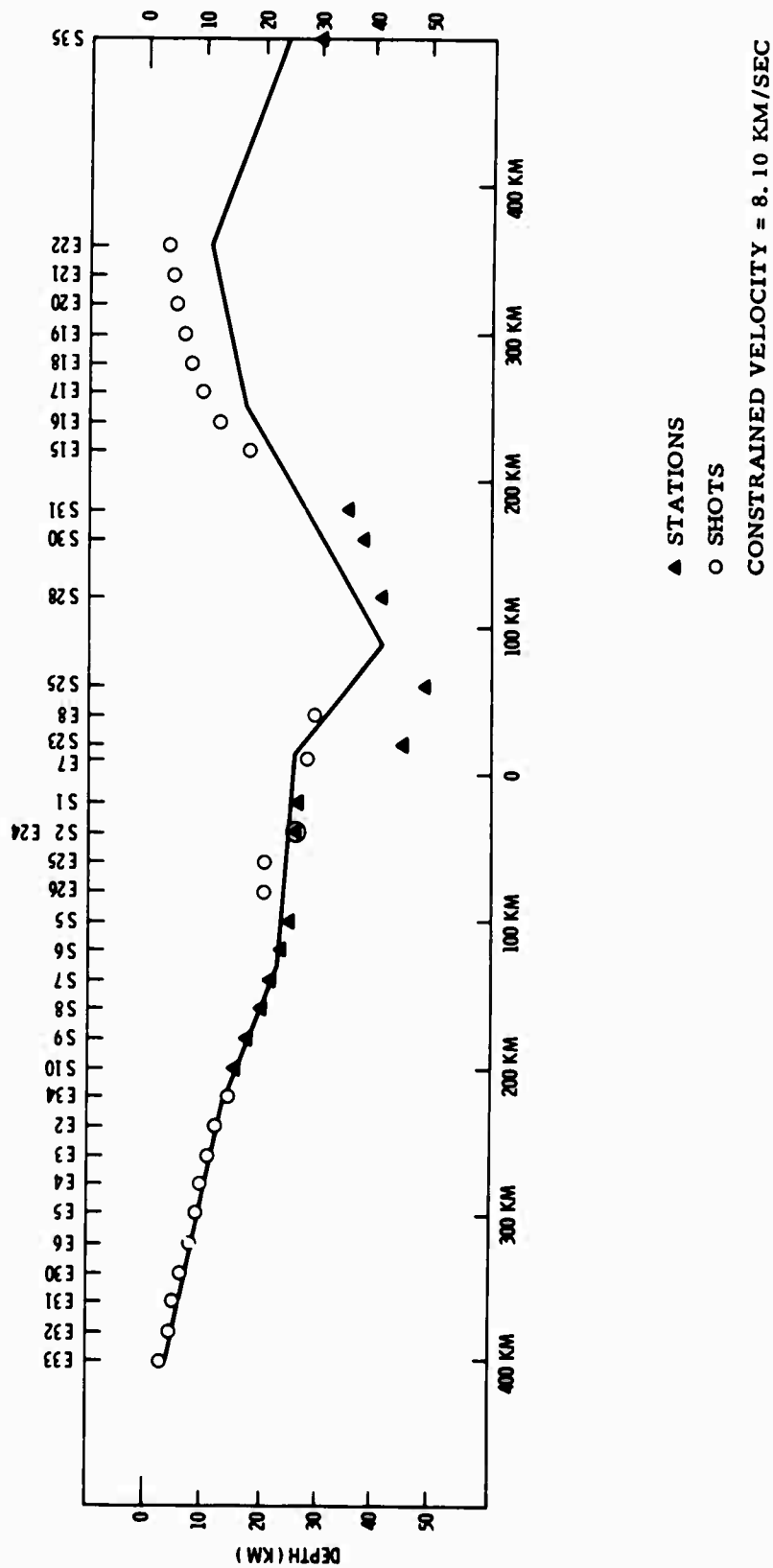


Figure II-47. Time-Term Results Using Theoretically Computed Traveltimes.
The interface of the theoretical model (with dip angles less than 11.8°) is indicated by the solid line ($\times 4$ vertical exaggeration).



Table II-4 shows the shot/station pairs used in computing the time-term depths. Inspection of Figure II-47 and Table II-4 shows that generally poor results are obtained by the time-term method for those stations under the root of the model, i.e., stations S23, S25, S28, S30, and S31 and those shots which connect with them. Relatively good agreement between the true model and the time-term depths is obtained for those sites not associated with the deepest parts of the model structure, i.e., those sites to the left of E26.

Since some of the disagreement between the true and the time-term depths might be attributable to violation of the assumption that the cosines of the dip angles may be approximated by unity, another model, with shallower dip angles, was input to the time-term program. The model and the time-term depths derived from it are shown in Figure II-48. The largest dip angle for the model of Figure II-47 was 11.8° ; the largest dip angle for the model of Figure II-48 was 5.2° . Although the time-term fit is somewhat better in this example, substantial deviation from the true model still occurs for the stations located over the root of the structure and the shots associated with them. This deviation supports the conclusion of previous investigations¹² that the time-term method is not fully suitable for deriving the structure under a site when the interface within the cone of critically refracted rays from that site deviates substantially from planarity.

E. TRAVELTIME ANALYSIS

1. Traveltime Program

A traveltime program was developed to compute theoretical traveltimes for crustal models with layers which change dip. The program contains a plot option so that the model may be plotted by computer, if desired; a computer-generated plot of a typical model is shown in Figure II-49.



Table II-4
SHOT/STATION THEORETICAL DATA

Station	Explosion																					
	E34	E2	E3	E4	E5	E6	E30	E31	E32	E33	E7	E8	E15	E16	E17	E18	E19	E20	E21	E22	E24	E25
S1	X	X	X	X	X	X	X	X	X	X	X	X										
S2	X	X	X	X	X	X	X	X	X	X	X	X										
S5	X	X	X	X	X	X	X	X	X	X	X	X										
S6	X	X	X	X	X	X	X	X	X	X	X	X										
S7	X	X	X	X	X	X	X	X	X	X	X	X										
S8	X	X	X	X	X	X	X	X	X	X	X	X										
S9	X	X	X	X	X	X	X	X	X	X	X	X										
S10	X	X	X	X	X	X	X	X	X	X	X	X										
S23											X	X	X	X	X	X	X	X	X	X	X	X
S25											X	X	X	X	X	X	X	X	X	X	X	X
S28											X	X	X	X	X	X	X	X	X	X	X	X
S30											X	X	X	X	X	X	X	X	X	X	X	X
S31											X	X	X	X	X	X	X	X	X	X	X	X
S35											X	X	X	X	X	X	X	X	X	X	X	X

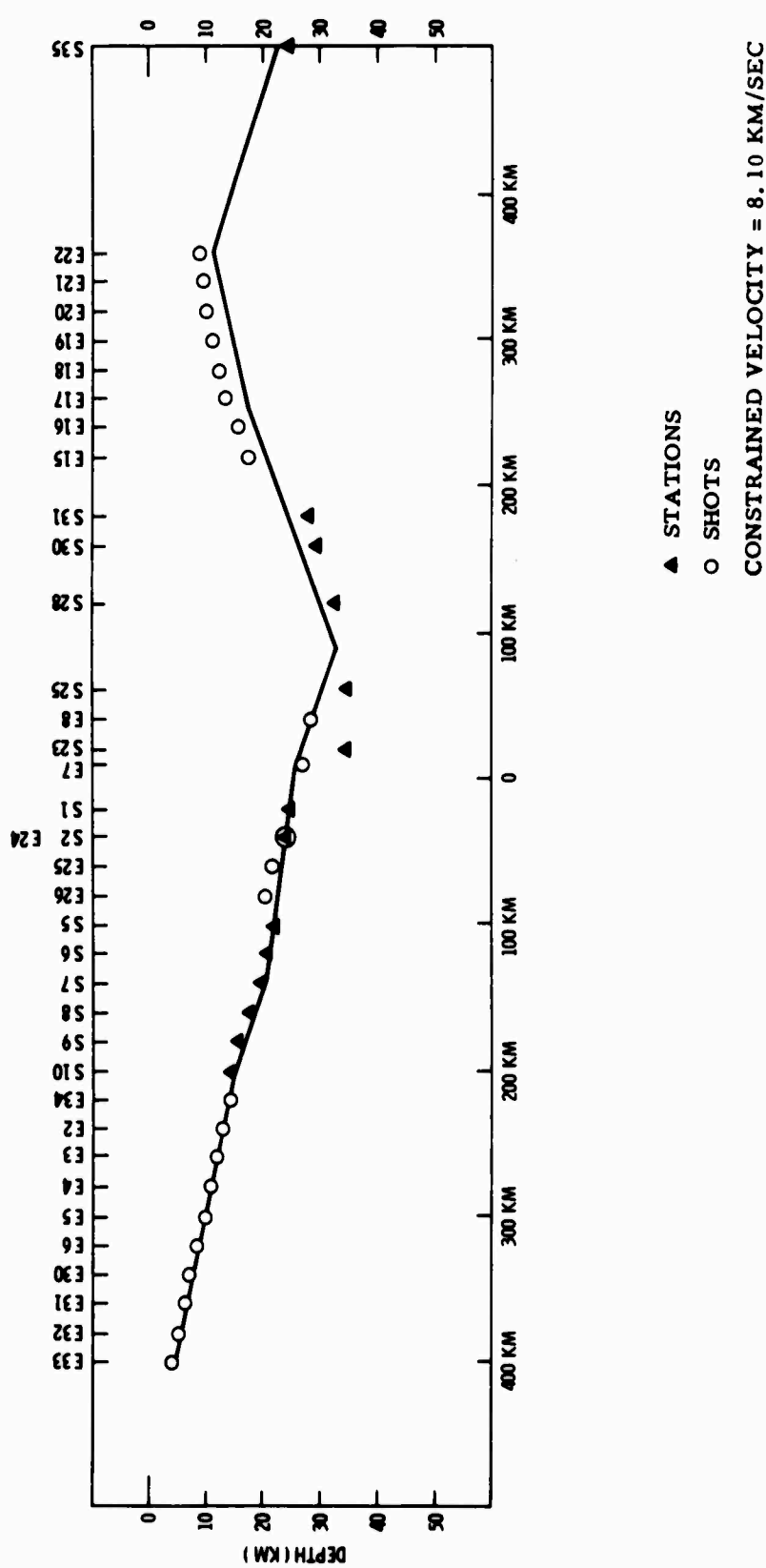


Figure II-48. Time-Term Results Using Theoretically Computed Traveltimes.
The interface of the theoretical model (with dip angles less than 5.2°) is indicated by the solid line (X4 vertical exaggeration).

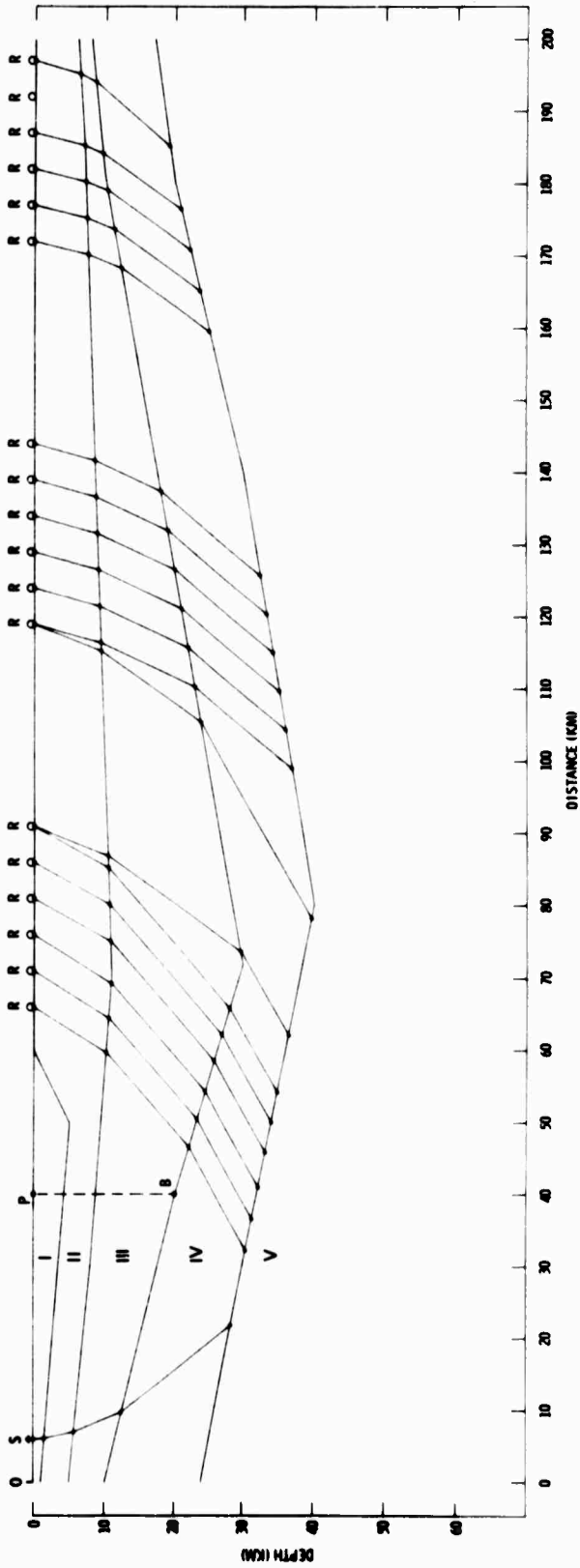


Figure II-49. Example of Output from Program Which Computes Traveltimes for Crustal Models with Layers that Change Dip



The model is input to the program by describing the interface above each layer in terms of the horizontal distance and vertical depth from the origin (0 in Figure II-49) to each point on the interface at which a change of dip angle occurs (e.g., the point B on the interface above layer IV, where the distance and depth are OP and PB, respectively). The program will accept a total of nine layers and a half-space and a maximum of 80 breakpoints (such as point B) in any one interface. Also, a P-wave velocity for each layer is read in.

The locations of both sources (e.g., points S) and receivers (e.g., points R) are specified in terms of their horizontal distances from the origin and the number of the interface on which they lie; sources and receivers may be specified to lie on separate interfaces. One hundred source locations and 100 receiver locations may be specified.

Ray paths are computed by geometrical acoustics; rays are assumed to enter and exit the refracting layer at the critical angle, following the contours of the interface above the refractor between entry and exit. Ray paths from the source S to the refractor (layer V) and from the refractor to the receivers R are also shown in Figure II-49. For a given input model, in addition to the options described above, the program may be recycled to compute traveltimes for additional source and receiver locations or for different refracting layers.

2. Perturbation Model

The traveltime program was used to perturb the crustal model across Amchitka to give a best fit to the observed traveltimes. The technique follows.



Given an estimate of the 2-dimensional model, the theoretical traveltimes for each shot/station pair are computed. In addition, the program computes a residual (experimental traveltime minus theoretical travelttime) for each shot/station pair having an experimental observation and subsequently calculates the mean-absolute-value and the root-mean-square of the residuals to give a measure of how well the theoretical model fits the experimental traveltimes. An inspection of the traveltime residuals allows determination of areas along the refracting interface where the structure should be flexed to give a closer fit to the observed traveltimes. The method, of course, considers the actual ray paths involved. The flexed model is input to the computer; theoretical traveltimes are determined; and residuals are computed as before. The model is then flexed again and the process repeated as necessary to produce a model which fits the experimental observations.

The initial model was the refraction model, with the refracting interface connected across areas where no coverage was obtained in the standard refraction analysis. Average crustal velocity was taken as 6.4 km/sec. Shown in Figures II-50 and II-51 are the initial model and the series of model perturbations. Mean-absolute-values (mav) and root-mean-squares (rms) of the traveltime residuals for each model are given in Table II-5. The model was perturbed eight times.

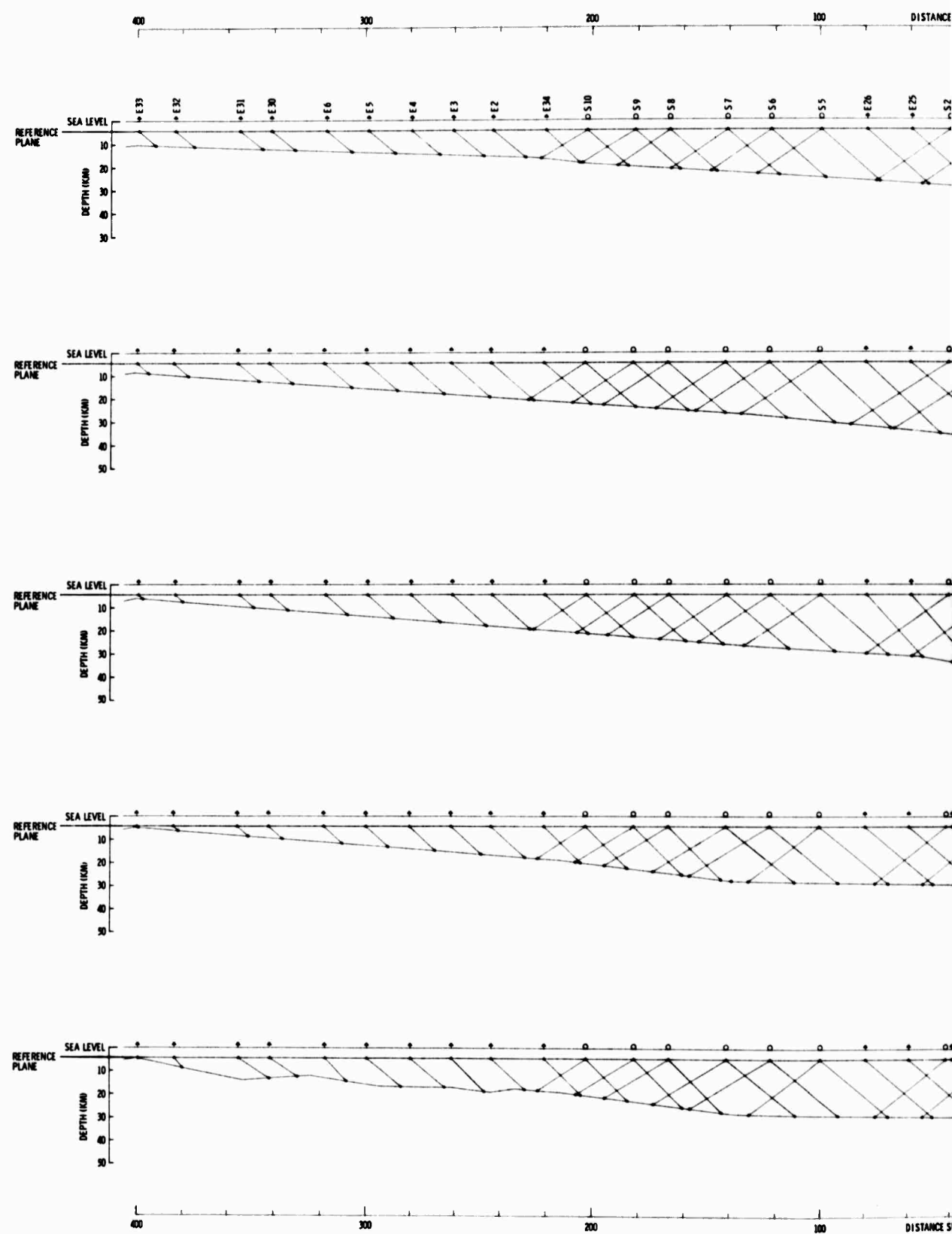
Due to the contour of the refracting interface (which is comprised of many straight-line segments), a theoretical observation was not obtained at shot E8 for iterations 3, 4, and 5, which excluded the experimental observations of E8 to S2, S5, S6, S7, S8, S9, and S10 from those mav and rms calculations. This resulted in an increase of those values on iteration 6 for which a theoretical observation was obtained at shot E8.



Figure II-51 (iteration 8) shows the final model, where the mav was 0.45 sec and the rms was 0.56 sec. Additional model perturbations could undoubtedly improve these values somewhat; however, it is felt that they essentially represent the contributions due to observational scatter in the experimental data. The model-perturbation method of crustal determination gives a good representation of the contour of the refractor across the profile, is not restricted by various assumptions necessary to implement other methods (e.g., standard refraction and time-term), and allows a direct measure of how well the model fits the observations. The final perturbation model (iteration 8) is a 2-dimensional determination from in-line profile recordings. Although the crustal parameters cannot be uniquely determined from the available data, the model gives a good fit to the seismic observations. The deepest part of the structure lies under the Petrel Bank, and the root of the structure is located 60 km north of Amchitka under Semisopochnoi Island.

Table II-5
TRAVELTIME RESIDUAL VALUES

	<u>mav</u> (sec)	<u>rms</u> (sec)
Refraction Model	0.61	0.77
Iteration 1	0.63	0.78
Iteration 2	0.53	0.65
Iteration 3	0.50	0.62
Iteration 4	0.43	0.54
Iteration 5	0.42	0.53
Iteration 6	0.48	0.60
Iteration 7	0.46	0.59
Iteration 8	0.45	0.56



A

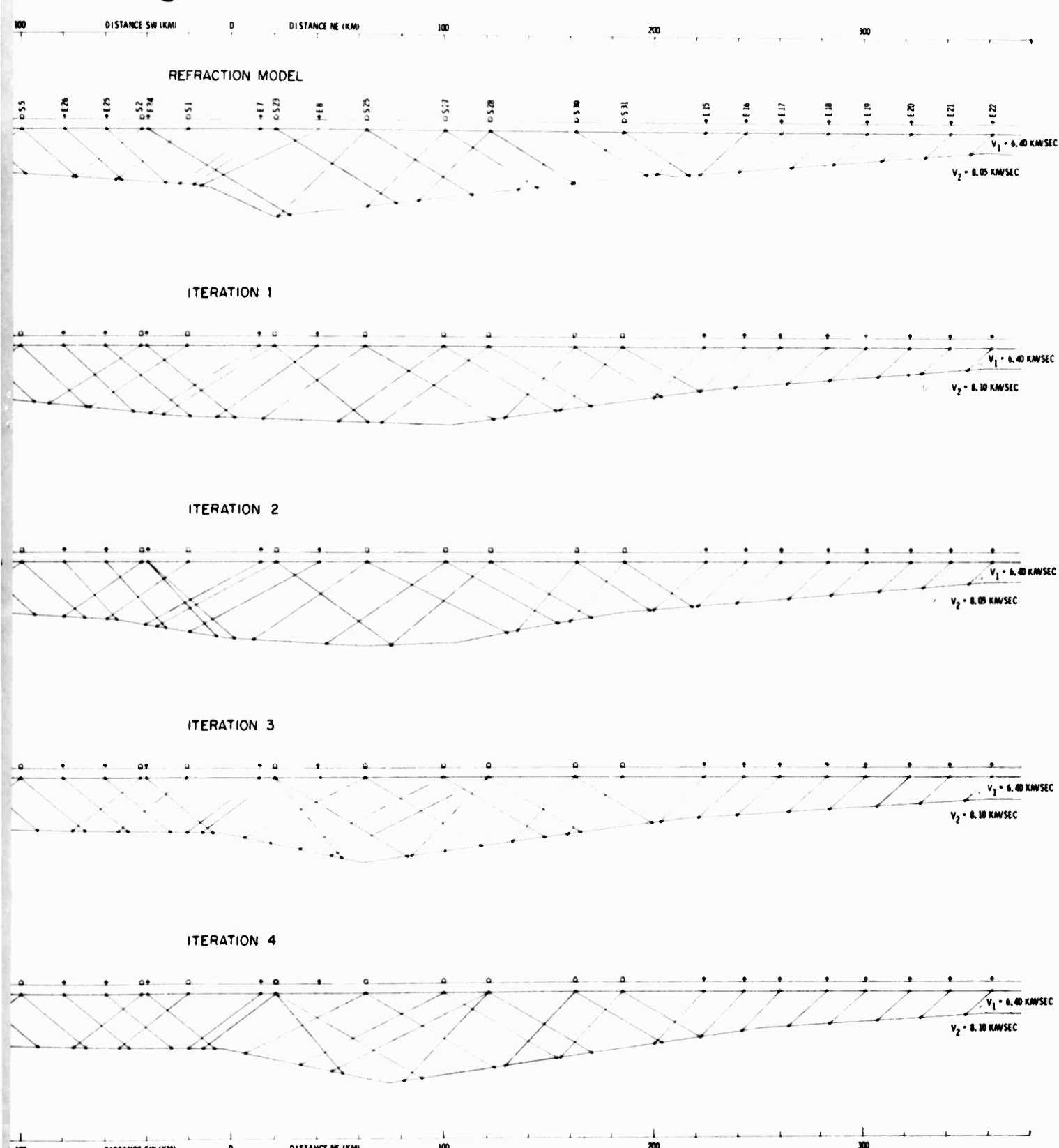
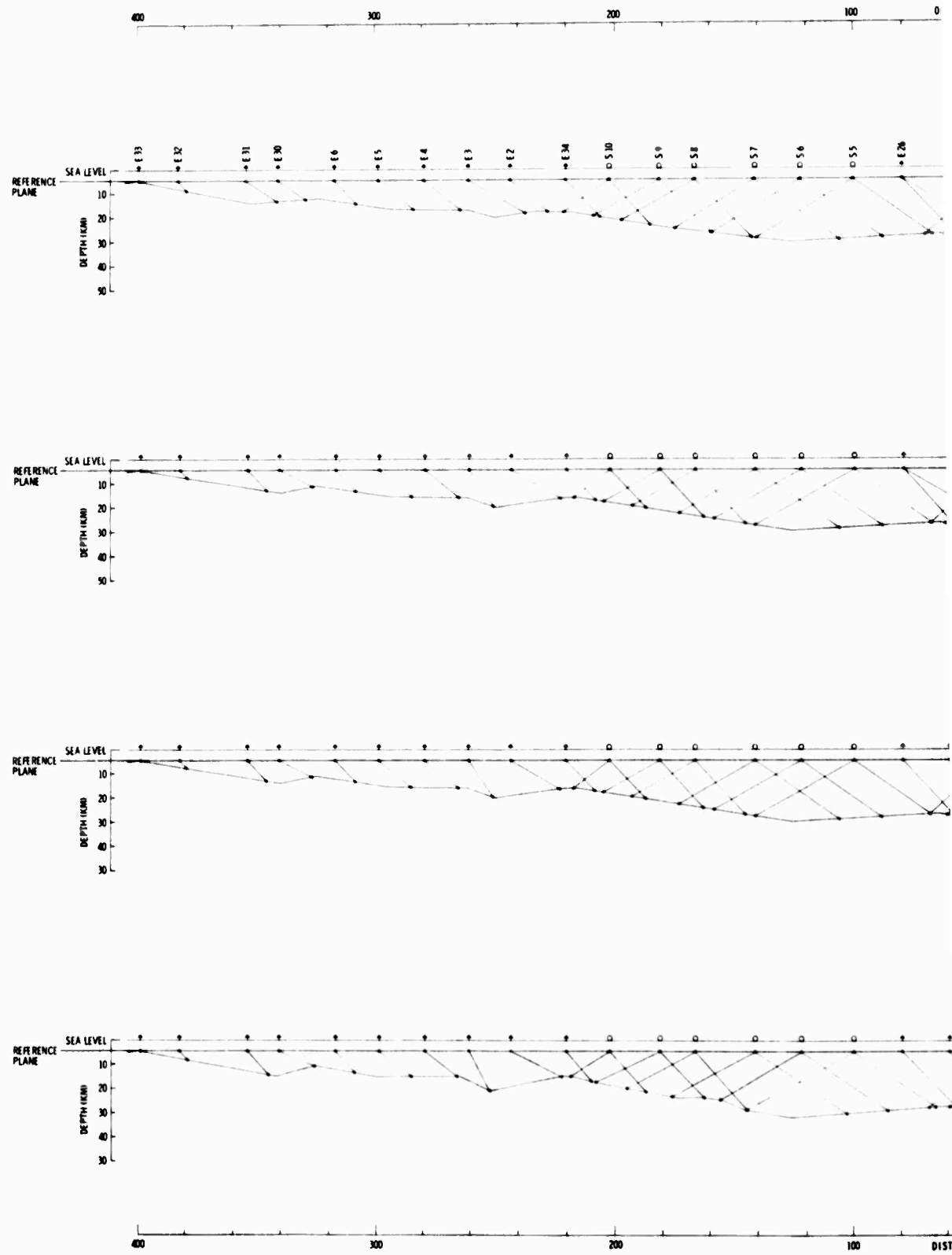


Figure II-50. Model-Perturbation Results Showing Initial (refraction) Model and Iterations 1 Through 4



A

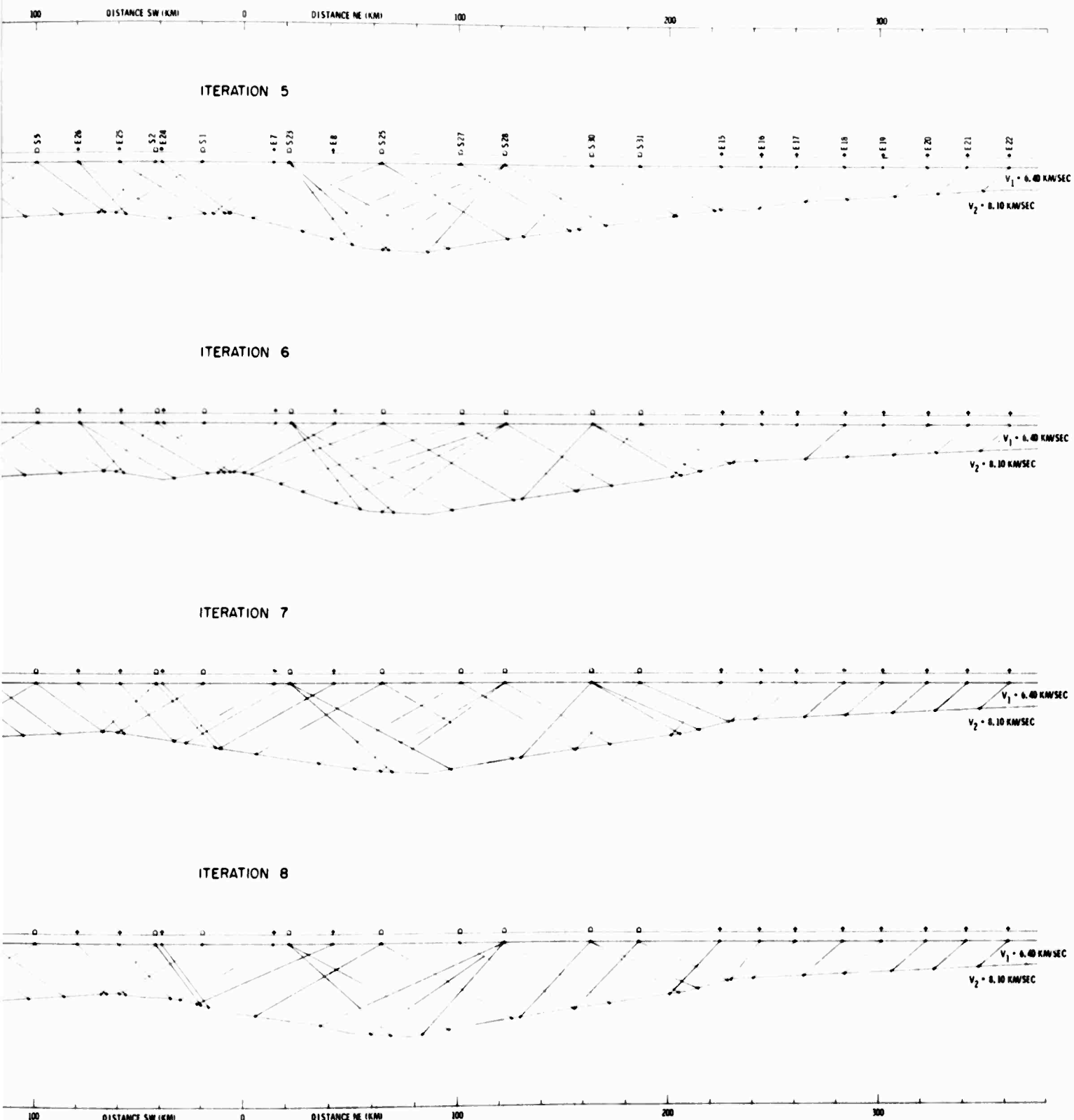


Figure II-51. Model-Perturbation Results Showing Iterations 5 Through 8



SECTION III

EFFECT OF CRUSTAL STRUCTURE ON REGIONAL TRAVELTIMES

This section presents results of calculations made to determine the effect of the Amchitka crustal structure on traveltimes observed at regional distances.

Utilizing the computer program described in Section II, subsection E, traveltime curves were determined for the symmetrical model shown in Figure III-1. The model consists of a standard (JB) 33-km crust with an average crustal velocity of 6.05 km/sec overlying a simplified upper mantle structure made up of several concentric constant-velocity layers. Ray paths are shown for the refraction in layer 7, which is the first arrival in the 20° distance range. The calculated traveltime curve for this refraction is shown in Figure III-2.

Next, the model was modified simply by replacing the standard crust on the left side of the model with the Amchitka Crust (the upper mantle structure being unchanged) to give the dual model shown in Figure III-1. Traveltime curves were computed for the same refracting layer; these curves are presented in Figure III-2 for comparison with the symmetrical model results. The shape of the traveltime curve essentially reflects the inverted contour of the Moho refractor across Amchitka. In addition, the traveltime curve is 0.5 to 2 sec earlier than that for the model with the standard crust, due primarily to differences in the crustal velocity of the Amchitka model (6.4 km/sec) and the JB model (6.05 km/sec).

For an event 20° from Amchitka recorded along the OBS profile (or for a series of events along the OBS profile recorded at 20° distance), a traveltime variation of about 1.5 sec is observed because of changes in the



crustal structure along that profile. Given the true upper mantle structure of the region (and resultant traveltimes curve), variations of \pm 0.7 sec are observed if changes in crustal structure are neglected. These variations are quite often interpreted as observational scatter. While these variations may be small compared to traveltimes resulting from incorrect upper mantle models, they are not insignificant.



Figure III-1. Crustal Refraction Ray Paths for Symmetrical Model, Standard Crust (top), and Dual Model, Anchitka Crust with Standard Crust (bottom)

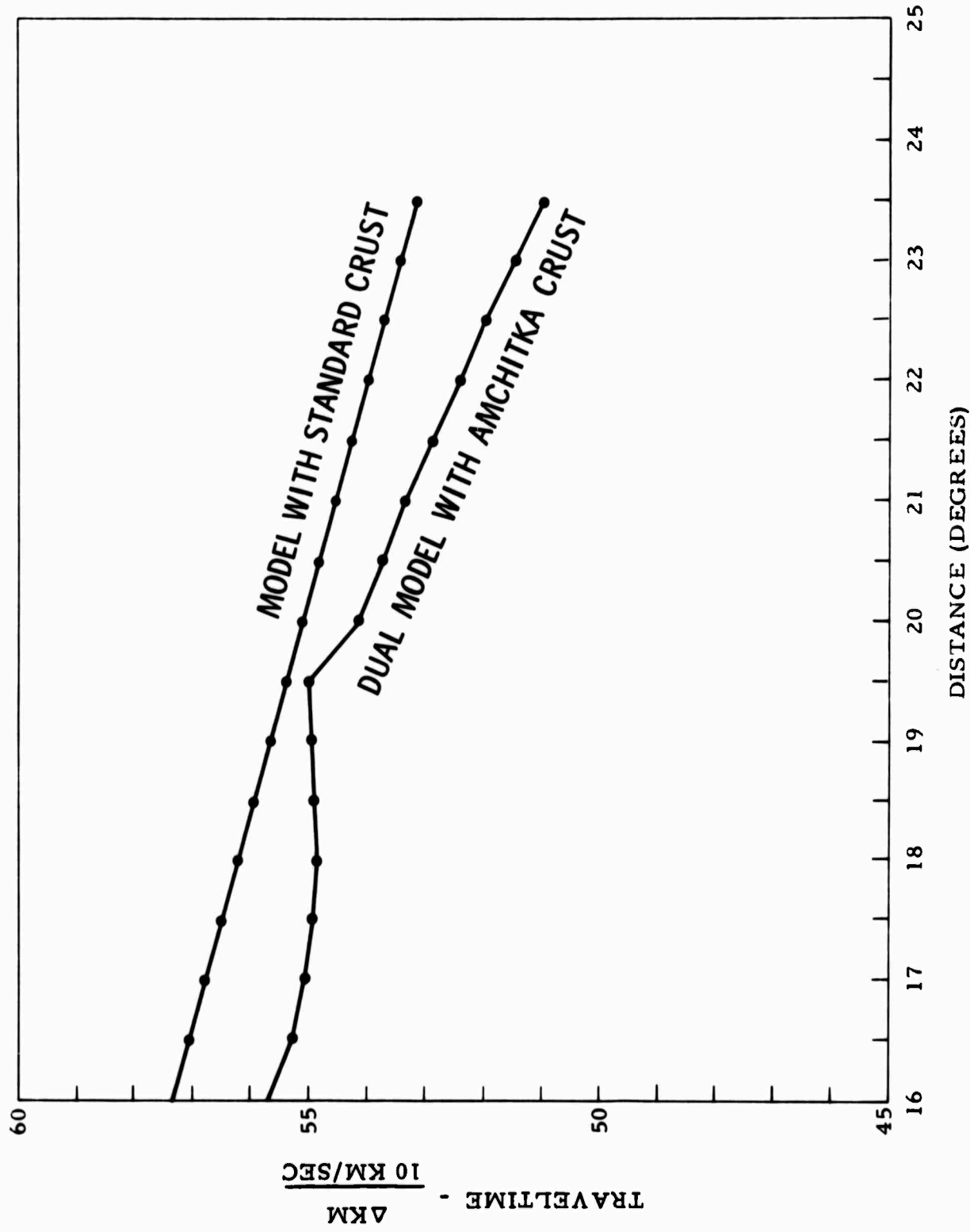


Figure III-2. Reduced Traveltimes for Symmetrical Model and Dual Model



SECTION IV

REFERENCES

1. Texas Instruments Incorporated, 1968: Operations Report, Aleutian Islands Ocean-Bottom Seismographic Experiments, Contract F33657-67-C-1341, 31 Jan.
2. Texas Instruments Incorporated, 1968: Ocean-Bottom Seismograph System-Response Study, Contract F33657-67-C-1341, 31 Jan.
3. Texas Instruments Incorporated, 1968: Preliminary Analysis Report, Aleutian Islands Experiment — Ocean-Bottom Seismographic Experiments, Contract F33657-67-C-1341, 31 Jan.
4. Texas Instruments Incorporated, 1968: Final Report, Ocean-Bottom Seismograph Experiments, Contract F33657-68-C-0875, 23 Aug.
5. Shor, George G. Jr., 1962, Seismic refraction studies off the coast of Alaska: Bull. Seis. Soc. Am., v. 52, p. 37-57.
6. Shor, George, G. Jr., 1964, Structure of the Bering Sea and the Aleutian Ridge: Marine Geol., v. 1, p. 213-219.
7. Thornburg, H. R., 1930, Wavefront diagrams in seismic interpretation: Bull. A. A. P. G., v. 14, p. 185-200.
8. Rockwell, D. W., 1967, A general wavefront method: Seismic Refraction Prospecting, Tulsa, SEG, p. 363-413.
9. Schenck, Frederick L., 1967, Refraction solutions and wavefront targeting: Seismic Refraction Prospecting, Tulsa, SEG, p. 416-425.
10. Scheidegger, A. E., and P. L. Willmore, 1957, The use of a least squares method for the interpretation of data from seismic surveys: Geophys., v. 22, n. 1, p. 9.
11. Smith, T. J., J. S. Steinhart, and L. T. Aldrich, 1966, Lake Superior crustal structure: Geol. Res., v. 71, p. 1141.
12. O'Brien, P. N.S., 1968, Lake Superior crustal structure — a reinterpretation of the 1963 seismic experiment: J. Geol. Res., v. 73, p. 2669.



13. Steinhart, John S., and R. P. Meyer, 1961: *Explosion Studies of Continental Structure*, Carnegie Institute of Washington, Pub. 622, Chapter 4.
14. Acton, F.S., 1959: *Analysis of Straight Line Data*, John Wiley and Sons, p. 135.
15. Davies, O. L., 1958: *Statistical Methods in Research and Production*, Oliver and Boyd, p. 173-174.
16. Dobrin, M. D., 1960: *Introduction to Geophysical Prospecting*, McGraw-Hill, p. 81-83.
17. Davies, O. L., 1958: *Statistical Methods in Research and Production*, Oliver and Boyd, p. 41.
18. Mood, A. M., and F. A. Grayhill, 1963: *Introduction to the Theory of Statistics*, McGraw-Hill, Chapter 8.



APPENDIX CONFIDENCE LEVELS

A study was undertaken to arrive at statistical confidence limits for the parameters of the determined refraction crustal model. Given the interval (a, b) denoted by the limits a and b and a confidence level N, confidence limits stated for a quantity may be interpreted as follows: the interval (a, b) will cover the desired quantity 100 N-percent of the time.

For example, suppose it is desired to place 0.95-percent confidence limits on the mean of a normal distribution, given four independent samples from that distribution having a variance equal to 9. Using the sample mean of the observation \bar{X} as the estimate of the true mean μ (this is the maximum-likelihood estimate of μ), it can be shown that

$$P \left\{ \bar{X} - 2.94 \leq \mu \leq \bar{X} + 2.94 \right\} = 0.95 \quad (A-1)$$

If the four samples taken are such that $\bar{X} = 2.7$, then $a = -0.24$ and $b = 5.64$ so that $(-0.24, 5.64)$ is the 95-percent confidence interval on μ . For a different set of four samples, the values of a and b are different.

The first step in arriving at confidence limits for the parameters of the crustal model was the fitting of the points of the time-distance plots to straight-line segments. Ordinarily, this is done by a simple least-squares fit, assuming that the distance errors in the data are much smaller than the time error.¹³ Since this condition cannot be assumed to hold for the present data, it was decided to employ a line fit which assumes both distance and time data to be subject to error and to compare the results with standard least-squares-error fits.

The equation for a straight line has the form

$$t = \bar{t} + \hat{b} (\bar{X} - \bar{X}) \quad (A-2)$$



where b is the slope. \bar{X} is given by

$$\bar{X} = \frac{1}{N} \sum_{i=1}^N X_i \quad (A-3)$$

and

$$\bar{t} = \frac{1}{N} \sum_{i=1}^N t_i \quad (A-4)$$

In Equations A-3 and A-4, N is the number of data points to be fitted.

For the case where $\{X_i\}$ and $\{t_i\}$ are uncorrelated sample sets from bivariate normal distributions, it can be shown that the maximum-likelihood estimate \hat{b} for the slope of the straight line satisfies^{14, 15}

$$\hat{b}^2 - 2mb - K^2 = 0 \quad (A-5)$$

where

$$K^2 = \frac{\sigma_t^2}{\sigma_x^2} \quad (A-6)$$

and

$$m = \frac{\sum_{i=1}^N (t_i - \bar{t})^2 - K^2 \sum_{i=1}^N (X_i - \bar{X})^2}{2 \sum_{i=1}^N (X_i - \bar{X})(t_i - \bar{t})} \quad (A-7)$$

Knowing the nature of the data permits a unique solution of Equation A-5 to be written as

$$\hat{b} = m + \sqrt{m^2 + K^2} \quad (A-8)$$



It is seen from Equations A-6, A-7, and A-8 that it is not necessary to know both σ_t^2 and σ_x^2 (the standard deviations of $\{X_i\}$ and $\{t_i\}$) but only their ratio. Given the result of Equation A-8, σ_x^2 can be estimated from the N data points by

$$\hat{\sigma}_x^2 = \frac{\sum_{i=1}^N (X_i - \bar{X})^2}{N - 2} - \frac{\sum_{i=1}^N (X_i - \bar{X})(t_i - \bar{t})}{(N - 2)\hat{b}} \quad (A-9)$$

Using Equation 2-2, it is seen that \hat{t}_o is given by

$$\hat{t}_o = \bar{t} - \hat{b} \bar{X} \quad (A-10)$$

when the line is required to pass through the mean of the observations. Therefore, the line which best fits the data when both variables are in error has a slope given by Equation A-8 and an intercept given by Equation A-10.

For the problem under consideration, X corresponds to the distance between signal source and receiver and t to the measurement of epoch. It should be noted that the distance error arises from three considerations: curvature of the earth, error in longitude, and error in latitude.

The circumference of the earth is 21,600 nautical miles. If a great circle arc is used, the plane angle subtended for a 400-nautical mile arc is 0.116 radians or 6.65° . The chord length is then within 0.5 percent of the arc length. Hence, it will be assumed that the chord and arc lengths are identical for the range of arc lengths encountered.

The following model seems appropriate for estimating the error in distance. Let (X_1, Y_1) be coordinates of the signal source and (X_2, Y_2) be the coordinates of the receiver. Assume further that the errors in placement of the source and receiver are statistically independent, that



(X_1, Y_1) and (X_2, Y_2) are samples from bivariate normal distributions with identical diagonal covariance matrices (X and Y errors are uncorrelated), and that the mean vectors are $(0, 0)$, and $(d, 0)$, respectively. In general, the distance between source and receiver is given by

$$D = \sqrt{(X_2 - X_1)^2 + (Y_2 - Y_1)^2} \quad (A-11)$$

Since X_1, X_2, Y_1 , and Y_2 are Gaussian random variables, it is seen that

$$X = (X_2 - X_1) \sim N(d, 2\sigma^2) \quad (A-12a)$$

and

$$Y = (Y_2 - Y_1) \sim N(0, 2\sigma^2) \quad (A-12b)$$

In addition, X and Y are uncorrelated. This latter statement follows from the diagonal-matrices discussion above. The distance, which is not normally distributed, is then

$$D = \sqrt{X^2 + Y^2} \quad (A-13)$$

It should be recalled that the assumptions made to obtain the maximum-likelihood estimate \hat{b} for the slope of the line used to fit the data required that the distance error be normally distributed. It appears that a reasonable approximation can be made for the distance if the variance $\sigma^2 \ll d^2$, since under this condition the effects of errors in the Y_1 and Y_2 coordinates are negligible in Equation A-13. The distance is modeled as

$$D = X_2 - X_1 \quad (A-14)$$

This statement can be written as

$$D = d + E_x \quad (A-15)$$



where E_x is a Gaussian random variable with zero mean and variance of $2\sigma^2$.
The variance in source or receiver placement is σ^2 .

Using these approximations, the development of the estimate \hat{b} is valid, provided K^2 is written as

$$K^2 = \frac{\sigma_t^2}{2} = \frac{\sigma_t^2}{2\sigma_x^2} \quad (A-16)$$

An estimate was made of the approximate value of Equation A-16 using previous experience as a guide. The value obtained from this procedure is $K^2 = 1.5 \times 10^{-3} \text{ sec}^2/\text{km}^2$ ($\sigma_t^2 = 1.57 \times 10^{-2} \text{ sec}^2$, and $\sigma_x^2 = 10.4 \text{ km}^2$). This value is used in all final computations which utilize Equation A-6 or A-16.

Once the line segments are fitted to the data using Equations A-2 and A-8 on each segment, standard formulas¹⁶ are employed to calculate the value of each parameter of the model using the fitted lines, slopes, and intercept values.

At this point, it is desirable to develop an expression, or at least bounds, for the variance of each estimated quantity. The ultimate objective is to establish confidence limits on each estimated quantity. An approximate expression for the variance $\sigma^2(F)$ of a function $F(X_1, X_2, \dots, X_n)$ is given by¹⁷

$$\sigma^2(F) = \left(\frac{\partial F}{\partial X_1} \right)^2 \sigma^2(X_1) + \left(\frac{\partial F}{\partial X_2} \right)^2 \sigma^2(X_2) + \dots + \left(\frac{\partial F}{\partial X_n} \right)^2 \sigma^2(X_n) \quad (A-17)$$

when the $\{X_i\}$ are mutually independent and includes covariance terms of the form

$$\left(\frac{\partial F}{\partial X_i} \right) \left(\frac{\partial F}{\partial X_j} \right) \text{cov}(X_i, X_j) \quad (A-18)$$



when the X_i are not mutually independent. The quantities for which estimates of the variance are desired are the velocity in the refractor, the dip angle of the interface, and the depths to the refractor at each end of the reverse profiles. The velocity in the refractor is given by

$$\hat{v}_2 = \frac{v_1}{\sin \theta} \quad (A-19)$$

where v_1 is the crustal velocity, assumed to be without error. θ is a function of the estimates of the slopes of the fitted lines and is given by

$$\hat{\theta} = \frac{1}{2} [\arcsin (\hat{v}_1 \hat{b}_d) + \arcsin (\hat{v}_1 \hat{b}_u)] \quad (A-20)$$

where \hat{b}_d is obtained using Equation A-8 and the down-dip traveltime and distance data and where \hat{b}_u is obtained from the data recorded shooting up-dip.

The dip angle between the crust and refractor is

$$\hat{\delta} = \frac{1}{2} [\arcsin (\hat{v}_1 \hat{b}_d) - \arcsin (\hat{v}_1 \hat{b}_u)] \quad (A-21)$$

The two depths are

$$\hat{h}_{ou} = \frac{v_1 \hat{t}_{ou}}{2 \cos(\hat{\theta}) \cos(\hat{\delta})} \quad (A-22)$$

and

$$\hat{h}_{od} = \frac{v_1 \hat{t}_{od}}{2 \cos(\hat{\theta}) \cos(\hat{\delta})} \quad (A-23)$$

where t_{ou} and t_{od} are the intercepts of the line fits for the up-dip and down-dip data, respectively.



In the succeeding work, approximate values for the variance of each of these quantities are obtained assuming the covariance terms of Equation A-18 are negligible for the (t_o, b_i) pairs. This follows the work of Davies.¹⁵ Variances of the estimated quantities related to the fitting of the lines to the data sets are¹⁵

$$\sigma^2(\hat{b}) = \frac{\left(K^2 + \hat{b}^2\right)^2 \left[\sum_{i=1}^N (t_i - \bar{t})^2 - \hat{b} \sum_{i=1}^N (X_i - \bar{X})(t_i - \bar{t}) \right]}{K^2(N-2) \left[K^2 \sum_{i=1}^N (X_i - \bar{X})^2 + \hat{b} \sum_{i=1}^N (X_i - \bar{X})(t_i - \bar{t}) \right]} \quad (A-24)$$

$$\sigma^2(\hat{t}_o) = \frac{\sigma^2(\bar{t})}{N} + (\bar{X})^2 \sigma^2(\hat{b}) + \hat{b}^2 \sigma^2(\bar{X}) \quad (A-25)$$

$$\sigma^2(\bar{X}) = \frac{\sigma_x^2}{N} = \frac{2\sigma^2}{N} \quad (A-26)$$

and

$$\sigma^2(\bar{t}) = \frac{\sigma_t^2}{N} \quad (A-27)$$

These expressions are obtained using Equations A-17, A-8, A-10, A-3, and A-14. It can now be shown that the expressions for the desired variance are given by

$$\sigma^2(\hat{V}_2) = \frac{v_1^4 \cot(\hat{\theta})}{4 \sin^2(\hat{\theta})} \left[\frac{\sigma^2(\hat{b}_d)}{1 - v_1^2 \hat{b}_d^2} + \frac{\sigma^2(\hat{b}_u)}{1 - v_1^2 \hat{b}_u^2} \right] \quad (A-28)$$

$$\sigma^2(\hat{\delta}) = \frac{v_1^2 \sigma^2(\hat{b}_d)}{4(1 - v_1^2 \hat{b}_d^2)} + \frac{v_1^2 \sigma^2(\hat{b}_u)}{4(1 - v_1^2 \hat{b}_u^2)} \quad (A-29)$$



$$\sigma^2(\hat{h}_{ou}) = \left\{ \frac{v_1^2}{4N_u \cos^2(\delta) \cos^2(\hat{\theta})} \right\} \left\{ \hat{b}_u \cdot \sigma^2(X_u) + \sigma^2(Y_u) \right\} \quad (A-30)$$

$$+ \left\{ \left[\frac{v_1 t_{ou}}{2(\hat{b}_d + \hat{b}_u) \sqrt{1 - v_1^2(\hat{b}_d)^2}} \right] \left[\tan(\hat{s}) \tan(\hat{\theta}) + \tan^2(\hat{\theta}) \right] \right\}^2 \left\{ \sigma^2(\hat{b}_d) \right\}$$

$$+ \left\{ \left[\frac{\tan(\hat{\theta})}{\hat{b}_d + \hat{b}_u} \right] \left[\bar{X}_u + \left(\frac{v_1 t_{ou}}{2\sqrt{1 - v_1^2(\hat{b}_u)^2}} \right) \left(\tan(\hat{\delta}) - \tan(\hat{\theta}) \right) \right] \right\}^2 \sigma^2(\hat{b}_u)$$

The expression for $\sigma^2(\hat{h}_{od})$ is identical to Equation A-30 with the subscript u replaced by d and d replaced by u wherever they appear.

The previous expressions, obtained using Equation A-17, are of unknown value due to the nonlinear nature of Equations A-19 through A-23. At this point, sample variance will be considered as a method of estimating the true population variance.

It can be shown that the sample variance is an optimum estimate in the sense of maximum likelihood of the true variance when the distribution is normal,¹⁸ and it is suspected that the estimates so obtained will be good estimates provided the true density is symmetrical about its peak and is approximately normal. The maximum-likelihood estimator just discussed is efficient and consistent, and it possesses a property called invariance. For these reasons, the estimate for the variance of each quantity determined by Equations A-19, A-21, A-22, and A-23 will be the corresponding sample variance. Denotating the elements $\{\hat{V}, \hat{\delta}, \hat{h}_{ou}, \hat{h}_{od}\}$ by $\{M\}$, the unbiased (normal case) estimate of the variance is

$$\hat{\sigma}^2 = \frac{1}{N-1} \sum_{i=1}^N (M_i - \bar{M})^2 \quad (A-31)$$



where \bar{M} , the sample mean, is given by

$$\bar{M} = \frac{1}{N} \sum_{i=1}^N M_i \quad (A-32)$$

However, for the volume of data available, it is necessary to use Equations A-28, A-29, and A-30, as $N = 1$ in Equations A-31 and A-32.

Confidence limits can now be determined using some $\underline{\sigma}^2$ as the variance of a normal distribution of zero mean and confidence level N such as

$$A = M + P(N) \underline{\sigma} \quad (A-33a)$$

and

$$B = M - P(N) \underline{\sigma} \quad (A-33b)$$

A and B denote the upper and lower N-percent confidence limits on the computed quantity M obtained from Equations A-19, A-21, A-22, and A-23. $P(N)$ is the standard-deviation multiplier obtained for N-percent confidence of a normal random variable of zero mean and unit variance (found in standard tables); $\underline{\sigma}$ is obtained from $\underline{\sigma}^2$. The computed parameters and their confidence limits, computed at both the 95-percent [$P(0.95) = 1.96$] and the 90-percent [$P(0.90) = 1.64$] confidence limits, are shown in Tables A-1 and A-2.

Since the a priori value of K^2 (Equation A-16) indicated that distance errors are relatively more significant than time errors, a one-variable-in-error line fit for each set of data points was also considered. For X-in-error line fit, the slope \hat{b}_x is given by Equations A-8 and A-9 (when $K^2 = 0$) as

$$\hat{b}_x = \frac{\sum_{i=1}^N (t_i - \bar{t})^2}{\sum_{i=1}^N (X_i - \bar{X})(t_i - \bar{t})} \quad (A-34)$$



The variance of the slope estimate is

$$\sigma^2 (\hat{b}_x) = \frac{\hat{b}_x^4 \sigma_x^2}{\sum_{i=1}^N (t_i - \bar{t})^2} \quad (A-35)$$

where

$$\hat{\sigma}_x^2 = \frac{\sum_{i=1}^N (X_i - \bar{X})^2 - \hat{b}_x^{-1} \sum_{i=1}^N (X_i - \bar{X})(t_i - \bar{t})}{N - 2} \quad (A-36)$$

The average value of σ_x^2 estimated using Equation 2-36 was approximately 16 km^2 , indicating that the original a priori value of σ_x^2 (10.4 km^2) was of the correct order of magnitude and was approximately correct.

Essentially the same values occur for model parameters and the model parameters' confidence limits when it is assumed that both time and distance are subject to error as when it is assumed that only time is subject to error (Table A-1). It may be concluded, therefore, that no significant increase in accuracy of the parameter calculations is gained by using the more complicated two-variables-in-error line fits rather than standard least-square-error line fits. It also may be concluded that distance-error effects are negligible compared to timing-error effects.



Table A-1
PARAMETERS AND CONFIDENCE LIMITS, SOUTHERN REVERSE PROFILE

Parameter	Value	Calculations Made Assuming Both Variables in Error		Calculations Made Assuming Time Only in Error	
		Upper Confidence Limit A; Lower Confidence Limit B	95-Percent Level	90-Percent Level	Upper Confidence Limit A; Lower Confidence Limit B
Dip Angle δ (°)	4.17	A = 9.17 B = -0.83	A = 8.36 B = -0.02	4.17	A = 9.17 B = -0.83
Refractor Velocity V_2 (km/sec)	8.03	A = 8.47 B = 7.59	A = 8.40 B = 7.66	8.03	A = 8.63 B = 7.43
Depth to Refractor	33.2	A = 42.0 B = 24.4	A = 40.6 B = 25.8	33.1	A = 42.0 B = 24.2
Depth to Refractor, Shallow End h_{od} (km)	16.3	A = 22.2 B = 10.4	A = 21.3 B = 11.3	16.3	A = 23.1 B = 9.5



Table A-2

PARAMETERS AND CONFIDENCE LIMITS, NORTHERN REVERSE PROFILE

Parameter	Value	Calculations Made Assuming Both Variables in Error		Calculations Made Assuming Time Only in Error	
		Upper Confidence Limit A; Lower Confidence Limit B		Upper Confidence Limit A; Lower Confidence Limit B	
		95-Percent Level	90-Percent Level	95-Percent Level	90-Percent Level
Dip Angle δ (°)	11. 2	A = 16. 1 B = 6. 3	A = 15. 3 B = 7. 1	11. 2	A = 16. 1 B = 6. 3
Refractor Velocity V_2 (km/sec)	8. 10	A = 8. 55 B = 7. 65	A = 8. 48 B = 7. 72	8. 09	A = 8. 54 B = 7. 64
Depth to Refractor, Deep End h_{ou} (km)	57. 4	A = 68. 5 B = 46. 3	A = 66. 6 B = 48. 2	57. 4	A = 68. 9 B = 45. 9
Depth to Refractor, Shallow End h_{od} (km)	20. 7	A = 25. 9 B = 15. 5	A = 25. 1 B = 16. 3	20. 7	A = 25. 9 B = 15. 5

UNCLASSIFIED
Security Classification

DOCUMENT CONTROL DATA - R&D

(Security classification of title, body of abstract and indexing annotation must be entered when the overall report is classified)

1. ORIGINATING ACTIVITY (Corporate author) Texas Instruments Incorporated Science Services Division P. O. Box 5621, Dallas, Texas 75222		2a. REPORT SECURITY CLASSIFICATION Unclassified 2b. GROUP
3. REPORT TITLE FINAL ANALYSIS REPORT ALEUTIAN ISLANDS EXPERIMENT – OCEAN-BOTTOM SEISMOGRAPHIC EXPERIMENTS		
4. DESCRIPTIVE NOTES (Type of report and inclusive dates) Final Report 31 July 1968		
5. AUTHOR(S) (Last name, first name, initial) Linville, A. Frank Howard, R. Fred Mendina, A. Ronald Bauer, Ronald D. McNeely, Gary D.		
6. REPORT DATE 31 July 1968	7a. TOTAL NO. OF PAGES 116	7b. NO. OF REFS 18
8a. CONTRACT OR GRANT NO. Contract F33657-67-C-1341 b. PROJECT NO. AFTAC Project No. VELA T/7704 c. d.	8b. ORIGINATOR'S REPORT NUMBER(S) _____	
8d. OTHER REPORT NO(S) (Any other numbers that may be assigned this report) _____		
10. AVAILABILITY/LIMITATION NOTICES Distribution of this document is unlimited.		
11. SUPPLEMENTARY NOTES ARPA Order No. 624 ARPA Program Code No. 7F10	12. SPONSORING MILITARY ACTIVITY Advanced Research Projects Agency Department of Defense The Pentagon, Washington, D.C. 20301	
13. ABSTRACT The crustal structure across Amchitka was determined from two in-line reversed-refraction profiles located northeast and southwest of Amchitka. Both profiles employed 10 Ocean-Bottom Seismographs (OBS) spaced at 20-km intervals and 5-ton shots detonated at 20-km intervals off each end of the OBS line. Travel-times were corrected to a reference plane 4.5 km below sea level to minimize lateral velocity variations associated with the large changes in water depth in the area. Depth to the Moho along the profile was determined from first arrivals using standard refraction analysis, wavefront methods, the time-term method and model perturbation techniques. Calculations show the Moho refractor to be dipping towards Amchitka with the root of the structure located 60 km north of Amchitka under Semisopochnoi Island. The Moho velocity is 8.1 km/sec in the area. Nearly all of the first arrivals were Moho refractions; therefore, digital techniques were employed to enhance the capability of picking secondary arrivals in order to obtain upper crustal velocity information. In general, secondary arrivals were difficult to identify, and although some apparent velocity measurements were obtained, the information could not be directly incorporated into the crustal model.		

UNCLASSIFIED

Security Classification

14. KEY WORDS	LINK A		LINK B		LINK C	
	ROLE	WT	ROLE	WT	ROLE	WT
Ocean-Bottom Seismographs						
Aleutian Islands Experiment						
Amchitka Crustal Structure						
Standard Refraction Analysis						
Wavefront Methods						
Time-Term Method						
Model Perturbation Techniques						

INSTRUCTIONS

1. ORIGINATING ACTIVITY: Enter the name and address of the contractor, subcontractor, grantee, Department of Defense activity or other organization (corporate author) issuing the report.

2a. REPORT SECURITY CLASSIFICATION: Enter the overall security classification of the report. Indicate whether "Restricted Data" is included. Marking is to be in accordance with appropriate security regulations.

2b. GROUP: Automatic downgrading is specified in DoD Directive 5200.10 and Armed Forces Industrial Manual. Enter the group number. Also, when applicable, show that optional markings have been used for Group 3 and Group 4 as authorized.

3. REPORT TITLE: Enter the complete report title in all capital letters. Titles in all cases should be unclassified. If a meaningful title cannot be selected without classification, show title classification in all capitals in parenthesis immediately following the title.

4. DESCRIPTIVE NOTES: If appropriate, enter the type of report, e.g., interim, progress, summary, annual, or final. Give the inclusive dates when a specific reporting period is covered.

5. AUTHOR(S): Enter the name(s) of author(s) as shown on or in the report. Enter last name, first name, middle initial. If military, show rank and branch of service. The name of the principal author is an absolute minimum requirement.

6. REPORT DATE: Enter the date of the report as day, month, year; or month, year. If more than one date appears on the report, use date of publication.

7a. TOTAL NUMBER OF PAGES: The total page count should follow normal pagination procedures, i.e., enter the number of pages containing information.

7b. NUMBER OF REFERENCES: Enter the total number of references cited in the report.

8a. CONTRACT OR GRANT NUMBER: If appropriate, enter the applicable number of the contract or grant under which the report was written.

8b, 8c, & 8d. PROJECT NUMBER: Enter the appropriate military department identification, such as project number, subproject number, system numbers, task number, etc.

9a. ORIGINATOR'S REPORT NUMBER(S): Enter the official report number by which the document will be identified and controlled by the originating activity. This number must be unique to this report.

9b. OTHER REPORT NUMBER(S): If the report has been assigned any other report numbers (either by the originator or by the sponsor), also enter this number(s).

10. AVAILABILITY/LIMITATION NOTICES: Enter any limitations on further dissemination of the report, other than those imposed by security classification, using standard statements such as:

- (1) "Qualified requesters may obtain copies of this report from DDC."
- (2) "Foreign announcement and dissemination of this report by DDC is not authorized."
- (3) "U. S. Government agencies may obtain copies of this report directly from DDC. Other qualified DDC users shall request through _____."
- (4) "U. S. military agencies may obtain copies of this report directly from DDC. Other qualified users shall request through _____."
- (5) "All distribution of this report is controlled. Qualified DDC users shall request through _____."

If the report has been furnished to the Office of Technical Services, Department of Commerce, for sale to the public, indicate this fact and enter the price, if known.

11. SUPPLEMENTARY NOTES: Use for additional explanatory notes.

12. SPONSORING MILITARY ACTIVITY: Enter the name of the departmental project office or laboratory sponsoring (paying for) the research and development. Include address.

13. ABSTRACT: Enter an abstract giving a brief and factual summary of the document indicative of the report, even though it may also appear elsewhere in the body of the technical report. If additional space is required, a continuation sheet shall be attached.

It is highly desirable that the abstract of classified reports be unclassified. Each paragraph of the abstract shall end with an indication of the military security classification of the information in the paragraph, represented as (TS), (S), (C), or (U).

There is no limitation on the length of the abstract. However, the suggested length is from 150 to 225 words.

14. KEY WORDS: Key words are technically meaningful terms or short phrases that characterize a report and may be used as index entries for cataloging the report. Key words must be selected so that no security classification is required. Identifiers, such as equipment model designation, trade name, military project code name, geographic location, may be used as key words but will be followed by an indication of technical context. The assignment of links, rules, and weights is optional.